"Ships at a distance have every man's wish on board. For some they come in with the tide. For others they sail forever on the horizon, never out of sight, never landing until the Watcher turns his eyes away in resignation, his dreams mocked to death by Time. That is the life of men."

Zora Neale Hurston
Their Eyes Were Watching God

University of Alberta

Lifetime measurement of trapped staus using ATLAS

by

Logan Alfred Boyd Sibley

A thesis submitted to the Faculty of Graduate Studies and Research in partial fulfillment of the requirements for the degree of **Master of Science**.

Department of Physics

Edmonton, Alberta
Spring 2008

Library and Archives Canada

Published Heritage Branch

395 Wellington Street
Ottawa ON K1A 0N4
Canada

Bibliothèque et Archives Canada

Direction du Patrimoine de l'édition

395, rue Wellington
Ottawa ON K1A 0N4
Canada

Your file Votre référence
ISBN: 978-0-494-45886-0
Our file Notre référence
ISBN: 978-0-494-45886-0

NOTICE:
The author has granted a non-exclusive license allowing Library and Archives Canada to reproduce, publish, archive, preserve, conserve, communicate to the public by telecommunication or on the Internet, loan, distribute and sell theses worldwide, for commercial or non-commercial purposes, in microform, paper, electronic and/or any other formats.

The author retains copyright ownership and moral rights in this thesis. Neither the thesis nor substantial extracts from it may be printed or otherwise reproduced without the author's permission.

AVIS:
L'auteur a accordé une licence non exclusive permettant à la Bibliothèque et Archives Canada de reproduire, publier, archiver, sauvegarder, conserver, transmettre au public par télécommunication ou par l'Internet, prêter, distribuer et vendre des thèses partout dans le monde, à des fins commerciales ou autres, sur support microforme, papier, électronique et/ou autres formats.

L'auteur conserve la propriété du droit d'auteur et des droits moraux qui protège cette thèse. Ni la thèse ni des extraits substantiels de celle-ci ne doivent être imprimés ou autrement reproduits sans son autorisation.

In compliance with the Canadian Privacy Act some supporting forms may have been removed from this thesis.

While these forms may be included in the document page count, their removal does not represent any loss of content from the thesis.

Conformément à la loi canadienne sur la protection de la vie privée, quelques formulaires secondaires ont été enlevés de cette thèse.

Bien que ces formulaires aient inclus dans la pagination, il n'y aura aucun contenu manquant.

Canada

Abstract

I study the creation of long-lived staus at a 14 TeV centre of mass energy in proton-proton collisions at the LHC using both the ATLAS and ACME detectors. The ATLAS overburden or underburden, or even ATLAS itself, may trap the semi-stable staus at that place where they will remain until the time at which they decay, where the stau lifetime ranges between seven days and one year. Using a novel method, one may count the number of muons and pions originating from the stau decay using the standard ATLAS cosmic ray trigger. Using an idealized detector model, I find that this method can lead to measurements of the stau lifetime and SUSY cross-section to within statistical uncertainties of 6% and 1% of their actual values, respectively.

Acknowledgements

I must first and foremost acknowledge the work of Jonathan Braden who initially developed the analysis that I extend in this thesis. With neither his help nor the volume of discourse we exchanged, I believe that this project may have never fully come to fruition. With that, I also acknowledge my supervisor, Dr. James Pinfold, for conceiving this project. Jim has, and I am sure that others will agree, an uncanny ability to envisage the most creative and interesting physics projects for his students.

Next, I would like to thank the other students in the Alberta ATLAS group – Sang Hee, Daniel, Kevin, Stephen, Hossain and Yushu – and my friends Cara and Matthew for aiding my quest and for engaging me in many thought-provoking discussions. In addition to them, I would like to thank Richard Soluk for shaping my abilities as a researcher, starting even before my work on ATLAS began, as well as for allowing me to use his model of the ATLAS overburden.

I would also like to thank my room-mate Logan for surviving me for the past five (almost) years.

Finally, I would like to thank my parents Elmer and Judy, sister Korin and brother Morgan for the unwavering support they have given me in all the exploits I undertook over the course of my time here at the University of Alberta.

Apart from this list, for she is in a category all her own, I thank my girlfriend Amy, whose ability to patiently listen to the ramblings of a would-be physicist are second to none.

Contents

1 Theory and motivation **4**
- 1.1 The Standard Model . . . 4
  - 1.1.1 Standard model shortcomings and their solutions . . . 8
- 1.2 Supersymmetry . . . 10
  - 1.2.1 Supersymmetry as an extension of the standard model 11
  - 1.2.2 Supersymmetry breaking . . . 12
  - 1.2.3 Stable massive particles . . . 13
- 1.3 Motivation . . . 15
- 1.4 Upward-going muons . . . 16

2 ATLAS and the LHC **19**
- 2.1 The Large Hadron Collider . . . 19
  - 2.1.1 Operating schedule . . . 21
- 2.2 ATLAS . . . 21
  - 2.2.1 The inner detector . . . 22
  - 2.2.2 The calorimetry . . . 25
  - 2.2.3 The muon system . . . 30
  - 2.2.4 The magnet system . . . 36

3 The ATLAS trigger system **39**
- 3.1 The low-level trigger . . . 40
- 3.2 Regions of interest . . . 47
- 3.3 The high-level trigger . . . 47
  - 3.3.1 Event selection . . . 48
- 3.4 The cosmic ray trigger . . . 50

4 Modelling ATLAS and its surroundings **53**
- 4.1 The inner detector . . . 55
  - 4.1.1 The pixel detector . . . 55
  - 4.1.2 The semiconductor tracker . . . 57
  - 4.1.3 The transition radiation tracker . . . 59
- 4.2 The calorimetry . . . 63
  - 4.2.1 The electromagnetic calorimeter . . . 63
  - 4.2.2 The hadronic tile calorimeter . . . 65
  - 4.2.3 The liquid argon endcap calorimeter . . . 67

4.2.4 The forward calorimeter 69
4.3 The muon system 70
4.3.1 The monitored drift tube chambers 70
4.3.2 The cathode strip chambers 73
4.3.3 The resistive plate chambers 74
4.3.4 The thin gap chambers 76
4.4 The magnet system 78
4.4.1 The barrel solenoid 80
4.4.2 The barrel and endcap toroids 81
4.5 The beam pipe and forward shielding 83
4.6 The ATLAS overburden and underburden and cavern system . 84

5 Analysis I **89**
5.1 Monte Carlo data production 90
5.2 Stau trapping 91
5.3 Stau decay detection 96
5.3.1 Trigger decision 105
5.3.2 Detector acceptance 107
5.4 Background sources 112

6 Analysis II **115**
6.1 Stau production and decay rates 116
6.2 The stau lifetime and SUSY cross-section fit 119

7 Conclusion **133**

Bibliography **135**

A ACME, an extension of ATLAS' reach **140**

B The ACME solid angle **142**

C Analytic number of remaining staus **152**

List of Tables

1.1 The SM forces and their mediators 5
1.2 Weak isospins and hypercharges of the leptons and quarks. . . 6

3.1 Muon trigger thresholds 45

4.1 Layout of the pixel detector 56
4.2 Material composition of the pixel detector 57
4.3 Radiation length contributions of the pixel detector 57
4.4 Layout of the SCT 58
4.5 The SCT ring structure and composition 59
4.6 Material composition of the SCT 60
4.7 Radiation length contributions of the SCT 60
4.8 Layout of the TRT 61
4.9 Material composition of the TRT 62
4.10 Radiation length contributions of the TRT 62
4.11 Layout of the ECAL 64
4.12 Material composition of the ECAL 64
4.13 Thickness of the ECAL materials 65
4.14 Volume contributions of the ECAL 66
4.15 Layout of the tile HCAL 67
4.16 Material composition of the tile HCAL 67
4.17 Volume contributions of the tile HCAL 67
4.18 Layout of the LAr HCAL 68
4.19 Material composition of the LAr HCAL 68
4.20 Volume contributions of the LAr HCAL 68
4.21 Layout of the FCAL 69
4.22 Material composition of the FCAL 70
4.23 Volume contributions of the FCAL 70
4.24 Layout of the MDTs 72
4.25 Material composition of the MDTs 72
4.26 Volume contributions of the MDTs 72
4.27 Layout of the CSCs 73
4.28 Material composition of the CSCs 74
4.29 Volume contributions of the CSCs 74
4.30 Layout of the RPCs 75
4.31 Material composition of the RPCs 76

4.32 Volume contributions of the RPCs 76
4.33 Layout of the TGCs 78
4.34 Material composition of the TGCs 78
4.35 Volume contributions of the TGCs 78
4.36 Material composition of the magnet system 80
4.37 Mass contributions of the barrel solenoid 80
4.38 Mass contributions of the barrel and endcap toroids 82
4.39 Barral and endcap toroid magnetic field parameters 83
4.40 Layout and dimensions of the forward shielding 84
4.41 The ATLAS overburden and underburden layout and material characteristics 85

5.1 mSUGRA simulation parameters 91
5.2 Gravitino masses 99
5.3 ATLAS upward-going acceptance 110
5.4 ACME upward-going acceptance 110
5.5 Total upward-going acceptance 111

6.1 LHC operating schedule scenario 116
6.2 ATLAS and ACME fit results 122
6.3 Combined fit results 122
6.4 Fit resolutions for a 30 day lifetime 124
6.5 ATLAS fit resolutions 131
6.6 ATLAS fit resolution errors 132

List of Figures

1.1 Electroweak symmetry breaking potential 7
1.2 Higgs loop corrections 9
1.3 Unification of the SM coupling constants 10
1.4 SUSY mass spectrum 14

2.1 The LHC injector chain 20
2.2 LHC dipole magnets 21
2.3 The ATLAS detector 23
2.4 The ATLAS inner detector 24
2.5 The ATLAS calorimetry 26
2.6 Accordion geometry of the ECAL 28
2.7 Module of the tile HCAL 29
2.8 Liquid argon gaps in the FCAL 31
2.9 The muon spectrometer 32
2.10 A MDT chamber 33
2.11 Layout of the CSCs 34
2.12 Layout of the RPCs 35
2.13 View of the doublet and triplet TGCs 36
2.14 The magnet system 37
2.15 The ATLAS magnetic field 38
2.16 Map of the ATLAS magnetic field integral 38

3.1 The LVL1 trigger 40
3.2 LVL1 calorimeter trigger towers 42
3.3 LVL1 calorimeter jet trigger windows 43
3.4 LVL1 RPC trigger scheme 44
3.5 LVL1 TGC trigger scheme 46
3.6 Introduction of dummy hits in the TGCs 52

4.1 The pixel detector 56
4.2 The SCT 58
4.3 The TRT 61
4.4 The ECAL 64
4.5 The tile HCAL 66
4.6 The LAr HCAL 68
4.7 The FCAL 69

4.8 The MDT chambers 71
4.9 The CSCs 73
4.10 The RPCs 75
4.11 The TGCs 77
4.12 The magnet system 79
4.13 The model magnetic field map 82
4.14 The beam pipe and forward shielding 83
4.15 The ATLAS cavern system 85
4.16 Top and side views of the ATLAS cavern system 87

5.1 Stau energy and $\cos\theta$ distributions 92
5.2 Stau energy versus $\cos\theta$ 93
5.3 Stau stopping positions 94
5.4 Stau range in matter 97
5.5 Stau lifetime distribution 98
5.6 ACME particle types 99
5.7 ACME hit positions 100
5.8 ACME hit momenta 100
5.9 ATLAS particle types 101
5.10 ATLAS hit positions 102
5.11 ATLAS hit momenta 103
5.12 ATLAS hit momenta of all particles 104
5.13 ATLAS and ACME detector acceptances 108
5.14 Total acceptance 109
5.15 Super-K upward-going muon flux 112

6.1 Number of stau decays at ATLAS 118
6.2 Total number of stau decays at ATLAS over six years 119
6.3 ATLAS and ACME lifetime fits 121
6.4 Combined lifetime fit 123
6.5 ATLAS and ACME lifetime fit distributions 125
6.6 ATLAS and ACME cross-section fit distributions 126
6.7 ATLAS and ACME background rate fit distributions 127
6.8 Combined data lifetime fit distribution 128
6.9 Combined data cross-section fit distribution 128
6.10 Combined data background rate fit distributions 129

A.1 The ACME detector 140
A.2 ACME in the ATLAS cavern 141

B.1 Solid angle of a square 143
B.2 Solid angle of a rectangle 145
B.3 Zenith angle dependence 1 146
B.4 Zenith angle dependence 2 147
B.5 Solid angle of a trapezoid 148

Introduction

> Iapetus led away the girl Clymene, an Oceanid, and they went together in the same bed; and she bore to him a child, stout-hearted Atlas; she also brought forth Menoetius, of very great renown, and devious and clever Prometheus, and Epimetheus, who was faulty in judgment and from the beginning was an evil for mortals who work for their bread. For he was the first to accept from Zeus the virgin woman he had formed. Far-seeing Zeus struck arrogant Menoetius with his smoldering bolts and hurled him down into Erebus because of his presumption and excessive pride. Atlas stands and holds the wide heaven with his head and tireless hands through the force of necessity at the edge of the earth, and in the sight of the clear-voiced Hesperides; this fate Zeus in his wisdom allotted him.
>
> Hesiod, *Theogony*

ATLAS (A Toroidal Large Hadron Collider ApparatuS) is a device of discovery, poised to sit at the forefront of high energy physics as the Large Hadron Collider (LHC), soon to be the highest energy particle accelerator on earth, prepares for its initial beam running in mid-2008. Its goal is the discovery of the Higgs boson, the last, as of yet undiscovered, particle of the Standard Model. Nevertheless, it is able to accomplish much more than just that. ATLAS has the capacity to explore the unknown regions of fundamental physics by searching for evidence of new particles and the ways in which they interact that one can currently only conceptualize in theory. As such, it becomes an invaluable instrument for our understanding of the universe on both the smallest and the largest of scales. Just as the Titan Atlas supports the heavens

with his "tireless hands" [1, 2], so too will ATLAS support the interrogation of nature at its most fundamental of levels.

Of all of its additional uses, perhaps one of the most intriguing is the ability of ATLAS to detect evidence of supersymmetry [3, 4], which is one postulated extension of the Standard Model that aids in overcoming some of the maladies from which it suffers. One of the major consequences of introducing supersymmetry into the Standard Model is that it introduces for every Standard Model particle a supersymmetric particle, or sparticle, partner. If supersymmetry were a perfect symmetry, then, one would expect that each sparticle would have the same mass as its Standard Model particle partner. Unfortunately, since no experiment has ever detected a sparticle, this cannot be the case. Therefore, supersymmetry must be a broken symmetry, inflating the masses of the sparticles to a level that is, presumably, just beyond the reach of creation by current colliders. It is the high centre-of-mass operating energy of the LHC that will hopefully allow us to see evidence of these sparticles. Chapter 1 delves more deeply into the theory of the Standard Model and the phenomenology of supersymmetry.

There are several theoretical models available, such as supergravity and gauge-mediated supersymmetry breaking, that describe how supersymmetry can break. In the supergravity model, there exist cosmologically-favoured regions in its parameter space where the dominant phenomenology is that of the gravitino as the lightest sparticle and the stau as the next-to-lightest sparticle. Within these regions it is possible for the stau to obtain an extended lifetime, ranging upwards to the order of one year [5]. Assuming that these parameters describe the physical world, it could be possible that these staus will travel away from their production point within ATLAS and become trapped in the rock overburden or underburden of the ATLAS cavern, or even in the ATLAS detector itself, where they will sit and await their eventual decay. Chapter 2 provides details about the ATLAS detector, chapter 4 discusses the simulation model of ATLAS that this thesis will use and chapter 5 describes the simulation of the stau trapping.

The stau, in order to conserve R-parity, will decay directly into a tau,

its Standard Model counterpart, and a gravitino, where the tau subsequently decays via Standard Model interactions, leading mainly to the production of pions and muons. Many of these pions and muons, resembling muons that originate from cosmic rays, could, in fact, pass through the dedicated muon systems of the ATLAS detector, where one could use the ATLAS trigger, which chapter 3 discusses, to measure the stau decay rate. Also, using the idea of having a unique secondary scintillator detector ACME (ATLAS Cosmic Muon and Exotics detector) [6] on the roof of the ATLAS cavern, as appendix A discusses, could aid this measurement. Then, using the stau decay rate, one can determine both the lifetime of the sleptons and the supersymmetry production cross-section, where the method one can use to do this and the results of doing so comprise chapter 6. What is more, if the two detectors remain operational during those scheduled periods when the LHC beam is off, one will obtain a clean signal with a very limited source of background, resulting almost exclusively from cosmic rays. As such, this thesis will only consider times when the beam is off.

There is some attention in the literature given to the problem of the detection of stable massive particles and slepton trapping. The work of [7] and [8] describes using the standard ATLAS muon systems to measure the mass of slow-moving stable massive particles. Hamaguchi et al. discuss using a detector consisting of a tracker and heavy stopping material that can measure the arrival times and positions of long-lived staus that stop within it [9,10]. Using such a setup, one could then study the stau decay products in detail. Lastly, Jonathan Feng, whose theoretical ideas form a basis for the work this thesis considers, proposes using water tanks to trap long-lived staus, which one could subsequently drain to a low-radiation environment to study the stau decay in detail [5]. Where this thesis is unique is in its ability to determine the stau lifetime using only the ATLAS detector, where one does not require any special upgrades or traps for the analysis to proceed. As such, one could use the methods I develop in this thesis as the basis for an initial study searching for the trapped stau signal. I regard this thesis to be complementary to other studies, where chapter 7 reports on the conclusions of this work.

Chapter 1

Theory and motivation

This chapter describes the theory and motivation upon which I structure this thesis. It begins with a description of the Standard Model of particle physics and the maladies from which it suffers. It then moves on to a description of one possible extension of the Standard Model, supersymmetry, and the phenomenology of a gravity-mediated supersymmetry model, where the gravitino is the lightest supersymmetric particle. The next section of the theory suggests what motivation there is for undertaking this thesis. The final section concerns itself with upward-going muons, which are an important background to this study.

1.1 The Standard Model

The Standard Model (SM) of particle physics is a mathematical description of matter and its interactions and consists of two groups of particles that have an internal spin quantum number, S. The spin-1/2 fermions, forming the visible matter in the universe, make up the first particle group, where one can further decompose the fermions into two subgroups: the leptons and quarks. In all, there are three fermion generations, where, in order of increasing mass, the leptons are the electron, the muon and the tau lepton, with each generation containing a corresponding neutrino. The quark generations, in order of increasing mass, progress as the down and up quarks, the strange and charm quarks and, finally, the bottom and top quarks.

The distinction between these subgroups lies in the fact that quarks can in-

Force	Strength	Mediator
Strong	10	Gluons (8)
Electromagnetic	10^{-2}	Photon
Weak	10^{-13}	$W^{\pm}$ and Z^0
Gravity	10^{-42}	Graviton

Table 1.1: The SM includes a description of the electromagnetic, weak, and strong forces, where the bosons act as the force carriers. The SM does not contain a description of gravity, although the table lists its strength for comparison.

teract via the strong force, whereas leptons cannot. As its name may suggest, the strong force is the most potent of the forces in the SM, providing the force necessary to bind together quarks into baryons, a three-quark bound state, and mesons, a two-quark bound state. One consequence of the strong force is quark confinement, which does not allow quarks to exist in an unbound state. A process known as hadronization prevents the existence of these free quarks, whereby a quark in danger of breaking free from the grip of its quark partner will spontaneously transform into a quark-anti-quark pair, which, upon iteration of this process, can lead to the production of a jet of hadronic material. The top quark is an exception to this rule, where its lifetime is so short that it will decay before the hadronization process can occur. Those particles that can interact via the strong force also possess colour charge, which is to the strong force what the electric charge is to the electromagnetic force. The difference is that there exist three colour charges to choose from - red, green and blue - along with their corresponding anti-colours.

The other two forces that comprise the SM are the electromagnetic force and the weak force, where only charged particles can interact electromagnetically, but all particles, with the exception of photons and gluons, can interact weakly. Of the three forces, the weak force, again, as its name should suggest, is the weakest, with a strength that is a full 13 orders of magnitude feebler than the strong force. Table 1.1 shows the relative strength of the forces in the SM, as well as the bosonic mediators of each [11].

The second group of particles consists of the bosons. These particles mediate the interactions between the fermions and themselves, where the eight gluons mediate the strong force, the photon mediates the electromagnetic force

I	II	III	I_L	I_R	I_L^3	I_R^3	Y_L	Y_R	Q
e	μ	τ	1/2	0	-1/2	0	-1	-2	-1
ν_e	ν_μ	ν_τ	1/2	0	1/2	0	-1	0	0
u	c	t	1/2	0	1/2	0	1/3	4/3	2/3
d'	s'	b'	1/2	0	-1/2	0	1/3	-2/3	-1/3

Table 1.2: The table lists the weak isospins and hypercharges of the leptons and quarks, where I^3 refers to the third component of the weak isospin I, Y is the weak hypercharge and Q is the electric charge [13]. I, II and II correspond to the three fermion generations.

and the $W^\pm$ and Z^0 bosons mediate the weak force [1].

One can actually describe the forces themselves in terms of the operations of a particular Lie group [12]. The strong force, mediating quantum chromodynamics (QCD), involves representations of the Lie group $SU(3)_c$. Since this group is non-abelian, it leads to the self-interaction of the gluons, where the gluons will also have a colour charge. One can describe the unbroken electromagnetic force with $U(1)_Y$ and weak force with $SU(2)_L$, which a weak hypercharge and isospin characterize, respectively. The U(1) group is abelian, which results in the photon being unable to interact with itself. Of course, since the SU(2) group is non-abelian, like the QCD representation, the carriers of the weak force can also interact with themselves. Upon taking the product $U(1)_Y \times SU(2)_L$, one arrives at a representation of electroweak theory, which combines the electromagnetic and weak theories into one entity. Table 1.2 lists the weak isospin and hypercharge for the leptons and quarks. The Gell-Mann-Nishijima relation gives the electric charge in terms of the weak isospin and hypercharge [13] as

$$Q = I^3 + \frac{1}{2}Y. \tag{1.1}$$

Since we know from experiment that most particles, including neutrinos, are massive, there must exist some mechanism in the SM that generates this mass. Inserting gauge boson mass terms into the SM Lagrangian destroys its invariance under gauge transformations [14], which is undesirable. In order to preserve this invariance, one invokes the Higgs mechanism [13], which in-

[1]There is also the graviton that would mediate the gravitational force, but, one does not include gravity in the SM.

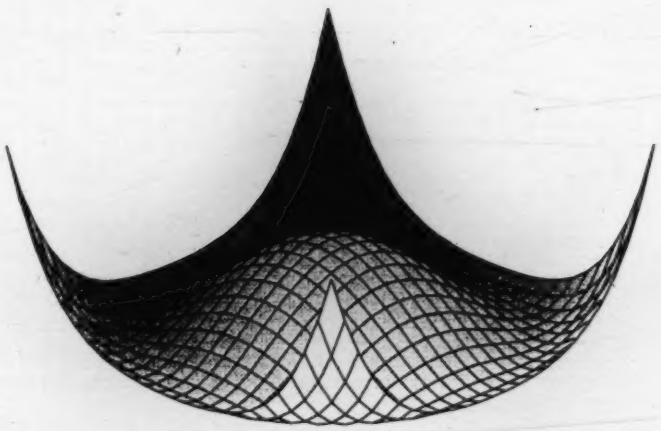

Figure 1.1: This potential allows symmetry breaking to occur, since the minimum is not unique. The figure shows a three-dimensional representation of ϕ_1 versus ϕ_2.

troduces a pair of scalar fields (ϕ_1,ϕ_2) with a potential $V(\phi_1^2 + \phi_2^2)$ that has a degenerate minimum. Figure 1.1 shows an example of such a potential, where ϕ_1 and ϕ_2 are the real and imaginary components, respectively, of a complex scalar field ϕ.

Since the minimum of this potential, lying away from zero, is not unique, its addition into the Lagrangian leads to the breaking of the electroweak gauge symmetry, and, in the process of this breaking, leads to the $W^{\pm}$ and Z^0 obtaining a mass. A scalar excitation in ϕ_2 represents the Higgs boson, which is the only particle in the SM that has yet to be seen experimentally. The fermions then obtain masses via Yukawa couplings to the Higgs field, ϕ [13].

Since the mass eigenstates and the weak eigenstates of the quarks are not equivalent, weak interactions can cause transitions between quark generations [12]. The Cabibbo-Kobayashi-Maskawa (CKM) matrix governs these transitions [13], where

$$\begin{pmatrix} d' \\ s' \\ b' \end{pmatrix} = \begin{pmatrix} V_{ud} & V_{us} & V_{ub} \\ V_{cd} & V_{cs} & V_{cb} \\ V_{td} & V_{ts} & V_{tb} \end{pmatrix} \begin{pmatrix} d \\ s \\ b \end{pmatrix}. \qquad (1.2)$$

Here, V_{ab} is the mixing component between quark types a and b. The values along the diagonal are near one and become small as one moves farther off

the diagonal. As such, this mechanism favours mixing amid a single quark generation and suppresses mixing between generations. This, in fact, leads to the extended lifetime of the bottom quark, since it must decay hadronically via a cross-generational transition. It also allows for the violation of the charge-parity (CP) symmetry in the SM, where one exchanges a particle with its anti-particle and inverts its spatial coordinates [12, 13].

As a final note, first-order corrections to the bare Higgs mass, several example Feynman diagrams for which figure 1.2 shows, diverge quadratically with the renormalization cut-off mass Λ, which one can take to be the Planck mass [15]. For a fermion of mass m_f that couples to the Higgs field with a strength G_f (the left image in figure 1.2), the corrections become

$$\delta M_{HF}^2 \propto -m_f^2 G_f \Lambda^2, \tag{1.3}$$

whereas for a boson of mass m_b and coupling G_b, the corrections become

$$\delta M_{HB}^2 \propto m_b^2 G_b \Lambda^2. \tag{1.4}$$

One should notice that the contributions from the bosonic loops differ by a negative sign from the contributions from the fermionic loops. Thus, the total correction becomes

$$\delta M_H^2 \propto \left(\sum_{bosons} c_b m_b^2 - \sum_{fermions} c_f m_f^2 \right) \Lambda^2, \tag{1.5}$$

where c_b and c_f are coefficients that depend on the boson or fermion flavour, respectively. Since Λ^2 is on the order of 10^{38}, these corrections then require the fine-tuning of the masses and couplings in order to keep the Higgs mass near the electroweak scale. Interestingly, if one were able to introduce an additional bosonic degree of freedom for every fermionic degree of freedom and vice versa, then the contributions from each would exactly cancel.

1.1.1 Standard model shortcomings and their solutions

While the performance of the SM is remarkable in terms of its ability to accurately describe nature, it also has several blemishes that cause us to believe

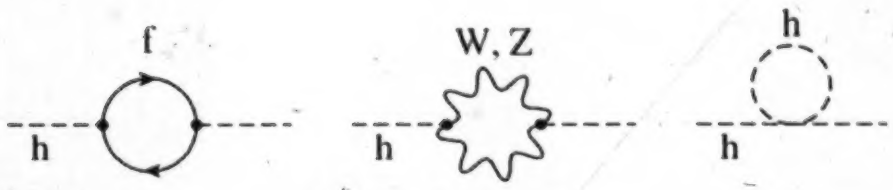

Figure 1.2: The diagrams show fermion, gauge boson and scalar boson loops, from left to right, that contribute to the effective Higgs mass [12].

that it cannot be the final theory of fundamental physics. The first of these is the fact that the SM does not include gravity. If one wishes to describe physics at the Planck scale, which is the scale of gravity, then it becomes imperative to include gravity in the theory, since at those energies concerned, the gravitational strength is on par with those of the other forces. In fact, the disparity between the strengths of the gravitational and electroweak forces at low scales - 29 orders of magnitude - is another such malignancy of the model, as there does not seem to be any natural motivation for this. Also, because of experimental evidence, it seems likely that the Higgs mass is at the electroweak scale [4], which, when one considers the loop corrections to the Higgs mass, as figure 1.2 shows, requires an extreme level of parameter fine-tuning to occur.

Additionally, while the three generation structure of the leptons and quarks is a nice property of the SM, there is no reason why this structure necessarily exists. There are also 18 free parameters in the SM – three lepton masses, six quark masses, two vector boson masses, three coupling constants and four mixing parameters in the CKM matrix – that one must measure experimentally, since they are arbitrary in the theory [16].

Although not necessary, the three forces of the SM do not unify at the Planck scale, even though the unification of the electromagnetic and weak forces at the electroweak scale would suggest that this property could, and perhaps should, occur at high energies. Finally, the SM does not provide a good candidate for dark matter, where visible baryonic matter only accounts for approximately 4% of the matter in the universe [15].

The goal of overcoming these shortcomings has led to several suggestions

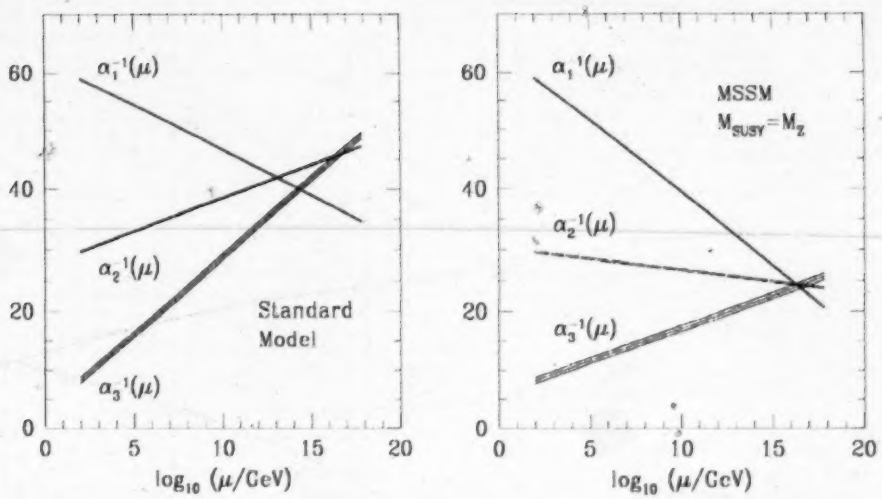

Figure 1.3: The introduction of SUSY into the SM leads to the unification of the coupling constants of the three SM forces just below the Planck scale [12].

for the more fundamental theory underlying the SM. These include, but are not limited to, the theories of extra dimensions, technicolour and supersymmetry [4]. Supersymmetry (SUSY) is a well-motivated extension of the SM that introduces an additional SUSY partner (superpartner) particle for every particle in the SM. The next section discusses SUSY and its phenomenology in more depth.

1.2 Supersymmetry

SUSY has become an important theory in terms of beyond-the-SM physics scenarios because of the multiple successes it predicts all within a framework that seems to stem from a natural motivation. It provides a natural method by which one can overcome the need to finely tune the Higgs loop corrections, unifies the couplings of the three SM forces at the Planck-scale, as figure 1.3 shows, which, according to the successes of electroweak theory, appears to be a logical requirement, and supplies a natural dark matter candidate. The following sections discuss SUSY as an extension of the standard model and the consequences of it, as such.

1.2.1 Supersymmetry as an extension of the standard model

Like gauge symmetry that requires the introduction of an anti-particle for every particle in the SM, SUSY introduces a bosonic counterpart, or superpartner, for every fermion in the SM, and vice versa. So, the operator Q that generates this transformation acts as

$$Q\,|Boson\rangle = |Fermion\rangle$$

$$Q\,|Fermion\rangle = |Boson\rangle\,. \tag{1.6}$$

Upon adding SUSY into the SM, one arrives at what is known as the minimal supersymmetric standard model (MSSM), which then contains all of the SM particles, as well as the superpartners of each. In addition to these, the MSSM also contains two hypercharge $Y = \pm 1$ Higgs doublets, where the theory requires at least two Higgs doublets in order to generate mass for both up- and down-type quarks and charged leptons [4]. Thus, the superpartners of the quark, lepton and neutrino are the spin-0 squark, slepton and sneutrino, respectively, the superpartner of the gluon is the spin-1/2 gluino, the superpartners of the charged vector bosons - $W^{\pm}$ and $H^{\pm}$ - and the neutral scalar bosons - γ, Z^0 and $H^o_{1,2}$ - become the charginos and neutralinos, respectively, which one denotes as $\tilde{\chi}^{\pm}_{1,2}$ and $\tilde{\chi}^o_{1,2,3,4}$; and the gravitino is the superpartner of the graviton [17]. As such, SUSY contains an equal number of fermionic and bosonic degrees of freedom, which allows one to solve the problem with the Higgs loop corrections, since each new bosonic degree of freedom will exactly cancel one fermionic correction in the loop calculation, removing the requirement for fine-tuning, but still allowing the Higgs mass to remain at a low scale.

The MSSM, in its most general construction, then contains 124 free parameters, because, as with the SM, theory cannot predict the masses of the superpartners and, in fact, the hierarchy of masses is not generally known. Also, since the SUSY operator Q commutes with both the squared-mass operator, $-P^2$, and the generators of gauge transformations, all superpartners

must have the same mass, electric charge, weak isospin and colour as their SM counterparts [18]. Nevertheless, if one associates SUSY with the origin of the scale of electroweak interactions (so that one overcomes the hierarchy problem, as above), then the superpartner masses should be on the order of 1 TeV, or the electroweak scale. Finally, one can include both baryon and lepton number conservation in the MSSM; consequently, the MSSM contains an invariance that one refers to as R-parity [4]. Here, one takes

$$R = (-1)^{3(B-L)+2S}, \tag{1.7}$$

where B and L refer to baryon and lepton number, respectively, and S is the particle spin. Thus, all SM particles will have an even R-parity, and all of their superpartners will have an odd R-parity. The effect of this is to prevent the decay of the lightest sparticle (LSP), since its decay would violate R-parity conservation.

1.2.2 Supersymmetry breaking

Of course, if these characteristics of the superpartners were, in fact, degenerate with their SM counterparts, then we should have already been able to experimentally verify their existence. Since no experiment has ever seen evidence of the superpartners, it follows that SUSY must be a broken symmetry, where the breaking mechanism must inflate the masses of the sparticles to a level that is above the masses of the particles in the SM. SUSY can be spontaneously broken at some high scale through the addition of general soft breaking terms that are consistent with gauge symmetry and R-parity conservation [4]. If one assumes that SUSY is a local symmetry, which requires the inclusion of gravity [19] in the theory, then this breaking leads to the gravitino acquiring a mass [4].

Because of the way in which particles in the MSSM interact, one usually considers this breaking to occur in some hidden sector, where, with respect to the SM gauge group, the particles there are neutral, which some mechanism then communicates to the visible sector of the MSSM. Minimal supergravity

(mSUGRA), which is a SUSY theory that incorporates gravity, is one such model in which gravity transmits the SUSY breaking between sectors [4].

Whereas the MSSM consists of 124 free parameters, mSUGRA condenses this number into a total of five real parameters on top of the 18 parameters (excluding the Higgs mass) from the SM. These parameters are the common scalar mass m_o, the common gaugino mass [2] $M_{1/2}$, the common soft breaking parameter A_o, the ratio of the two Higgs doublet vaccuum expectation values $\tan\beta$ and the sign of the higgsino mass term $\mathrm{sgn}\mu$. These five parameters then determine the MSSM mass spectrum, which figure 1.4 shows, as a function of the parameter $M_{1/2}$, and its interaction strengths. In mSUGRA, the gravitino acquires a mass

$$m = \frac{F}{\sqrt{3}M_*}, \tag{1.8}$$

where $\sqrt{F}$ is the SUSY breaking scale and $M_* = (8\pi\frac{G_N}{\hbar c})^{-1/2}$ is the Planck mass, with G_N being Newton's gravitational constant [20].

1.2.3 Stable massive particles

In the mSUGRA framework, one generally takes the LSP to be a slepton or a neutralino; nevertheless, it is possible to consider the gravitino to be the LSP in many sectors of the mSUGRA parameter space [20] and, if one assumes R-parity conservation, the gravitino then becomes stable. Since the gravitino couples only gravitationally, any interaction involving the gravitino becomes Planck-suppressed. As a result, because every supersymmetric particle decay chain must end with the LSP, the decay of the next-to-lightest supersymmetric particle (NLSP) into the LSP becomes Planck-supressed. It follows that the NLSP can become long-lived, where, assuming the NLSP is a stau, one can write the NLSP lifetime as

$$\tau = \frac{\hbar}{\Gamma}\ , \text{ where}$$

$$c^{-2}\Gamma(\tilde{\tau} \to \tau\tilde{G}) = \frac{1}{48\pi M_*^2}\frac{m_{\tilde{\tau}}^5}{m_{\tilde{G}}^2}\left(1 - \frac{m_{\tilde{G}}^2}{m_{\tilde{\tau}}^2}\right)^4. \tag{1.9}$$

[2] The gauginos and higgsinos, which upon mixing give us the charginos and neutralinos, are the superpartners of the gauge and Higgs bosons, respectively.

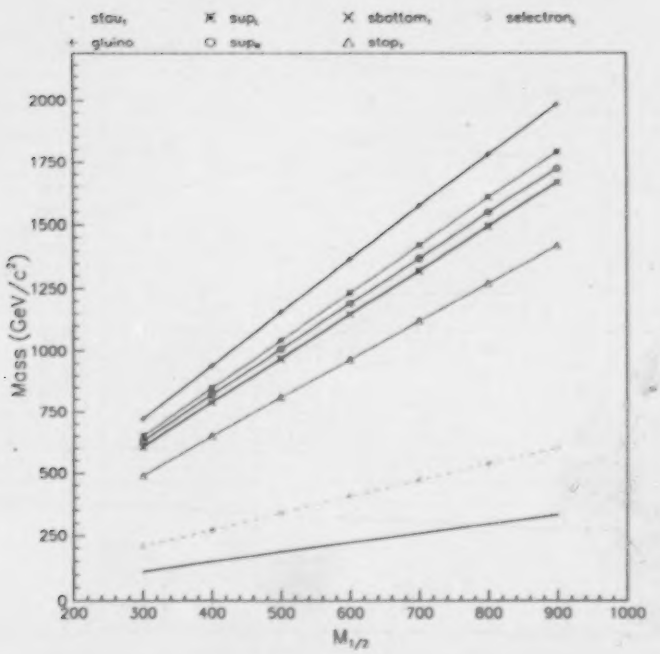

Figure 1.4: A sample of the SUSY mass spectrum in mSUGRA, as a function of $M_{1/2}$, where m_o=0, A_o=0, $\tan\beta$=10 and sgn$\mu > 0$. The bottom line corresponds to the stau NLSP.

Here, $m_{\tilde{\tau}}$ and $m_{\tilde{G}}$ are the masses of the stau and gravitino, respectively, M_* is the Planck mass, $\hbar$ is Planck's constant, Γ is the decay width of the stau into the tau and gravitino and τ is the stau lifetime [3] [20]. In this scenario, the stau will always decay into its SM counterpart, the tau lepton, and a gravitino.

The lifetime of the stau, then, depends only on the masses of the stau and gravitino and the Planck mass, which one should expect, since gravity mediates the interaction. As such, the lifetime of the stau naturally falls into the approximate range 10^4 s – 10^8 s, where the most favourable lifetime, from cosmological constraints, is about 37 days [5] (see section 1.3).

Essentially, the NLSP becomes a stable massive particle (SMP) [21], where stable refers to the fact that its lifetime is long enough for it to travel a significant distance away (on the order of 10 m – 1000 m) from its production point

[3] One should not confuse the τ that denotes the stau lifetime with the τ that denotes the tau lepton particle, where the reference to each in equation 1.9 should be unambiguous.

before decaying [4]. This has many implications for next-generation collider experiments, where it is possible that one may be able to detect direct evidence of SUSY. Because of its long lifetime, the SMP will travel a far distance from the interaction point after depositing only a fraction of its energy in the detector systems. Thus, if the design of the detector is not suited to searching for long-lived, slow moving particles, the signal from the SMPs could be lost.

1.3 Motivation

SUSY is quite possibly the most promising theory beyond the SM that will allow us to describe the new physics that we expect must exist for those reasons that section 1.1.1 covers. This, in and of itself, is the main motivation behind any SUSY study. Nevertheless, because the study of SUSY and SUSY breaking can take on a seemingly infinite number of guises, one must attribute some justification to the specific SUSY model that one is considering.

Jonathan Feng best addresses the motivation to study mSUGRA with a gravitino LSP and stau NLSP in [5]. Since the gravitino couples only gravitationally, it is a superweakly interacting massive particle (superWIMP). As such, it becomes an excellent dark matter candidate. If the gravitino is not the LSP, then its late decays will require reheating temperatures $T_{RH} \lesssim 10^5$ GeV k_B^{-1} – 10^8 GeV k_B^{-1}, which contradicts the leptogenesis requirement that $T_{RH} \gtrsim 3 \times 10^9$ GeV k_B^{-1}. If the gravitino is the LSP and does not decay, then this is not a problem, where constraints allow reheat temperatures on the order of 10^{10} GeV k_B^{-1}.

Scenarios with a neutralino NLSP lead to excess hadronic energy in the early universe and are thereby in conflict with big bang nucleosynthesis (BBN) successes, unless some mechanism is able to highly suppress these decays. Also, while the stau lifetime, as equation 1.9 shows, naturally falls into the range 10^4 s – 10^8 s, cosmic microwave background (CMB) and BBN constraints place an upper limit on the stau lifetime of roughly one year, since a cold universe

[4] So, one may prefer to use the term pseudo-stable when referring to these particles, even though some literature, notably [21] prefers the term stable.

will not effectively thermalize the decay products from very late decays. Nevertheless, NLSP decays that occur late enough to have their decay products thermalize according to the CMB and BBN constraints may be able to destroy ^{7}Li, which would bring the predicted levels of ^{7}Li in the universe down to the level that we observe. Thus, the stau, with a lifetime of approximately 37 days, is favourable over other choices as the NLSP.

1.4 Upward-going muons

As Super-Kamiokande observed in [22–24], there seems to be a natural flux of muons arriving at the earth's surface from within the earth itself. One cannot explain this effect through the passage of high energy cosmic ray muons through the earth, because, while muons are weakly ionizing, so that they can traverse a long distance through matter with little impediment, a muon will generally range-out over the 1-13000 km distance it would travel through the earth to arrive upward-going at the earth's surface. As such, one attributes the upward-going muon flux to high energy atmospheric muon neutrinos that interact within the earth.

Since neutrinos only interact weakly, they are able to pass through the earth with almost no hindrance. Nevertheless, since the distance the neutrino must travel is so huge, the probability that it will interact with matter on its journey becomes non-negligible. Thus, if a muon neutrino interacts with matter via a charged current interaction as it passes through the earth, then the result will be the production of a muon, with the conversion of the nucleon with which the interaction took place into a neutron if it was a proton, or vice versa. If this interaction takes place sufficiently far within the earth, then the muon will be able to make it through the remaining distance of the earth, where it will contribute to the upward-going muon flux at the surface.

Like the muon neutrino, electron and tau neutrinos can also undergo charged current interactions as they pass through the earth, which lead to the production of electrons and tau leptons, respectively. Electrons, with such a small mass, range-out very quickly in matter and tau leptons, with their large mass

and small lifetime, promptly decay. This decay can occur through leptonic channels, producing muons that contribute to the upward-going muon flux. Yet, because of branching ratios and kinematics, these muons account for less than 3% of the total upward-going muon rate [22]. Thus, unlike muons, one neither observes an upward-going electron flux nor an upward-going tau lepton flux. There is also the possibility that these charged current neutrino interactions can lead to the production of high energy staus within the earth, which could arrive upward-going at the earth's surface with a signal that is similar in appearance to the upward-going muons [25]. Even so, the Super-Kamiokande data agrees well with the predictions of the SM with the inclusion of neutrino oscillations (see below) and one presently does not observe evidence of upward-going staus.

Considering the addition of neutrino oscillations into the SM [26–28], whereby a neutrino from one generation may change into a neutrino from another generation via some unitary CKM-like matrix transformation of the neutrino weak eigenstates into their mass eigenstates, one should recognise that the large distance the neutrinos traverse through the earth could be far enough for this generational mixing to occur. In fact, this does happen, with a transformation probability of

$$P(\nu_1 \rightarrow \nu_2) = \sin^2(2\theta)\sin^2(\pi x/\lambda)$$
$$\lambda = \frac{4\pi E_\nu \hbar}{\Delta m^2 c^4} \approx 2.48\left(\frac{E_\nu}{1\text{MeV}}\frac{1\text{eV}^2}{\Delta m^2 c^4}\right)\text{m}, \tag{1.10}$$

where Δm is the mass difference between the two neutrino mass eigenstates (where the subscripts 1 and 2 denote this difference), θ is the mixing angle upon which one builds the transformation matrix and E_ν is the neutrino energy, which, because Δm is so small, one considers to be the same before and after the generational change. Also, λ is the characteristic length over which the neutrino undergoes an oscillation, in units of metres.

Thus, as muon neutrinos pass through the earth, there is a finite probability that they will oscillate into a different neutrino flavour, with the effect of reducing the upward-going muon flux at the earth's surface. The Super-Kamiokande collaboration also observed this phenomenon, where the upward-going muon

rate was consistent with neutrino oscillations [22–24].

Chapter 2

ATLAS and the LHC

2.1 The Large Hadron Collider

The Large Hadron Collider (LHC) [29–31] has a name that aptly suits its physical attributes: the machine is huge, with a circumference of 27 km, and fosters one of the most ambitious physics research programs in the history of the discipline. The host site of the LHC is the European Organisation for Nuclear Research (CERN), near Geneva, where the LHC actually takes over the ring that once housed the Large Electron Positron (LEP) [1] collider [32–34], 100 m below the Franco-Swiss border.

The LHC is a proton-proton collider [2] operating at a centre of mass energy of 14 TeV with a luminosity that will increase from 10^{33} cm^{-2} s^{-1} after the first few years of running (low-luminosity) to a peak luminosity of 10^{34} cm^{-2} s^{-1} (high-luminosity). The beam consists of proton bunches containing approximately 10^{11} protons each, where the temporal separation between bunches is 25 ns. As such, given that the inelastic proton-proton cross section is of the order 100 mb at the LHC centre of mass energy, one expects that approximately 25 interactions will occur every beam crossing at the highest luminosity.

To obtain the 7 TeV beam energy, the LHC relies on an injector chain that will increase the energy of the protons in the beam in sequential steps.

[1] The removal of LEP from its tunnel to make room for the LHC took place in 2000.

[2] The machine can also accelerate heavy ions, an example of which are lead, where the centre of mass energy is 1150 TeV and the luminosity peaks at 10^{27} cm^{-2} s^{-1}.

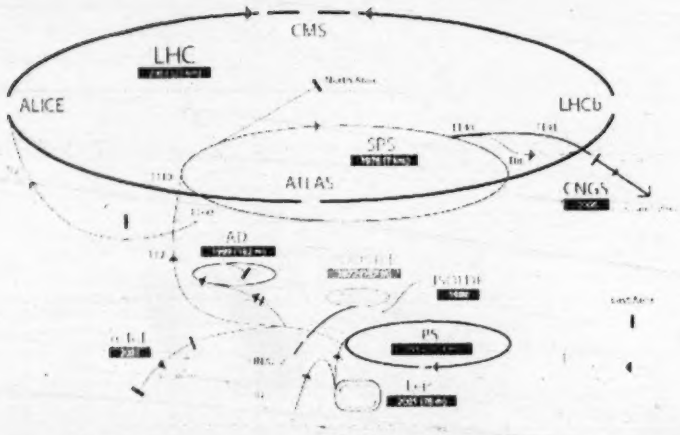

Figure 2.1: The LHC injector chain consists of four main components: the Linac2, the PSB, the PS and the SPS, which successively increase the energy of the protons to 450 GeV before injecting them into the LHC ring [35].

This chain, as figure 2.1 shows, consists of four main components. The Linac2 linearly accelerates protons to an energy of 50 MeV before passing them to the Proton Synchrotron Booster (PSB). The PSB then pushes the proton energy up to 1.4 GeV, whereupon they pass to the Proton Synchrotron (PS), which subsequently increases the proton energy to 25 GeV. Finally, the protons move into the Super Proton Synchrotron (SPS), where they attain an energy of 450 GeV. One then requires the LHC to ramp the proton energy up to its final energy of 7 TeV.

Superconducting electromagnets, at a temperature of 1.9 K, guide the proton beams around the LHC ring in vacuum conditions. These magnets include 1232 14.3 m long dipoles that bend the beam in the beam pipe, with a peak field of 8.33 T at a nominal current of 11.7 kA, and 392 quadropole magnets that focus the beams so that they will collide within the detectors that lie along the beam line [36]. Figure 2.2 shows a diagram of the LHC dipole magnets.

There are four main experiments that the LHC will service – ATLAS, CMS [38, 39], ALICE [40] and LHCb [41] – where figure 2.1 displays the arrangement of these experiments on the LHC ring. ATLAS, the experiment under discussion in this thesis, and CMS are general-purpose detectors with wide-ranging physics programs, covering topics spanning from the search for

Figure 2.2: The image shows the LHC dipole magnets, where one can see the superconducting coils that make up the magnet [37].

the Higgs boson to the search for supersymmetry, extra-dimensions and other exotic physics [3]. ALICE will study heavy ion interaction-induced plasmas and LHCb will concern itself with the study of bottom quark physics, including a study of CP-violation in the B-hadron system.

2.1.1 Operating schedule

From [43, 44], in a 52 week year, a typical LHC operating schedule will be broken into two periods. The first period will consist of 32 weeks of beam operation and the second will consist of a 20 week shutdown period with no beam, which one generally reserves for detector servicing. A further sectioning of the first period consists of eight four week periods where there will be 25 days of beam running and three days of technical stop. As a result, there should be 200 days of beam operation per year.

2.2 ATLAS

ATLAS (A Toroidal LHC ApparatuS) [3, 45], a picture of which figure 2.3 shows, is a general purpose experiment whose design enables it to pursue

[3]For a comparison between ATLAS and CMS see [42].

an extensive physics program. This program ranges from new measurements in the SM to discovering physics that lies beyond the reach of the SM [3]. With the increased luminosity and larger cross-sections of the LHC, ATLAS will enable high precision tests of QCD, electroweak and flavour physics. The number of interactions occurring per beam crossing will lead to a top quark production rate on the level of several Hz, which will allow for tests of top quark coupling and spin. Also, if the SM Higgs boson does exist, ATLAS, as a result of the high LHC luminosity and the expectation that the Higgs mass lies at the electroweak scale, will be able to find it, where the concentration on this discovery established the focus of many ATLAS subsystems, descriptions of which follow in the upcoming sections. ATLAS will also facilitate a search for physics processes that lie outside the SM, including a search for beyond-the-SM Higgs particles, like the A and $H^{\pm}$ of the MSSM. Also, ATLAS will perform a search for SUSY, where, assuming R-parity conservation, decays of SUSY particles will lead to a signature of large missing transverse energy (E_T^{miss}), with the possibility of an excess of hard isolated photons in the final state [4]. Aside from SUSY, ATLAS will also conduct a search for evidence of extra dimensions, which, with the production of weakly interacting gravitons, will have a signal similar to SUSY with large E_T^{miss}. Other signatures of large extra dimensions include anomalous high-mass dijet production or the production of micro-black holes, which will uniformly decay into SM particles with a resulting high-multiplicity jet production [46].

2.2.1 The inner detector

The innermost component of ATLAS, aside from the beampipe, the inner detector [47, 48] consists of 3 distinct, yet complimentary, sub-detectors: the pixel detector, the semiconductor tracker (SCT) and the transition radiation tracker (TRT). The main purpose of the inner detector is to provide high-precision tracking [4] and momentum measurement, for which it lies inside a uniform 2 T solenoidal magnetic field. Figure 2.4 shows how the three

[4]One requires high-precision tracking for such things as secondary vertex measurement and for the identification of particles within jets that are not actually jet-constituents.

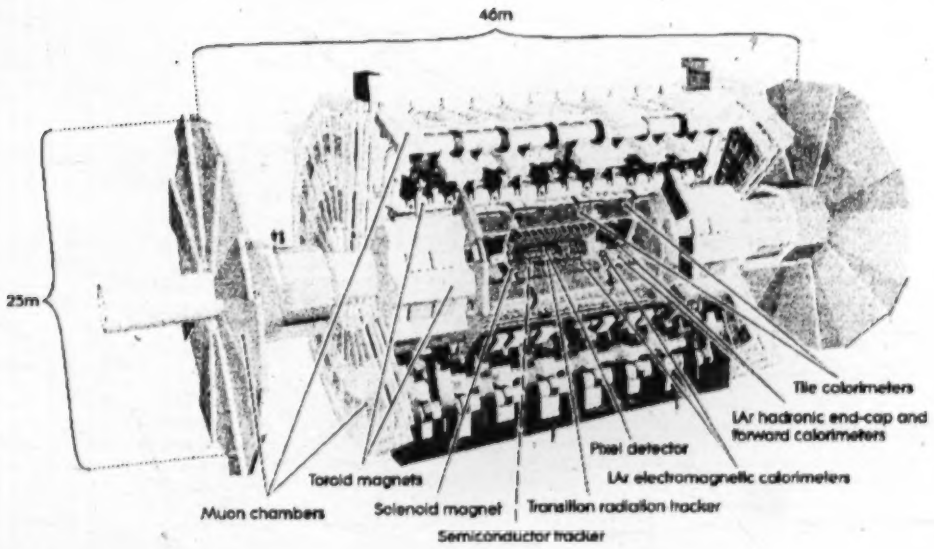

Figure 2.3: There are four main subsystems comprising the ATLAS detector. From the inside out, they are, respectively, the inner detector, the calorimetry, consisting of both electromagnetic and hadronic calorimetry, the muon spectrometer and the magnet system (which really spans the whole detector) [3].

components of the inner detector sit together.

The pixel detector

As one can see in figure 2.4, the pixel detector is the innermost of the inner detector components, residing as near as it possibly can to the beam pipe. The three barrel layers of the pixel detector extend from an inner radius of 4.55 cm to an outer radius of 24.2 cm and its encap, consisting of three sensitive wheels, reaches out to ± 65.0 cm in z.

The pixel detector is able to achieve the highest granularity of the three tracking detectors through the use of 50×400 μm^2 silicon pixels, where the detector utilises a total of approximately 140×10^6 pixels and 80.4×10^6 readout channels. Both the barrel layers and endcap disks have an intrinsic accuracy of 10 μm in R-ϕ and 115 μm in z for the barrel and R for the endcap, where, typically, each track crosses three pixel layers. This allows for a high-precision set of coordinate measurements very close to the interaction

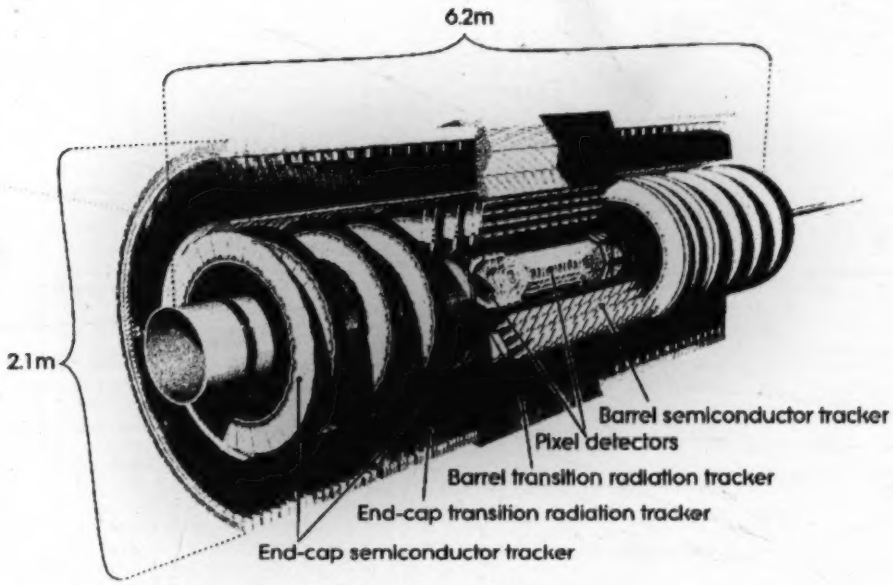

Figure 2.4: The ATLAS inner detector consists of three components: the pixel detector, the SCT and the TRT, each with a barrel and an endcap section [3].

point, which is essential for such things are secondary vertex measurement and primary vertex identification amidst event pile-up.

The semiconductor tracker

Like the pixel detector, the SCT uses semiconducting silicon technology as its active detection medium, where the silicon takes the form of microstrips of length 2×6.4 cm and pitch 80 μm. As such, the granularity of the SCT is not as high as that of the pixel detector, consisting of only 6.3×10^6 readout channels. In the barrel region, one set of strips runs parallel to the beam direction, providing a ϕ measurement and in the endcap one set of strips running radially accomplishes this. Both the barrel and the endcap have a set of stereo strips set at an angle of 40 mrad for the second coordinate measurement.

The SCT, as figure 2.4 shows, consists of four layers in the barrel region, extending from an inner radius of 29.9 cm to an outer radius of 51.4 cm, and 9 wheels in the endcap region, reaching out to $\pm$273.5 cm in z with radii between 27.5 cm and 56.0 cm. Because of this, the SCT is able to make four spatial

measurements per particle track, where the track typically crosses eight layers of the SCT (four corresponding to each spatial direction).

The transition radiation tracker

The tracking detector lying farthest from the interaction point is the TRT, with a barrel section that extends radially from 56.3 cm to 106.6 cm and along z to ±71.2 cm and an endcap with a radial extension between 64.4 cm and 104.4 cm and a half-length in z of 93.1 cm. Consisting of 4 mm diameter polyimide straw tubes surrounding a central 31 μm diameter gold-plated tungsten anode, the TRT is able to provide nearly continuous tracking in the outer tracking sector, where each track will impart approximately 36 hits in the TRT. These tubes contain a mixture of xenon, carbon dioxide, and oxygen gas, which enhances one's ability to distinguish electrons from pions, since the electrons passing through a radiator between the tubes will cause the creation of transition radiation that the gas mixture can detect.

An intrinsic accuracy of 130 μm accompanies the R-ϕ coordinate measurement, which, since the tubes lie parallel to the beam direction in the barrel and lie radially in the endcaps, is the only information the TRT is able to provide. The TRT consists of approximately 3.51×10^5 readout channels. Figure 2.4 shows a picture of the TRT inside the inner detector.

2.2.2 The calorimetry

The ATLAS calorimetry lies in the area between the inner detector and the muon system, consisting of both electromagnetic (ECAL) and hadronic (HCAL) calorimeters. The main purpose of the calorimetry is to provide a measurement of E_T for electrons, photons and jets, as well as to provide a measurement of E_T^{miss}. Additionally, the calorimetry can provide position and direction information for these objects and aid in performing particle identification.

Figure 2.5 shows the layout of the calorimetry. The electromagnetic calorimetry lies closest to the interaction point in order to intercept electrons/positrons and photons traversing the detector, whereas hadrons, interacting strongly, will

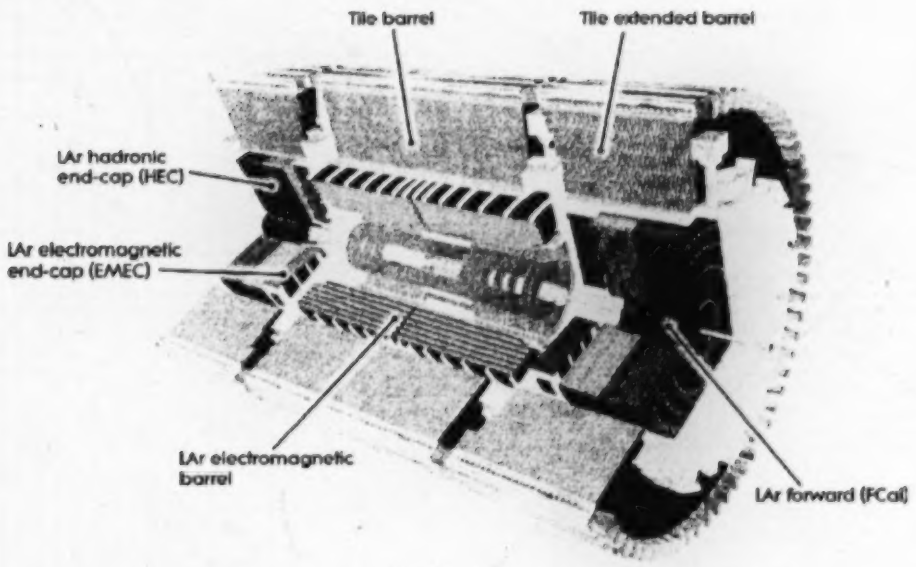

Figure 2.5: The ATLAS calorimetry consists of both an electromagnetic and a hadronic calorimeter, where the HCAL contains the barrel tile HCAL, liquid argon endcap HCAL and FCAL subsystems [3].

generally pass completely through the electromagnetic calorimetry, depositing only a fraction of their energy there. For this reason, the hadronic calorimetry consists of three subsystems lying outside of the electromagnetic calorimetry: the tile HCAL in the barrel, the liquid argon HCAL in the endcap region and the forward calorimeter (FCAL) near the beam pipe in the extreme forward region of ATLAS.

Each of these calorimetry components has a sort of tower geometry, whereby each calorimetry module points toward the interaction point. Figures 2.6 and 2.7 show this tower structure of the ECAL and tile HCAL modules, respectively. For the FCAL, since it is not quite pointing, one groups its internal tube structure into tower-like clusters. This geometry is useful for jet energy measurements, since the towers project back to the interaction point, along the direction of the jet energy deposition.

The electromagnetic calorimeter

As figure 2.5 shows, the ECAL [3, 49] is the innermost component of the calorimetry, consisting of both a barrel and an endcap section, which provide coverage out to $|\eta| < 3.2$. The ECAL consists of lead absorbers with kapton electrodes that sit in a bath of liquid argon, which a cryostat maintains at a temperature of 89.3 K [50]. The absorber plates and electrodes use an accordion geometry, as figure 2.6 displays, in order that the azimuthal coverage will have no holes through which particle data may be lost. The accordion geometry also reduces the amount of time the electrodes require to obtain the ionization signal, which is essential in the high interaction rate environment of ATLAS. In fact, it is the high radiation rate in the volume of the ECAL that warrants the use of liquid argon [50] as the detection medium. Liquid argon is inherently radiation hard, because of the ability of one to cycle the liquid through the detector.

The granularity of the ECAL, as figure 2.6 shows for the barrel region, decreases as the radial distance from the interaction point increases, thus providing higher granularity measurements closer to the interaction point, mimicking the style of the inner detector. From the inner barrel layer to the outer barrel layer, the granularity in $\eta \times \phi$ changes from 0.003125 $\times$ 0.098 to 0.025 $\times$ 0.0245 to, in the outer layer, 0.05 $\times$ 0.0245. The endcap region has an average granularity of 0.019 $\times$ 0.1 in the inner layer, which changes to approximately 0.025 $\times$ 0.025 in the middle layer and 0.050 $\times$ 0.025 in the outer layer. One requires this high granularity in the ECAL region in order to correctly measure the positions of electrons/positrons and photons. The identification of the electrons/positrons and photons occurs via the examination of electromagnetic shower profiles; but, since their shower profiles are very similar, one uses track matching in the inner detector to distinguish between them, which is another reason why the inner detector requires such high granularity.

The ECAL relies on the electromagnetic interactions of charged particles as they pass through the lead absorbers in order to perform its energy measurement. A photon incident on the ECAL will, as it traverses the thickness of

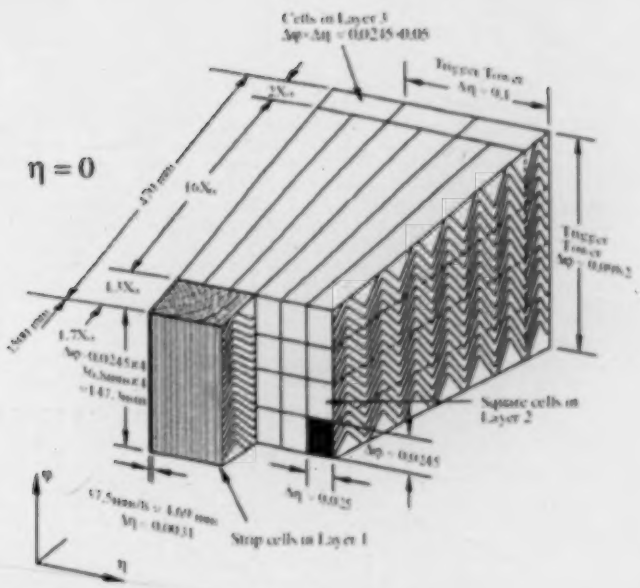

Figure 2.6: The accordion geometry of the ECAL allows for complete azimuthal coverage, with no cracks [3].

the ECAL, convert into an electron/positron pair. Just as with electrons that are incident on the ECAL surface, as these electrons pass through the ECAL, they result in bremsstrahlung, or breaking radiation. This subsequently converts into electron/positron pairs, which result in further bremsstrahlung and so on, a process to which one refers as an electromagnetic shower. The shower ionizes the liquid argon as it passes through and, in an electric field of 2 kV, the ionization electrons then drift toward the kapton electrodes, where the number of ionization electrons incident on the electrodes is proportional to the energy of the shower.

The hadronic tile calorimeter

Lying directly outside the ECAL in the radial region 2.28 m to 4.25 m is the tile HCAL barrel [3,51], which consists of a central barrel 5.8 m in length and two extended barrels each 2.6 m in length. Each barrel consists of 64 modules of width 0.1 in ϕ, an image of which one can see in figure 2.7.

This calorimeter uses lead plates as the absorber material and plastic scintillator layers as the active medium. One can use plastic scintillator in the

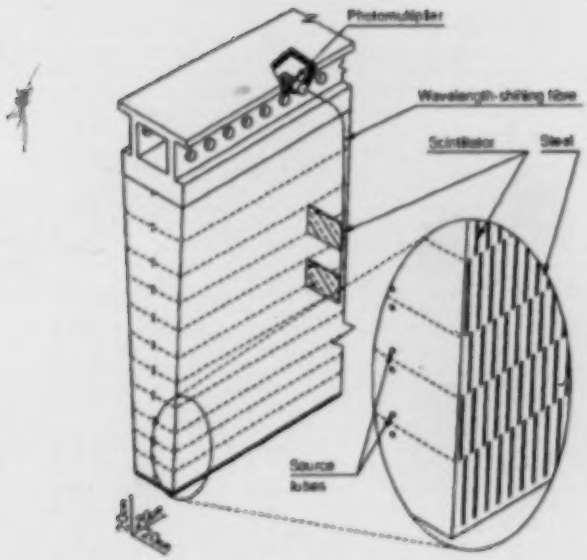

Figure 2.7: The tile HCAL consists of 64 tower modules containing layers of lead and plastic scintillator. Photomultiplier tubes capture the wavelength-shifted light that the scintillators emit [3].

barrel region of the hadronic calorimeter because the radiation rate is much lower there, since the ECAL largely reduces this rate. One uses the plastic scintillator in place of the liquid argon, since it is a more cost-effective way to perform the measurement of hadronic energy deposition. Photomultiplier tubes (PMTs), which obtain the signal from the plastic scintillator via wavelength shifting fibres, count the number of photons that a charged particle passing through the plastic scintillator produces. The number of photons the plastic scintillator emits is proportional to the energy that the charged particle that caused the production of the light deposits there.

The liquid argon endcap calorimeter

The HCAL endcap uses liquid argon as its active detection medium and has copper absorber plates. The high radiation rates in the endcap region of ATLAS necessitate the use of the liquid argon, since it is inherently radiation hard. The HCAL and the ECAL share the endcap liquid argon cryostat.

The liquid argon endcaps have an inner radius of 47.5 cm and an outer

radius of 203.0 cm and cover the range $1.5 < |\eta| < 3.2$, lying just outside the ECAL endcaps. An endcap consists of two wheels, each consisting of 32 wedge-shaped modules. The inner endcap wheels utilise 24 copper plates, each 25 mm thick, with an 8.5 mm thick liquid argon gap in between every pair of plates that three electrodes split into four drift regions of approximately equal volume. The outer wheel has a more coarse sampling, using only 16 copper plates per module. The granularity of the readout is 0.1×0.1 in $\eta \times \phi$ in the region $|\eta| < 2.5$ and is 0.2×0.2 for larger $|\eta|$ values.

The forward calorimeter

The FCAL sits very close to the beam pipe, with an inner radius of only approximately 7.2 cm, and covers the range $3.1 < |\eta| < 4.9$ in three longitudinal sections. This extremely forward region of ATLAS receives the highest particle flux; thus, the FCAL must be able to withstand very high radiation doses and, as such, it uses liquid argon as its detecting medium. The liquid argon fills 0.250 mm gaps amid copper absorber in the first longitudinal section of the FCAL, 0.375 mm gaps in the second section of tungsten absorber and 0.500 mm gaps in the third section, which also consists of tungsten absorber, where figure 2.8 shows the layout of the liquid argon gaps with respect to the absorber in the first section. The high density of the FCAL requires these small layers of liquid argon, where, in order to obtain a signal from those particles entering it, the FCAL must have a large interaction length in its relatively short physical length of only 138.5 cm, warranting its high density.

2.2.3 The muon system

Because muons are low-ionizing particles, they will generally pass through the inner detector, where, since it is charged, the muon will leave a track, and the calorimetry, where the muon will deposit only a small fraction of its energy [5]. As such, the ATLAS muon system [3, 52] is the outermost detector

[5] In fact, the inner detector and calorimetry, comprising a total interaction length of approximately 11λ, act as background suppressors for the muon system, stopping almost everything except the muons from reaching it. Particles that punch through these systems or neutrons or photons in the MeV range that arise due to secondary interactions are some

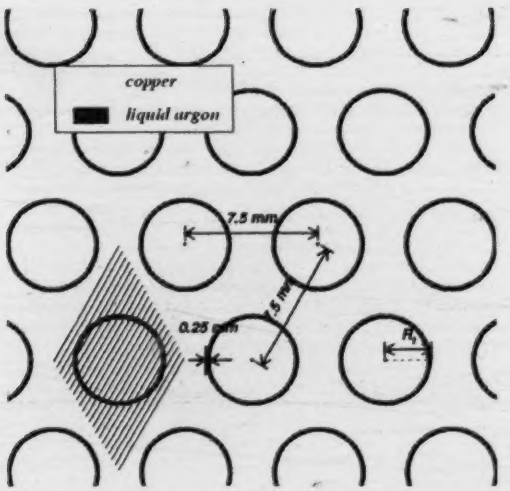

Figure 2.8: The first section of the FCAL consists of hexagonally-arranged 0.250 mm liquid argon gaps with copper electrodes inside the liquid argon layers [49].

component, where the fields of the barrel and endcap toroid magnets (see section 2.2.4) exist specifically to bend the muon trajectory as it passes through the muon system, thus enabling a measurement of the muon momentum.

The muon system, as figure 2.9 displays, actually consists of four subsystems. The monitored drift tubes (MDTs) and cathode strip chambers (CSCs) are precision measurement stations and the resistive plate chambers (RPCs) and thin gap chambers (TGCs) are dedicated trigger stations. In fact, the muon system, taken as a whole, can stand on its own as a muon detector, since it is able to reconstruct the positions and arrival times of the muons with great accuracy.

The monitored drift tube chambers

The MDT chambers are precision measurement devices covering a range $|\eta| < 2.0$ (and $2.7 < |\eta| < 2.0$ in the very outer tracking layer of the endcap). There are three MDT chamber layers in the barrel covering a radial range of 4.5 m to 10.5 m, where the length of each layer increases as its distance from the interaction point increases. The endcap consists of two small and two large

background sources that one could see in the muon spectrometer.

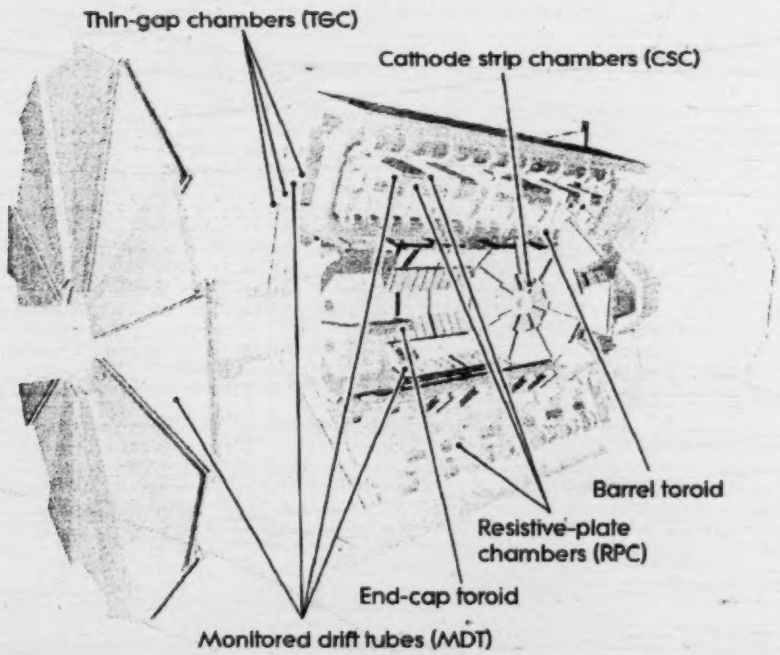

Figure 2.9: The muon spectrometer is the farthest system from the interaction point and consists of four subsystems – the MDTs, the CSCs, the RPCs and the TGCs. The figure also shows the barrel and endcap toroid magnets [3].

MDT chamber wheels. The small wheels reach out to approximately ± 10 m in z, the first large wheel sits at $\pm$ 13.8 m in z and the outer large wheel sits more than 20 m from the interaction point, outside of the forward shielding. Figure 2.9 shows a view of the positioning of the MDT chambers.

Each MDT chamber layer in the barrel and wheel in the endcap consists of two layers of drift tubes, as figure 2.10 shows, with a gap of air separating them. In turn, each of the chamber layers of tubes consists of a stacked layer of three drift tubes. There are a total of 656 chambers in the barrel layers and 516 chambers in the endcap wheels.

The tubes themselves are aluminum, with a 30 mm diameter and a wall thickness of 0.4 mm. A 93 to 7 mixture of argon to carbon dioxide gas fills the tubes, and at their centres lie tungsten-rhenium wire anodes of diameter 50 μm. Each tube has a precision of approximately 80 μm and, when one combines the tubes in a chamber, the precision increases to 35 μm. When a charged particle, notably a muon, passes through the gas mixture, ionization

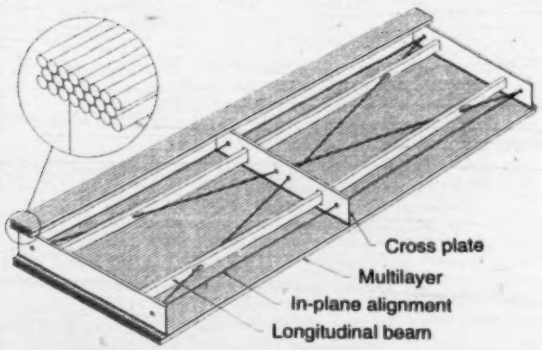

Figure 2.10: The MDT chambers consist of two layers of drift tubes with a layer of air filling the gap in between them. Layers of three drift tubes comprise each of the layers of the MDT chamber [52].

electrons drift toward the anode wire under the influence of a 3.08 kV electric field with a maximum drift time of 700 ns. Although the drift time is much longer than the LHC bunch spacing of 25 ns, the MDTs have a time resolution of 300 ps, which adequately allows for one to determine from which bunch crossing a particle originates. To obtain such good precision, one continuously monitors the MDTs in their frames for any deformations with the use of a built-in optical sensor, thus defining the "monitored" in MDT. Also, since the MDT chambers lie in the magnetic fields of the toroid magnets, they can provide a measurement of the muon momentum, with an approximate resolution $\frac{\delta p}{p} = \frac{45p}{500}$, in units of TeV. A total of 3.72×10^5 tubes comprise the MDT system.

The cathode strip chambers

The CSCs reside in the forward region of ATLAS, covering the range $2 < |\eta| < 2.7$, lying just behind the liquid argon HCAL endcap. As a result of the high particle flux in the forward region, the CSCs are multi-wire proportional chambers, since these are better able to cope with high occupancy rates of up to 1000 Hz cm^{-2} while maintaining a good timing resolution of 7 ns. The chamber spatial resolution is approximately 0.040 mm in η and 5 mm in ϕ (a result of the different pitches of the readout channels). Also, the CSCs tilt at an angle of 11.59° with respect to the beam axis, as figure 2.11 shows, to

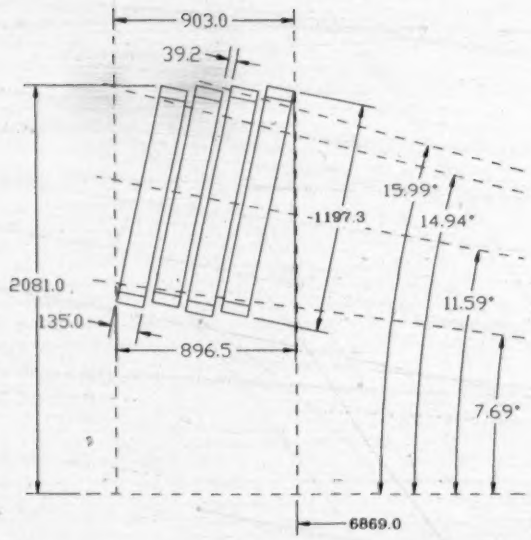

Figure 2.11: In order to provide better coverage in the forward region, the CSCs tilt at an angle of approximately 11.59° [52].

allow for better coverage in the forward region. The active detection medium for the CSCs is a gas mixture of 80 to 20 argon to carbon dioxide [3].

The resistive plate chambers

Dedicated trigger detectors, the RPCs reside in three layers in the barrel region, as figure 2.9 shows. The purpose of these layers is to provide a fast LVL1 trigger decision with reduced-granularity position measurements, while the ATLAS trigger (see chapter 3) bases subsequent decisions on the higher granularity data from the MDTs. To facilitate this, the RPC layers cover both sides of the middle and one of either side of the outer MDT chamber layers in the barrel, having the same length as those MDT chambers.

The RPCs are gaseous parallel-plate detectors with a typical space-time resolution of 1 cm $\times$ 1 ns. As figure 2.12 shows, a RPC has two planes, each consisting of two sets of readout strips, one in the η direction and the other in the ϕ direction, where each plane constitutes a gas volume. These strips cover two resistive bakelite plates that insulating polycarbonate spacers hold parallel at a separation distance of 2 mm. A uniform electric field of a few kV

mm^{-1} between the bakelite plates causes avalanche multiplication of ionization electrons that originate from charged particles passing through a gas mixture of 94.7 to 5.0 to 0.3 tetrafluoroethane to isobutane to sulphurhexafluoride. There are a total of 544 RPCs in the three barrel layers.

The thin gap chambers

The TGCs are dedicated trigger detectors that are meant to provide a fast trigger decision in the endcap region and to provide a measurement of the ϕ coordinate in order to compliment the measurement capacity of the MDTs. There are four TGC layers consisting of three doublets and one triplet, schematics of which figure 2.13 shows. Thus, a total of seven TGC layers surround the first large MDT wheel, where the last doublet lies just outside the inner small MDT wheel, as figure 2.9 displays.

Thin gap chambers are similar to multi-wire proportional chambers, where the wire-to-wire distance of 1.8 mm is larger than the wire-to-cathode distance of 1.4 mm [3]. The 50 μm anodes lie inside gas layers containing a gas mixture of 55 to 45 carbon dioxide to n-pentane that have a graphite cathode on either side of the volume. The doublets and triplets contain either two or three of these gas layers, respectively, which layers of paper honeycomb separate by a distance of 20 mm. There are a total of 3588 anode-containing gas volumes in the TGC system.

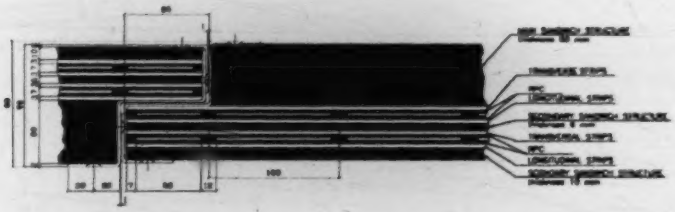

Figure 2.12: The RPCs consist of two doublet layers of strips, where each doublet contains one set of transversal strips and one set of longitudinal strips. Polystyrene comprises the sandwich structures [52].

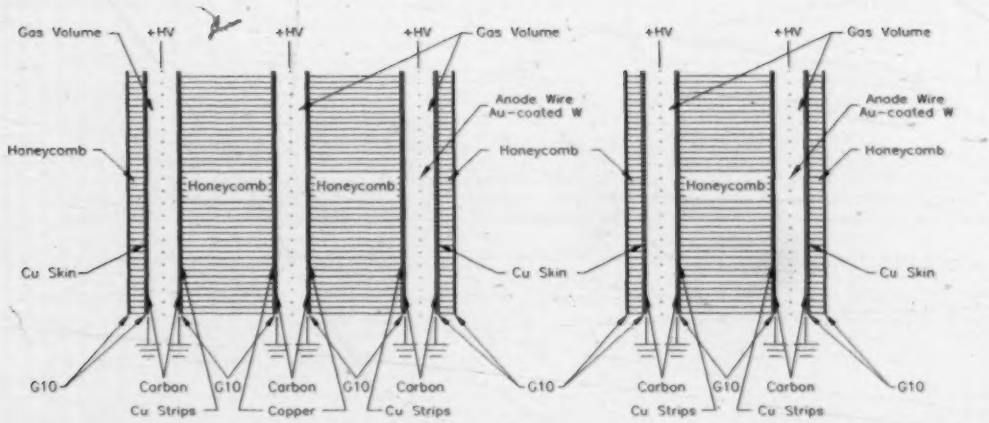

Figure 2.13: The TGC chambers, a doublet on the right and a triplet on the left, consist of two or three gas volumes, respectively, with layers of paper honeycomb separating them [52].

2.2.4 The magnet system

As figure 2.14 shows, the ATLAS magnet system [53–57] consists of three subsystems: the barrel solenoid, the barrel toroid and the endcap toroids. The barrel solenoid, with an inner radius of 1.23 m, outer radius of 1.32 m and half-length of 2.65 m, encloses the inner detector. With a radial range of 4.7 m to 10.1 m and a half-length of 12.7 m, the barrel toroid is the largest superconducting magnet ever constructed and contains the central MDT chamber layer and outer two RPC layers. The endcap toroids have a structure that is similar to that of the barrel toroid, but on a smaller scale, with an inner radius of 0.83 m, an outer radius of 5.35 m and a length of 5.0 m.

The conductor is a mixture of aluminum, copper, and niobium-titanium, which, when one holds the temperature at 4.5 K, becomes superconducting. As such, cryostats house the magnets, where liquid helium cools them to their superconducting temperature. Including the cold mass, the solenoid has a mass of 5.7 tonnes, the barrel toroid has a mass of 830 tonnes and the endcap toroids have a mass of 239 tonnes each.

The solenoid contains 1173 coil turns that carry a nominal current of 7.73 kA and have a central field of 2 T along the z-axis. This field provides enough bending power in the transverse plane of the inner detector region to allow

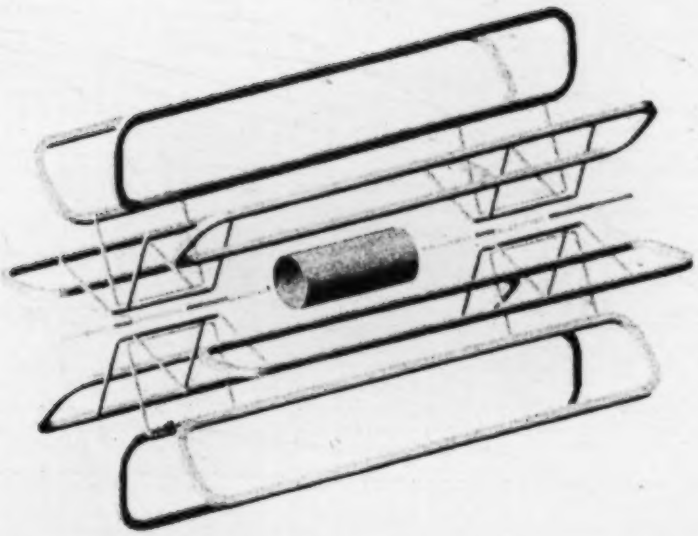

Figure 2.14: The magnet system consists of a central barrel solenoid, a large barrel toroid and its supplementary endcap toroids [53].

one to make an accurate measurement of the p_T of charged particles. Each of the toroids consists of eight coils with an approximate diameter of 40 cm. The barrel uses 120 turns of the conducting wire per coil and the endcaps utilize 116 turns per coil. The nominal current passing through each of these toroids is 20.5 kA, where the barrel has a peak field of 3.9 T and the endcaps have a peak field of 4.1 T. These fields provide additional bending power in the η direction to bend muons that arrive at the outer regions of ATLAS, allowing for muon p_T measurement. Figure 2.15 shows a picture of the total ATLAS magnetic field that each magnet subsystem generates. Figure 2.16 shows the the field integral as a function of η.

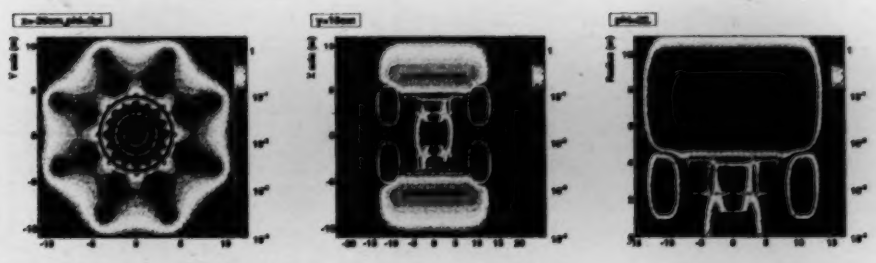

Figure 2.15: The ATLAS magnetic field magnitude is shown on a colour grading scale, where red (image centre) is the highest field (above 1 T). The image on the left is an x-y slice of the field at -20 cm in z and 360° in ϕ. The centre image shows an x-z slice of the field at 10 cm in y. Finally, the right image displays an r-z slice of the field at an angle of 22° in ϕ [58].

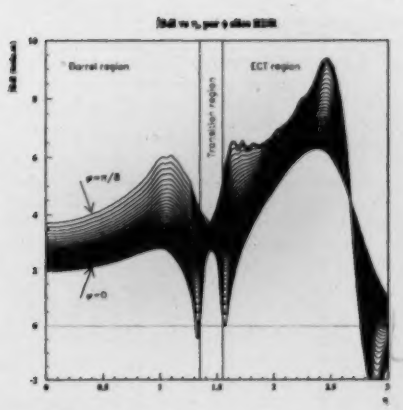

Figure 2.16: The ATLAS magnetic field integral as a function of η [58].

Chapter 3

The ATLAS trigger system

At the LHC design luminosity of 10^{34} cm^{-2} s^{-1} with an inelastic proton-proton cross-section of 100 mb, ATLAS will see an event rate at the level of GHz. One billion particles per second is truly an unprecedented amount of data to handle and, as a result of current technological and data storage capacity limitations, becomes physically impossible to process. Compounding this problem is the fact that, because of their high cross-sections, QCD processes dominate this event rate and those processes, like Higgs production, that are of prime interest to the ATLAS research program become lost in this QCD background. Fortunately, in order to be sensitive to rare processes, one can largely limit the amount of data that one must store. The problem, then, is that one requires a method by which one can extract these interesting physics events from all of those processes that occur.

To facilitate this, ATLAS uses a three-tier trigger system, where each tier successively reduces the data rate to the final writeable rate of approximately 200 Hz. The low-level trigger, level 1 (LVL1), is hardware-based and consists of custom electronics operating at the LHC bunch crossing frequency. The high-level trigger (HLT) is the collective term for the two software-based triggers, level 2 (LVL2) and the event filter (EF), that run on dedicated processor farms and use as input the event data that LVL1 selects. The following sections describe in detail the workings of the ATLAS trigger system [3,59,60] and the last section provides an outline of the cosmic ray trigger.

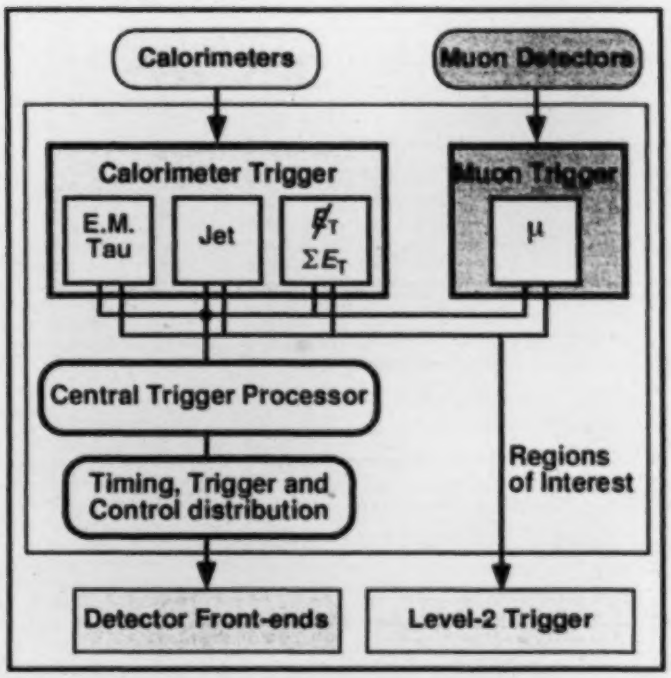

Figure 3.1: A block diagram of the LVL1 trigger.

3.1 The low-level trigger

A hardware-based trigger, LVL1 develops its decisions using information from the calorimeters and the muon detectors at a rate of 75 kHz. The LVL1 calorimeter trigger seeks to separate high-E_T electrons and photons, jets and hadronically-decaying tau leptons, as well as events with large E_T^{miss} and large total E_T from QCD background events. The RPCs and TGCs act as dedicated LVL1 muon trigger hardware components, where the trigger uses them to identify low- and high-p_T muons. By combining the information on different trigger objects, the central trigger processor (CTP) makes the final LVL1 trigger decision, where one can program the trigger menus with up to 256 distinct trigger types. Finally, an optical broadcast network communicates the trigger decision to the front-end electronics and readout systems through the timing, trigger and control system (TTC). Figure 3.1 shows a block diagram of the LVL1 trigger.

Pipeline memories store the information for all detector channels while the

trigger uses the multiplicity of the trigger objects to form its decision. This occurs for each bunch crossing with a target LVL1 latency time of 2.0 μs and an additional latency time of 0.5 μs that one has as contingency. If an event passes the LVL1 trigger selection, then the spatial information of the trigger objects that the pipeline memories were storing is sent to the LVL2 trigger as a region of interest (RoI) (see section 3.2), whereupon the LVL2 trigger will take over and implement a more refined trigger decision, accessing only the limited information in the RoI definition.

The LVL1 calorimeter triggers use approximately 7200 reduced-granularity (0.1×0.1 in $\eta \times \phi$) analogue trigger towers from both the ECAL and HCAL to form its decision with a total latency time of about 2.1 μs. The trigger covers a region that extends out to $|\eta| < 2.5$, which corresponds to the limit of the inner detector and the high-granularity ECAL coverage. A sliding window of 4×4 towers in both the ECAL and HCAL, as figure 3.2 displays, forms the basis of the electron/photon and tau/hadron trigger algorithms [61]. The window slides in steps of one trigger tower in both η and ϕ so that there exists one window corresponding to each trigger tower within the trigger acceptance.

The sum of E_T over a group of towers forms each of six basic elements that comprise this sliding window. The first element consists of four overlapping electromagnetic clusters, each of which is either the vertical or horizontal sum over two electromagnetic towers, as figure 3.2 shows, which one uses to measure the E_T of electromagnetic showers. The next element is a hadronic core that consists of the four hadronic towers comprising the window directly behind the electromagnetic clusters. One uses the sum of these four towers to test for isolation in the HCAL. Four hadronic clusters that one uses to measure the E_T of hadronic showers make up the third element. The sum of each of the electromagnetic clusters with the hadronic core forms the hadronic clusters. Following this are the electromagnetic and hadronic isolation rings, comprising elements four and five, which one uses to test for isolation in the ECAL and HCAL, respectively. The electromagnetic isolation ring consists of the twelve electromagnetic towers that surround the electromagnetic clusters. The hadronic isolation ring consists of the twelve hadronic towers directly be-

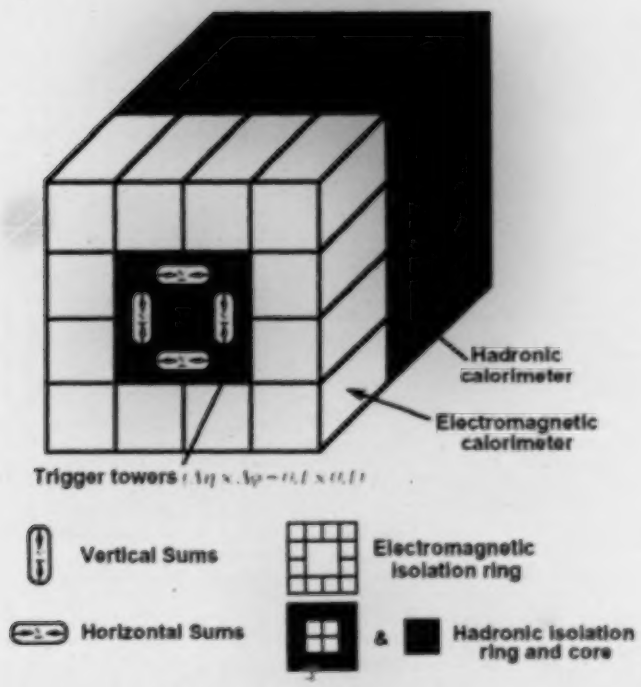

Figure 3.2: The LVL1 calorimeter trigger algorithm uses a window of 4 × 4 electron/photon and tau/hadron trigger towers [3].

hind the electromagnetic isolation ring. Finally, the sixth and last element is a 2 × 2 tower cluster RoI, which is the sum in depth over the electromagnetic cluster and hadronic core and which one uses to identify candidate RoIs [61].

There are 16 sets of trigger E_T thresholds available, where each set is a combination of E_T for cluster energy, electromagnetic and hadronic isolation rings and hadronic core isolation. The electromagnetic cluster trigger utilises eight of these sets directly, where each of the other eight sets are independently programmable to be either an electromagnetic or a hadronic cluster trigger threshold. Based on these thresholds, if the total E_T of an electron/photon or tau/hadron object falls within the trigger threshold requirements, then one considers the window to contain an electromagnetic or a hadronic cluster candidate, respectively.

In addition to this, there exists a jet trigger that searches for jets over units of 2 × 2 trigger towers, or jet elements, out to $|\eta| < 3.2$ (with a forward jet trigger that searches out to $|\eta| < 4.9$). One takes the sum of E_T over the depth

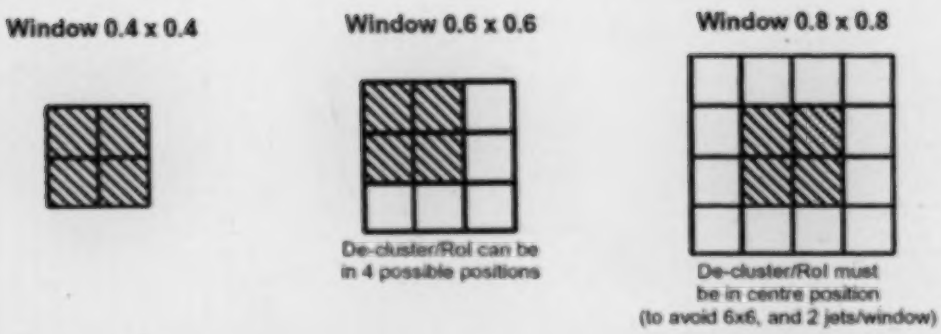

Figure 3.3: The jet trigger windows consist of 2×2 trigger towers, corresponding to 0.2×0.2 in $\eta \times \phi$. Note that in the case of 3×3 jet elements, there are four windows that surround a RoI, so one uses the window with the highest E_T sum [3].

of the ECAL and HCAL towers via sliding jet windows that consist of either 2×2, 3×3 or 4×4 jet elements, as figure 3.3 shows. These windows slide in steps of one jet element in both η and ϕ. If the jet window E_T is greater than one of the eight jet trigger E_T thresholds, then one considers the window to contain a jet trigger candidate and forms a RoI. Note that in the 3×3 case there are four windows surrounding each RoI candidate, so one uses that window with the highest E_T sum.

The calorimeter trigger algorithms construct a RoI for every electromagnetic and hadronic cluster and jet trigger candidate. With respect to the proper granularity of the candidate object (0.1×0.1 for cluster triggers and 0.2×0.2 for jet triggers in $\eta \times \phi$), the RoI information consists of the η-ϕ coordinate of the candidate object and the thresholds the object passed. LVL2 can then access these RoIs.

Finally, there is also an E_T^{miss} trigger in the calorimetry [62,63] that takes the negative sum over all calorimeter cells trigger towers to determine the amount of E_T in the event that the detector is unable to account for. This trigger can also include the energy that a muon failed to deposit in the calorimetry. If the E_T^{miss} sum is greater than 10 GeV, then the trigger constructs a RoI, which the HLT will access.

The LVL1 muon trigger relies on dedicated, finely segmented detectors – the RPCs in the barrel region and the TGCs in the endcap region – to form its

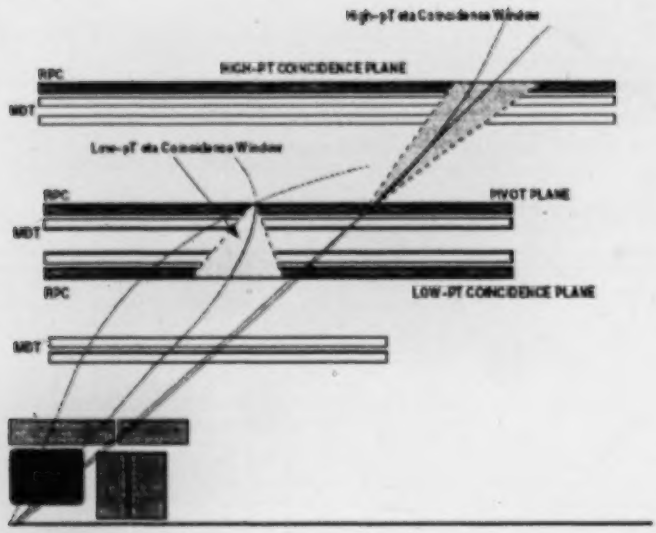

Figure 3.4: The LVL1 RPC trigger scheme works via searching for hits in the inner and outer RPC layers within p_T threshold-defined roads for low- and high-p_T triggers, respectively [3].

decision. Each detector type consists of three trigger stations that envelop the MDT chambers in both regions, where the excellent timing resolution of these trigger chambers allows for unambiguous determination of the bunch crossing.

With a typical space-time resolution of 1 cm $\times$ 1 ns, the RPCs act as the dedicated LVL1 trigger in the muon barrel region, arriving at a trigger decision in a latency time of 2.1 μs. Since one expects low radiation rates in the barrel region, the RPCs have a rate handling capability of approximately 1 kHz cm^{-2}. Each of the three RPC layers actually consists of two RPC doublets, where one doublet follows the η projection, providing a view in the bending plane, and the other lies along the ϕ projection, allowing for the measurement of the second coordinate and for pattern recognition.

The middle RPC layer is known as the pivot plane and lies atop the middle MDT barrel. When a muon generates a hit in this layer, the trigger searches for a matching track in the inner RPC layer within a road surrounding a straight line that connects the position of the hit to the interaction point. This low-p_T trigger requires a 3 out of 4 coincidence in the four RPC doublets

Threshold name	Value	Low-/high-p_T
MU4	Cosmic	Low
MU5	5 GeV	Low
MU6	6 GeV	Low
MU8	8 GeV	Low
MU10	10 GeV	Low
MU11	11 GeV	High
MU15	15 GeV	High
MU20	20 GeV	High
MU40	40 GeV	High

Table 3.1: One can use up to six muon trigger p_T thresholds to search for hits in the inner and outer RPC or TGC layers for low- and high-p_T triggers, respectively. The standard LVL1 trigger consists of low-p_T thresholds MU6, MU8 and MU10 and high-p_T thresholds MU11, MU20 and MU40.

comprising the inner and middle RPC layers. The trigger searches for this track in the inner RPC layer using three independently programmable low-p_T trigger thresholds [64], where the width of the road depends on the p_T cut one chooses: the larger the cut, the narrower the road. Similarly, one can also search for a high-p_T trigger using an additional three high-p_T thresholds, as table 3.1 shows, that run in parallel, for a total of six concurrently searchable thresholds. The high-p_T trigger works in the same fashion as the low-p_T trigger, where the trigger searches the outer RPC layer for a hit matching the muon hit in the pivot plane, again within a p_T threshold-defined road. The trigger requires a 1 out of 2 coincidence in the outer RPC doublet as well as a passing decision in the low-p_T trigger. The sectors of the RPC layers that contain the trigger events then form the RoIs that LVL2 will use. Figure 3.4 shows how these trigger schemes work.

Because the particle flux in the endcap region is so high, TGCs, with a rate capability of approximately 20 kHz cm^{-2}, provide the muon trigger signals there. Even though the time resolution of the TGCs is not as great as that of the RPCs, the TGCs are still able to provide greater than 99% efficiency in bunch crossing identification. The TGCs consist of four planes, with a near inner doublet covering the range $1.05 < |\eta| < 1.9$ and two far doublet planes with a far triplet layer that cover the range $1.05 < |\eta| < 2.4$. Each plane

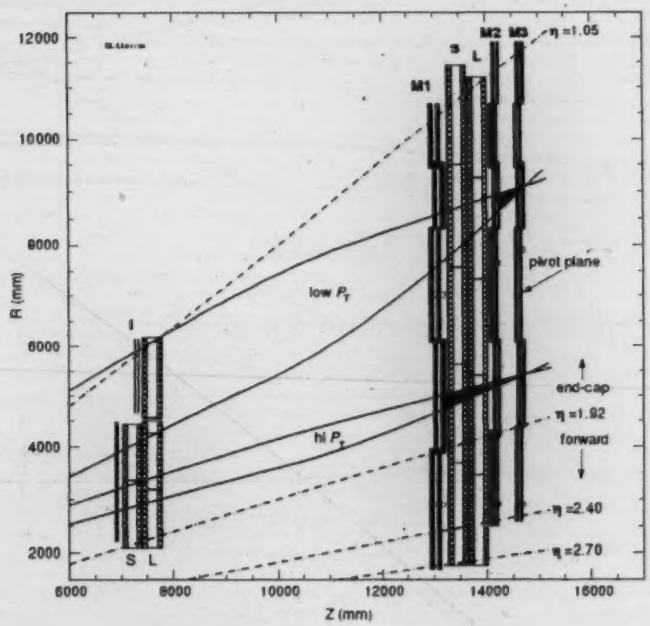

Figure 3.5: The LVL1 TGC trigger scheme works via searching for hits in the doublet and triplet TGC layers within p_T threshold-defined roads for low- and high-p_T triggers, respectively [3].

consists of azimuthally-arranged wire groups that are between 10.8 mm and 36 mm in width in addition to 32 radial strips orthogonal to the wires that provide ϕ measurements. The latency time of the TGCs is approximately 2.1 μs.

The TGC trigger scheme, which figure 3.5 displays, is similar to that of the RPCs, where the pivot plane in this case becomes the outer TGC doublet farthest from the interaction point. The trigger searches for hits in the inner doublet and triplet layers within p_T-dependent coincidence windows that ensconce the straight line path connecting the hit in the pivot plane to the interaction point. Again, there are six independently programmable p_T thresholds equivalent to those that the RPC trigger uses, where three thresholds concern low-p_T events and the other three define high-p_T events. The trigger requires a 3 out of 4 coincidence in the two TGC doublets in order to define a low-p_T trigger, while the trigger necessitates a 2 out of 3 coincidence in the triplet layer in addition to a passing low-p_T trigger decision to form a high-p_T trigger

event [3]. The trigger sector that contains the hit strips and wires then forms the RoI that LVL2 will access.

3.2 Regions of interest

The LVL2 trigger has a monumental task in winnowing the trigger events that the LVL1 trigger selects, especially since it must do so in a latency time of 10 ms. Rather than having the LVL2 trigger access all of the event data for those events that pass the LVL1 trigger decision, ATLAS uses a novel region of interest (RoI) [65] mechanism whereby only a small portion – approximately 1-2% – of the total event data aids in forming the LVL2 trigger decision.

When the LVL1 trigger selects an event, a RoI builder [66] uses the event data to form a RoI, which generally stores information on the η and ϕ positions and the p_T of the candidate object as well as any energy sums if the RoI is in the calorimetry. A dedicated data path sends this RoI information to the LVL2 trigger, which then selectively chooses which data to access according to the type of trigger event it is considering. In this way, the LVL2 trigger only accesses data that it needs to form its decision, which allows the latency time of the LVL2 trigger to be attainable. If one were to require the LVL2 trigger to utilise the entire event data, it would not be able to form a decision with enough speed to allow the data buffers to flush themselves in anticipation of further events, simply due to the event rate.

3.3 The high-level trigger

Consisting of both the LVL2 trigger and EF, the primarily software-based HLT further reduces the writeable event rate by refining the LVL1 trigger decisions. After confirming the LVL1 hypothesis, the LVL2 trigger selects the limited data from the RoI that corresponds to the type of event selection it is considering, where a list of trigger definitions dictates this event type. These trigger definitions can require the LVL2 trigger to search for events containing multiple jets with E_T above certain thresholds, or one or more isolated leptons with E_T, again, above some threshold, et cetera, or some combination thereof.

In other words, if the trigger is considering an electromagnetic cluster event, then it will query the calorimeter RoIs to select the corresponding data. If the event does not pass the LVL2 decision, then the system flushes its memory buffers, without searching for data from subsequent RoIs, such as those from the inner detector that the trigger could use for track matching. In this way, one minimises the amount of data that the LVL2 trigger must access [3]. To make its decision, the LVL2 trigger obtains higher granularity data from the hardware components that correspond to the RoI, which allows for the more refined event selection. The LVL2 trigger operates with a latency time of approximately 10 ms and, via its access to higher granularity data and more stringent event requirements, cuts the trigger rate to 3.5 kHz from the LVL1 75 kHz input rate.

Unlike the LVL2 trigger that accesses limited event information to implement software-based cuts and initial track matching, the EF is a processing farm that has access to the full event information, enabling it to further refine the LVL2 selection and reduce the trigger rate to the final writeable rate of 200 Hz. Each node in the farm is able to manage a number of processing tasks that are actually standard ATLAS event reconstruction and analysis applications [3]. If an event passes the EF decision, the EF appends a subset of the analysis data to the event data that one can use to identify the event during subsequent analyses. Notably, the EF attaches a tag to the event that records into what type of physics stream it sorted the event. Since the EF forms its decision using the complete event data, which is higher in both quality and quantity than the data the previous two trigger levels access, it has an average latency time of 1 s. The EF stage is the first time that all of the event information becomes accessible.

3.3.1 Event selection

The HLT seeds its selection of events containing high E_T electrons using the candidate electromagnetic clusters that the LVL1 trigger finds. Since higher granularity data is now available, the HLT recalculates the energy and position measurements, which allows the triggers to apply more stringent E_T cuts

during their event selections. The use of the shower shape aids in identifying the particle type and, if the trigger selects a candidate electron cluster, then it searches for a matching track among the inner detector RoIs. The trigger can also impart an isolation requirement on the electron candidate. The search for photons occurs in a similar manner, where the shape of the electromagnetic shower aids in the photon identification. Since the photon is neutral, it will not leave a track in the inner detector unless it converts into an electon/positron pair before exiting there; thus, the trigger can only perform track matching if the pair-production occurs.

To identify high-p_T muons, the HLT accesses data that correspond to the RPC or TGC RoI information, whereupon these RoIs seed the identification of track segments in the MDT chambers [3]. Since the MDT information is of higher granularity than that of the RPCs or TGCs, which results in a better determination of p_T, the trigger can require more strict cuts on p_T selection. The trigger then performs a search for a matching track in the inner detector RoIs, which, again, allows for a refinement in the measurement of the muon p_T. If the muon has an energy greater than 20 GeV c^{-1}, then the trigger will also impart an isolation requirement, using information from the ECAL and HCAL.

Finally, the trigger applies more rigid thresholds on jet clustering after recalculating the E_T using higher granularity calorimeter data. This also applies to E_T^{miss}, where, because of the more accurate summing over calorimeter tower data, one can apply higher trigger thresholds of up to 80 GeV when searching for events containing high E_T^{miss}. This signal relies on the full event information from all calorimetry, where $|\eta| < 4.9$, and on information from muon candidates. Also, offline E_T^{miss} reconstruction algorithms exist to ensure its correct calculation, since it is a fundamental signature for many interesting physics processes, including SUSY [62].

3.4 The cosmic ray trigger

The rate one measures for cosmic rays entering the ATLAS cavern is enormous – on the order of kHz for cosmic ray muons alone [67]. As such, it is important to be able to distinguish between this source of background and those interesting physics events that originate from the interaction point. Nevertheless, when cosmic rays become the signal, which is the case when using cosmic ray muons for detector commissioning, the ATLAS trigger scheme, while resolute in finding physics events originating from the interaction point by design, will require significant redefinition. This is, in part, a result of the heavy dependence on pointing of the LVL2 trigger algorithms, where cosmic rays are generally non-pointing. To remedy this, there exists, in addition to the standard ATLAS trigger, a set of dedicated LVL2 cosmic ray muon trigger algorithms that rely heavily on the LVL1 muon trigger architecture. While running, this trigger (MU4) takes the place of one of the six programmable trigger thresholds that table 3.1 lists.

Like the low-p_T trigger in the barrel region, the LVL1 cosmic ray muon trigger [64,68] forms a decision via a 3 out of 4 majority in the η and ϕ strip planes of the inner two RPC layers. If layer RPC2 registers a hit, then the trigger searches for a hit in layer RPC1 within a fully open coincidence window, rather than within a coincidence window that is p_T threshold-dependent. In this way, one removes the necessity to require pointing in the LVL2 trigger algorithms, even though a small constraint on the pointing of the muon remains. This is a result of the electronics cabling, which, since there must be a connection between the electronics in the two RPC layers, generally corresponds to the muon pointing to within 2 m of the interaction point.

In addition to defining a RoI that can seed the LVL2 trigger [1], the hits in these two RPC layers also define the timing of the trigger decision, where the hits must fit into a 25 ns time window, corresponding to the LHC bunch spacing time. If the hits cannot fit into this window, then they will be lost. Consequently, one divides ATLAS into a top and a bottom section, where

[1] One can either use the RPC or MDT information to seed the LVL2 trigger.

most hits will either fit into the top detector decision or the bottom detector decision, but not both, since a muon generally requires more than 25 ns to travel between the two halves. Of course, it is difficult to associate a cosmic ray muon event to a bunch crossing period, because the muons do not originate from the interaction point and, thus, one cannot tag them in the standard way. To overcome this timing dilemma, a special tool exists at LVL2 to calculate the arrival time of the non-pointing muon at each MDT chamber, which allows one to fully exploit the position measurement accuracy of the MDT chambers.

The LVL2 algorithms [69] search for pairs of η and ϕ hits in both RPC layers using as a seed the information they obtain from the RoIs. If they locate a hit pair, the algorithms then fit the pair with a straight line to form a track candidate. Following this, the trigger reads out the MDT information from those tubes surrounding the candidate tracks, where a straight line fit to the MDT information forms the actual muon track. Once again, the non-pointing muon timing tool allows one to determine the precise track segments of the cosmic ray muon events. Simulations show that the distribution between the MDT track segments and the MDT hits has a width of approximately 80 μm, which is close to the MDT precision.

Turning to the endcap region, the physical cross-section of the TGCs is very small with respect to the cosmic ray muons that arrive from above essentially parallel to the TGC surface; thus, few triggers would occur if one were to use the standard TGC LVL1 trigger configuration. Consequently, to increase the cosmic ray muon trigger rate in the endcap region, the trigger requires only one TGC layer to register a hit. Nevertheless, since the TGC electronics require a coincidence between layers to observe a hit, one introduces dummy hits into the TGC layers that envelop the hit layer to form the trigger decision, as figure 3.6 shows. Typically, one chooses the central layer of the TGC triplet as the trigger layer and imparts dummy hits in the inner and outer triplet layers. Because the triplet layers are so closely spaced, a muon that truly originates from the interaction point will almost always register a hit in all three of them, with a track that one can trace to the interaction point and that has a matching track in the inner detector. A cosmic ray muon that triggers because

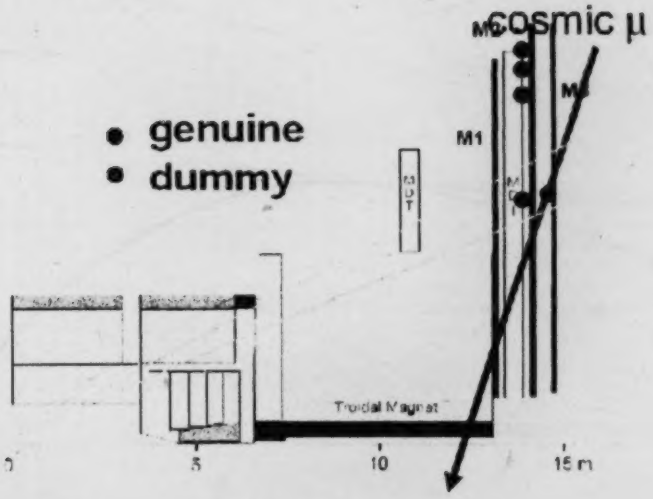

Figure 3.6: One introduces dummy hits into the TGCs to trick the muon trigger into thinking that it has seen a muon that originated from the interaction point. Here, the inner and outer TGC doublets contain the dummy hits, although the inner and outer layers of the TGC triplet work equally well, since the layers are so closely spaced [68].

of the the use of dummy hits will not often have a trajectory that is in line with the interaction point and, therefore, one can inherently distinguish it from the muons that do originate from there. In the end, one essentially tricks the muon trigger into thinking it has seen a muon that originated from the interaction point, resulting in the LVL1 trigger defining a RoI.

Once an event passes the LVL1 trigger decision, the LVL2 trigger algorithms can begin to construct a track for the cosmic ray muon. Again, using a fully open coincidence window, the algorithms search those TGC layers surrounding the layer that registered a hit for either a pair or a trio of hits with which it performs a straight line fit to form a track candidate. If the track candidate is consistent with a potential cosmic ray muon track, then the algorithms access the MDT information from those tubes surrounding the candidate and use it to form the actual cosmic ray muon track, with the same precision as that above.

Chapter 4

Modelling ATLAS and its surroundings

Before this physics study can begin, it is first neccessary for one to develop a simple model of ATLAS to simulate the detector response to the long-lived stau signal. To facilitate this, I use GEANT 3.21 [70] to model the ATLAS detector and overburden. GEANT is a detector description and simulation tool that allows one to simulate the interactions of high energy particles as they traverse matter and pass between volumes.

The model consists of both a description of the ATLAS and overburden volumes, as well as the materials that fill these volumes. ATLAS sits approximately 80 m below ground level in a cavern with layers of rock of varying density surrounding it. There are four access shafts that reach from the top of the cavern to ground level, as well as the two main ATLAS counting rooms perpendicular to the cavern. The ATLAS detector itself sits in the main cavern with its centre defining the interaction point at (0,0,0) m. The ATLAS model represents all subsections of the detector, including the inner detector, the calorimetry, the muon system, the magnet system and the beam pipe and shielding. In turn, I subdivide each of these sytems into its constituent subdetector volumes.

Lastly, I should note that I use the standard list of GEANT material definitions where possible in this simulation. Of course, most volumes consist of a material mixture that is more complicated than consisting of a pure element. In order to adequately model the complicated structure of ATLAS, then, I

use an average material definition to create a smeared mixture for each of the model volumes.

If a volume consists of i materials, then the equivalent thickness T_i of each material comprising the volume is

$$T_i = \%X_o^i \cdot X_o^i, \tag{4.1}$$

where $\%X_o^i$ is the percent of a radiation length X_o^i, in units of length, that material i contributes to the volume. Thus, the total thickness of the component is written as

$$T = \sum_i \%X_o^i \cdot X_o^i. \tag{4.2}$$

As such, the percent of each material by volume V is

$$\%V_i = \frac{T_i}{T}. \tag{4.3}$$

To smear the density of the material over the whole volume, one must place a mass $\rho_i \%X_o^i \cdot X_o^i$ in the volume V, giving

$$\tilde{\rho}_i = \rho_i \%V_i, \tag{4.4}$$

where ρ is the density. Thus, the total density of the component will be the sum of the smeared densities

$$\tilde{\rho} = \sum_i \tilde{\rho}_i. \tag{4.5}$$

Consequently, the percent of each material by mass will be the same as the percent of each by density (since the volume cancels), giving

$$\%M = \frac{\tilde{\rho}_i}{\tilde{\rho}} = \frac{\rho_i \%X_o^i \cdot X_o^i}{\sum_i \rho_i \%X_o^i \cdot X_o^i}. \tag{4.6}$$

To calculate the radiation length of the mixture, which GEANT requires in order to define a material, one can use [70]

$$(\rho X_o)^{-1} = 4\alpha r_o^2 N_{Av} A^{-1} Z(Z + \xi(Z))[\ln(183 Z^{-1/3}) - F_c(Z)], \tag{4.7}$$

where α is the fine structure constant, r_o is the classical electron radius and N_{Av} is Avogadro's number and the radiation length and density are in units

of cm and g cm^{-3}, respectively. Also, A and Z are the effective atomic weight and number, which one can determine by

$$A_{eff} = \sum_i \%MA_i \text{ and } Z_{eff} = \sum_i \%MZ_i. \tag{4.8}$$

The function $F_c(Z)$ is the Coulomb correction function and is written as

$$F_c(Z) = (\alpha Z)^2[(1 + (\alpha Z)^2)^{-1} + 0.20206 - 0.0369(\alpha Z)^2 + 0.0083(\alpha Z)^4 - 0.0020(\alpha Z)^6], \tag{4.9}$$

where

$$\xi(Z) = \frac{\ln(1440Z^{-2/3})}{\ln(183Z^{-1/3}) - F_c(Z)}. \tag{4.10}$$

The sections below outline the exact geometry, layout and material descriptions, including the $\%X_o$, $\%V$ or $\%M$ contributions of each material type to each of the smeared materials I define, for all of the ATLAS subdetector models. The basis for the information in the sections below, unless I state otherwise, is the set of ATLAS technical design reports [45, 47–52, 54–57]. As such, some of the models I create reflect an older version of the detector design than that one may find in [3].

4.1 The inner detector

The inner detector logical volume model is a cylinder with an inner radius of 4.75 cm, an outer radius of 115.0 cm and a half-length of 345.0 cm. It is the innermost volume, just outside of the beampipe, where its dimensions enable it to contain the three subdetectors that comprise it: the pixel detector, the semiconductor tracker and the transition radiation tracker. As with the other logical volumes, I fill the inner detector with air. The three subsections below contain descriptions of the precise geometries and material compositions of the subdetectors. A substantial amount of the information upon which I built the inner detector model comes from [71].

4.1.1 The pixel detector

The pixel detector lies within the inner detector logical volume and is its innermost component. As one can see in figure 4.1, it consists of both a barrel

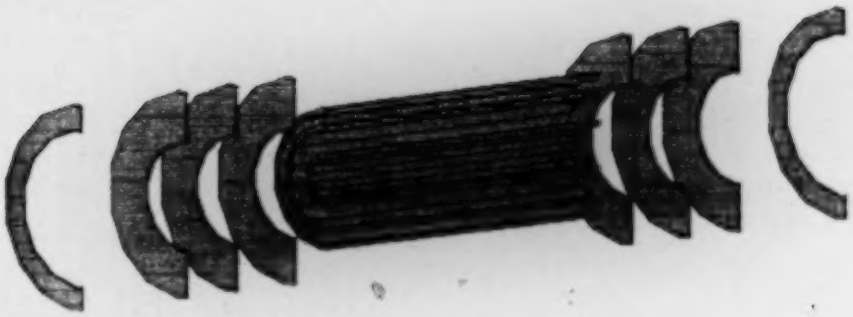

Figure 4.1: The pixel detector.

Barrel/Wheel #	Inner radius (cm)	Outer radius (cm)	Half-length (cm)	z-position (cm)
B1	4.2	5.3	38.5	0.0
B2	10.0	11.1	38.5	0.0
B3	13.2	14.3	38.5	0.0
Wh1	11.0	20.84	0.374	47.3
Wh2	11.0	20.84	0.374	63.5
Wh3	11.0	20.84	0.374	77.6
Wh4	15.9	20.84	0.164	107.2

Table 4.1: Layout of the pixel detector. Note that there are two of each wheel, since the detector is symmetric about z equal to 0.

and an endcap section, where I model the barrel as a series of three concentric cylinders and the endcap as a series of four wheels separated in z. The barrel begins at an innermost radius of 4.2 cm and extends outward to a radius of 14.3 cm. The endcap wheels extend outward along z to ± 107.364 cm. Table 4.1 gives an exact description of the pixel detector geometry and layout.

As I outline in table 4.2, the material composition of the active components of the model detector – the pixels and chips – is silicon. I fill the support structure with beryllium and use a mixture of aluminum, beryllium, carbon and water, as a coolant, to model the barrel and endcap services. The exact $\%X_o$ contributions of each material type for each detector component are in table 4.3. These $\%X_o$ contributions define the smeared material mixtures, as equation 4.6 describes.

#	Material	Composition	A	Z	ρ (g cm^{-3})	X_o (cm)
1	EC services	Al+Be+C+H_2O	24.575	11.133	1.03	28.1
2	B services	Al+Be+C+H_2O	24.575	11.133	1.80	16.1
3	Support	Be	9.01	4.0	1.848	35.3
4	Chips	Si	28.09	14.0	2.33	9.36
5	Pixels	Si	28.09	14.0	2.33	9.36

Table 4.2: Material composition of the pixel detector. B refers to barrel and EC refers to endcap.

Barrel/Wheel #	Material #	% X_o
B	2	0.74
B	3	0.18
B	4	0.19
B	5	0.28
Wh1,2,3	1	0.86
Wh4	1	0.46
Wh1,2,3,4	4	0.23
Wh1,2,3,4	5	0.27

Table 4.3: Radiation length contributions of the pixel detector.

4.1.2 The semiconductor tracker

The SCT lies directly on the outside of the pixel detector inside the inner detector logical volume. Like the pixel detector, I model the SCT as a series of four concentric barrel cylinders and nine parallel endcap wheels. One can see a pictorial representation of the SCT in figure 4.2. The barrel extends inward to a radius of 29.25 cm and outward to a radius of 52.75 cm. The endcap wheels reach out to ±278.5 cm in z. Table 4.4 contains the precise geometry and layout of the SCT.

There are four types of endcap wheel, each built from a different combination of four rings. The rings are intended, in the design of ATLAS, to each cover a different radial range. Thus, each endcap wheel has an inner radius equal to the inner radius of the smallest ring comprising it and an outer radius equal to the outer radius of the largest ring comprising it. The total thickness of each wheel is equivalent to the sum of the thickness of each ring type from which it is made. Rings 1, 2 and 4 build wheel type 1 (wheels 1,3–6), rings 1

Figure 4.2: The SCT.

Barrel/Wheel #	Inner radius (cm)	Outer radius (cm)	Half-length (cm)	z-position (cm)
B1	29.25	30.75	74.7	0.0
B2	36.55	38.05	74.7	0.0
B3	43.95	45.45	74.7	0.0
B4	51.25	52.75	74.7	0.0
Wh1	26.0	56.5	1.0	83.5
Wh2	32.0	56.5	0.85	92.5
Wh3	26.0	56.5	1.0	107.2
Wh4	26.0	56.5	1.0	126.0
Wh5	26.0	56.5	1.0	146.0
Wh6	26.0	56.5	1.0	169.5
Wh7	32.0	56.5	0.85	213.5
Wh8	38.0	56.5	0.85	252.8
Wh9	41.0	56.5	0.70	277.8

Table 4.4: Layout of the SCT. Note that there are two of each wheel, since the detector is symmetric about z equal to 0.

Ring #	Composition	R_{min} (cm)	R_{max} (cm)
1	Si	43.8	56.0
2	Si	33.4	45.1
3	Si	39.9	45.1
4	GaAs	26.0	33.1

Table 4.5: The SCT ring structure and composition. R refers to the radius (minimum and maximum, respectively) of the ring.

and 2 build wheel type 2 (wheels 2,7), rings 1 and 3 build wheel type 3 (wheel 8) and ring 1 builds wheel type 4 (wheel 9). The active detection media also differ between ring types. Silicon is the active medium in rings 1–3, while, for ring 4, gallium arsenide does the job. One can find a summary of the ring information in table 4.5.

Even though the SCT design consists of these ring modules, the SCT endcap model, for simplicity, does not. Rather, the endcap model consists of simple cylindrical wheels, as I described above, where the material of each ring type is smeared, again according to equation 4.6, to yield the average material definition for each wheel. As well, the cooling and support systems, spine, hybrid module and mounting and cabling contribute to this average material definition. As one can read in table 4.6, I model the cooling system as a combination of aluminum and water and the support system as carbon. The spine is beryllium oxide. In the endcap, I build the hybrid module out of silicon and in the barrel I use copper. Finally, aluminum is the material of choice for the mounting and cabling. Table 4.7 lists the $\%X_o$ contribution of each material to each barrel section and endcap wheel.

4.1.3 The transition radiation tracker

Enveloping both the pixel detector and the SCT, the TRT is the outermost, and final, subdetector comprising the inner detector. The TRT model, a picture of which one can see in figure 4.3, consists of a barrel of half-length 79.0 cm and a much longer endcap section that extends out to ±339.6 cm in z. The endcap is split into two sections of differing radii at z equal to ±280.5

#	Material	Composition	A	Z	ρ (g cm^{-3})	X_o (cm)
1	Cooling	Al+H_2O	20.582	10.066	1.52	18.8
2	Support	C	12.0	6.0	0.13	328.0
3	Spine	BeO	15.0	6.667	3.01	14.7
4	EC hybrid	Si	28.09	14.0	4.66	4.68
5	B hybrid	Cu	63.54	29.0	8.96	1.43
6	Mounting+Cabling	Al	26.98	13.0	2.7	8.90
7	Detector	Si	28.09	14.0	2.33	9.36
8	Detector	GaAs	72.393	32.036	5.307	2.30

Table 4.6: Material composition of the SCT. B refers to barrel and EC refers to endcap.

Barrel/Wheel #	Material #	% X_o
B	2	0.47
B	5	0.99
B	7	0.70
1	1	0.07
1	2	0.30
1	3	0.19
1	4	0.43
1	6	0.42
1	7	0.39
1	8	0.52
2	1	0.07
2	2	0.30
2	3	0.17
2	4	0.36
2	6	0.33
2	7	0.68
3	1	0.07
3	2	0.30
3	3	0.17
3	4	0.45
3	6	0.36
3	7	0.66
4	1	0.04
4	2	0.30
4	3	0.14
4	4	0.26
4	6	0.28
4	7	0.56

Table 4.7: Radiation length contributions of the SCT.

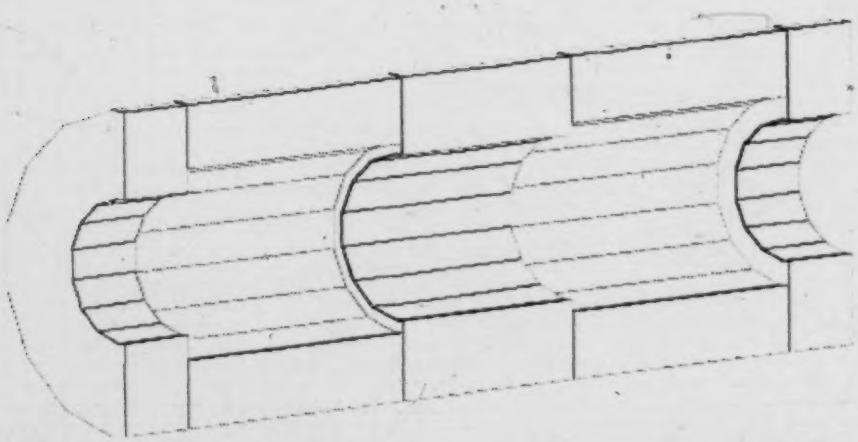

Figure 4.3: The TRT consists of a barrel and an endcap. The endcap is split into two because the two sections differ in radius and a slightly different set of materials services each part.

Barrel/Endcap	Inner radius (cm)	Outer radius (cm)	Half-length (cm)	z-position (cm)
B	56.0	108.0	79.0	0.0
IEC	64.0	108.0	100.75	179.75
OEC	48.0	108.0	29.55	310.05

Table 4.8: Layout of the TRT. Note that there are two of each endcap, since the detector is symmetric about z equal to 0.

cm and is a result of a change in the physical attributes of the endcaps at this position. Table 4.8 outlines the full geometry and layout of the TRT model.

Gas-filled straws constitute a large proportion of the volume of the TRT. I take the gas to be a mixture of 70% xenon, 20% tetrafluoromethane and 10% carbon dioxide and the straw shell material to be kapton of density 1.39 g cm^{-3}. Copper comprises the anode wire that is inside each straw. The radiator in the barrel and endcaps I model as foam and foil, respectively. All of the support frames in both the barrel and endcap regions are carbon. Finally, as before, I use a combination of aluminum and water to model the TRT cooling services. Of course, table 4.9 outlines all of this in detail and table 4.10 lists the $\%X_o$ contributions for the barrel and endcaps of all of the materials.

#	Material	Composition	A	Z	ρ (g cm^{-3})	X_o (cm)
1	Straws	$C_5H_4O_2$	12.88	6.456	1.39	28.6
2	Gas	Xe+CF_4+CO_2	109.293	45.184	0.005	2090.0
3	Wires	Cu	63.54	29.0	8.96	1.43
4	B radiator	Foam, C+H	10.438	5.286	0.059	748.0
5	IEC radiator	Foil, C+H	10.438	5.286	0.059	748.0
6	OEC radiator	Foil, C+H	10.438	5.286	0.030	1470.0
7	IB support	C	12.01	6.0	2.661	16.0
8	OB support	C	12.01	6.0	2.484	17.1
9	IECI support	C	12.01	6.0	3.960	10.8
10	IECO support	C	12.01	6.0	0.872	48.8
11	OECI support	C	12.01	6.0	2.747	15.5
12	OECO support	C	12.01	6.0	0.760	56.1
13	Cooling	Al+H_2O	22.603	11.001	1.680	16.1

Table 4.9: Material composition of the TRT. B refers to barrel, EC refers to endcap, I refers to inner and O refers to outer; thus, there is the inner barrel, the outer barrel, the inner endcap, the outer endcap and the inner and outer endcap inner and outer support!.

Barrel/Endcap #	Material #	$\%X_o$
B	1	4.2
B	2	0.63
B	3	0.2
B	4	4.4
B	7	4.4
B	8	6.0
B	13	1.4
IEC	1	4.1
IEC	2	0.63
IEC	3	0.13
IEC	5	6.7
IEC	9	2.7
IEC	10	8.0
IEC	13	5.1
OEC	1	3.7
OEC	2	0.65
OEC	3	0.15
OEC	6	5.6
OEC	11	4.6
OEC	12	15.4

Table 4.10: Radiation length contributions of the TRT.

4.2 The calorimetry

There are two sections of calorimetry: the electromagnetic calorimetry and the hadronic calorimetry. The electromagnetic calorimeter logical volume model is a cylinder with an inner radius of 3.7 cm, an outer radius of 225.0 cm and a half-length of 426.2 cm. It contains the inner detector logical volume, as well as the electromagnetic calorimeter barrel and endcap models. Like the inner detector, I fill this logical volume with air.

The larger hadronic calorimeter logical volume, in turn, contains the ECAL logical volume and, once again, air is the material that fills it. Along with the ECAL logical volume, the HCAL logical volume also contains both a barrel and endcap tile calorimeter and liquid argon endcap and forward calorimeters. It contains these within a cylinder of inner radius 3.7 cm, outer radius 423.0 cm and half-length 612.0 cm.

Finally, for organisational purposes, a calorimeter logical volume exists to contain the HCAL logical volume (and, in turn, the ECAL logical volume). This model is again cylindrical with an inner radius of 3.7 cm, an outer radius of 425.0 cm and a half-length of 665.0 cm. Also, air is, of course, its material constituent. A more concise description of these subdetectors follows in the subsections below.

4.2.1 The electromagnetic calorimeter

As one can see in figure 4.4, the ECAL model consists of both a barrel and an endcap, where the endcap is split into two sections because of a change in the radiation length between them. The cylindrical barrel has an inner radius of 150.0 cm, an outer radius of 205.0 cm and a half-length of 300.0 cm. The two endcap sections share the same dimensions: an inner radius of 15.0 cm, an outer radius of 207.7 cm and a half-length of 15.8 cm. The inner and outer endcaps are offset from z equal to 0 by a distance of $\pm$379.9 cm and $\pm$411.5 cm, respectively. One can find this description of the layout and dimensions of the ECAL in table 4.11.

The material description of the ECAL model, which one can find in table

Figure 4.4: The ECAL consists of a barrel and an endcap. I model the endcap in two sections because of a change in the radiation length between them.

Barrel/Endcap	Inner radius (cm)	Outer radius (cm)	Half-length (cm)	z-position (cm)
B	150.0	205.0	300.0	0.0
IEC	15.0	207.7	15.8	379.9
OEC	15.0	207.7	15.8	379.9

Table 4.11: Layout of the ECAL. Note that there are two of each endcap, since the detector is symmetric about z equal to 0.

#	Material	Composition	A	Z	ρ (g cm^{-3})	X_o (cm)
1	Absorber	Pb	207.19	82.0	11.35	0.56
2	Active detector	LAr	39.95	18.0	1.40	14.0
3	Electrodes	Kapton+Cu	55.002	25.2	5.175	2.72
4	Steel	Fe+Cr+Ni+C	55.29	25.74	7.80	1.79
5	Glue	Polystyrene	11.154	5.615	1.032	42.0

Table 4.12: Material composition of the ECAL.

Material	Thickness (mm)		
	Barrel	Inner Endcap	Outer Endcap
Absorber	1.3	1.7	2.2
Active detector	2.1 (×2)	1.85 (×2)	2.45 (×2)
Electrodes	0.32	0.32	0.32
Steel	0.4	0.4	0.4
Glue	0.23	0.33	0.33

Table 4.13: The thickness for the materials comprising a single layer of the ECAL. Each layer actually consists of two layers of liquid argon, the active detection medium.

4.12, consists, essentially, of two parts – the absorber material and the active detection medium – that are, in ATLAS, successively layered one after the other. To model the absorber, I use solid lead. Along with the lead, I also include glue, which I model as polystyrene (simply for a lack of a better material description for glue), and stainless steel in the absorber material since, in ATLAS, the lead absorber plates have a glue-attached stainless steel covering. The stainless steel is a mixture of 77.9% iron, 17.0% chromium, 5.0% nickel and 0.1% copper, by mass. I use liquid argon to model the active detection medium. Finally, I model the electrodes as a kapton and copper mixture with a ratio of kapton to copper of one to one, by volume. Table 4.13 outlines the amount of each material type comprising the ECAL by the thickness of each in a single layer and table 4.14 contains the familiar $\%X_o$ smearing contributions of each material.

4.2.2 The hadronic tile calorimeter

The model of the tile HCAL, as figure 4.5 shows, consists of a cylindrical barrel of an inner radius of 228.0 cm, an outer radius of 423.0 cm and a half-length of 282.0 cm and a cylindrical endcap with inner an outer radii identical to those of the barrel and a half-length of 145.5 cm. The endcap is offset from z equal to 0 by 457.5 cm. Table 4.15 reiterates these details.

I give the tile HCAL a very simple material description, consisting of only two materials: iron to model the 14 mm thick absorber plates and plastic scintillator to model the 3 mm thick active detector layers. Table 4.16 contains

Barrel/Endcap #	Material #	%V
B	1	20.16
B	2	65.12
B	3	4.96
B	4	6.20
B	5	3.56
IEC	1	26.36
IEC	2	57.36
IEC	3	4.96
IEC	4	6.20
IEC	5	5.12
OEC	1	26.99
OEC	2	60.12
OEC	3	3.93
OEC	4	4.91
OEC	5	4.05

Table 4.14: Volume contributions of the ECAL.

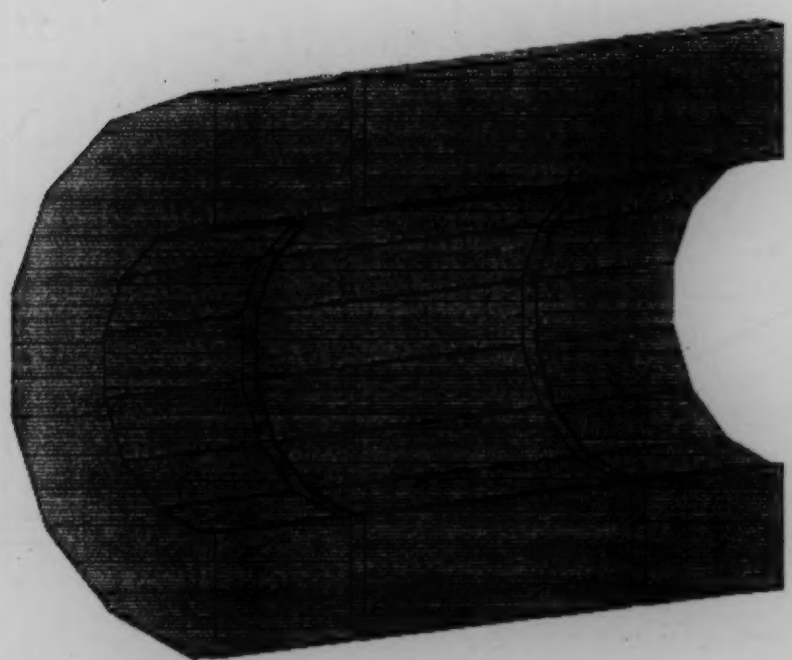

Figure 4.5: The tile HCAL consists of a barrel and an endcap. The material composition of both the barrel and the endcap is identical.

Barrel/Endcap	Inner radius (cm)	Outer radius (cm)	Half-length (cm)	z-position (cm)
B	228.0	423.0	282.0	0.0
EC	228.0	423.0	145.5	457.5

Table 4.15: Layout of the tile HCAL. Note that there are two of each endcap, since the detector is symmetric about z equal to 0.

#	Material	Composition	A	Z	ρ (g cm^{-3})	X_o (cm)
1	Absorber	Fe	55.85	26.0	7.87	1.76
2	Active detector	Plastic scintillator	6.25	3.4	1.032	43.0

Table 4.16: Material composition of the tile HCAL.

the exact material description and table 4.17 shows the $\%V$ contributions for each material type.

4.2.3 The liquid argon endcap calorimeter

The model LAr endcap calorimeter, as the name suggests, consists only of endcaps offset from z equal to 0 by 519.1 cm. The cylindrical model has an inner radius of 45.7 cm, an outer radius of 209.0 cm and a half-length of 92.9 cm. For convenience, table 4.18 also contains these dimensions. One can find a picture of the LAr endcap model in figure 4.6.

Once again, I define only a very basic material model for the LAr endcap calorimeter. I use copper to model the absorber plates and liquid argon as the active detector medium. Table 4.19 contains the details and 4.20 lists the $\%V$ contributions of each material.

Barrel/Endcap #	Material #	$\%V$
B	1	82.35
B	2	17.65
EC	1	82.35
EC	2	17.65

Table 4.17: Volume contributions of the tile HCAL.

Figure 4.6: The LAr HCAL resides in the endcap region of ATLAS where the high radiation level requires a cyclable active detector medium.

Barrel/Endcap	Inner radius (cm)	Outer radius (cm)	Half-length (cm)	z-position (cm)
EC	45.7	209.0	92.9	519.1

Table 4.18: Layout of the LAr HCAL. Note that there are two of each endcap, since the detector is symmetric about z equal to 0.

#	Material	Composition	A	Z	ρ (g cm^{-3})	X_o (cm)
1	Absorber	Cu	63.54	29.0	8.96	1.43
2	Active detector	LAr	39.95	18.0	1.40	14.0

Table 4.19: Material composition of the LAr HCAL.

Barrel/Endcap #	Material #	$\%V$
EC	1	81.52
EC	2	18.48

Table 4.20: Volume contributions of the LAr HCAL.

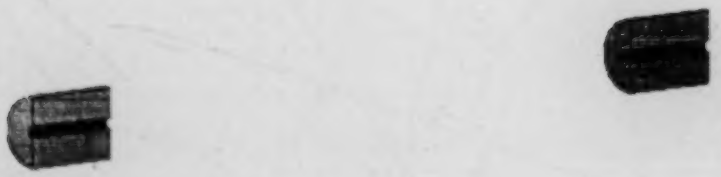

Figure 4.7: The FCAL resides in the endcap region of ATLAS where the high radiation level requires a cyclable active detector medium. These high z-momentum of the radiation travelling in the very forward regions of ATLAS also require the FCAL to be very dense; thus, the bulk of the material in this model forms the (mainly) tungsten absorber plates.

4.2.4 The forward calorimeter

The FCAL model, which figure 4.7 shows, lies in the extreme forward region of ATLAS very close to the beam pipe, with an inner radius of only 7.2 cm and an outer radius of 45.7 cm. It has a half-length of 69.23 cm and its centre lies offset from z equal to 0 at ±537.0 cm. Table 4.21 outlines the simple geometry and layout of the model.

Like the actual FCAL, I make the FCAL model very dense, consisting mainly of absorber plates of copper, tungsten, iron, and nickel. One can find this exact composition in table 4.22. The active detector medium, which I model as liquid argon, contributes relatively minimally to the overall volume of the FCAL model, as table 4.23 shows.

Barrel/Endcap	Inner radius (cm)	Outer radius (cm)	Half-length (cm)	z-position (cm)
EC	7.2	45.7	69.23	537.0

Table 4.21: Layout of the FCAL. Note that there are two of each endcap, since the detector is symmetric about z equal to 0.

#	Material	Composition	A	Z	ρ (g cm^{-3})	X_o (cm)
1	Absorber	Cu	63.54	29.0	8.96	1.43
2	Absorber	W	183.84	74.0	19.3	0.35
3	Absorber	Fe	55.85	26.0	7.87	1.76
4	Absorber	Ni	58.69	28.0	8.902	1.42
5	Active detector	LAr	39.95	18.0	1.40	14.0

Table 4.22: Material composition of the FCAL.

Barrel/Endcap #	Material #	$\%V$
EC	1	39.17
EC	2	46.41
EC	3	1.19
EC	4	2.03
EC	5	11.20

Table 4.23: Volume contributions of the FCAL.

4.3 The muon system

The muon system logical volume – a cylinder with an inner radius of 3.7 cm, an outer radius of 1204.0 cm and a half-length of 2266.0 cm – is the largest volume in the ATLAS model, encompassing the HCAL logical volume, as well as the beam pipe, shielding and toroid magnet systems. It contains the four muon subsystems, all of which I model independently and describe in the subsections below. Details concerning the beam pipe, shielding and magnet systems comprise subsequent sections. Aga[redacted]ill this logical volume with air.

4.3.1 The monitored drift tube chambers

The MDT model consists of three cylindrical barrel layers that extend outward along z to ±1225.0 cm with an innermost radius of 431.7 cm and an outermost radius of 1078.6 cm and five endcap wheels reaching to ±2265.55 cm in z, each with varying inner and outer radii, as table 4.24 outlines. Figure 4.8 shows a picture of this subsystem. I reduce the outer radius of the innermost endcap wheel to 500.5 cm from 618.7 cm, as [52] suggests it should be, simply to avoid an overlap of this wheel with the barrel toroid magnet volume. I

Figure 4.8: Both the barrel and endcap MDT chambers.

should also note that the central MDT chamber actually lies within the air-core of the barrel toroid magnet.

The drift tubes themselves consume most of the volume in the MDT chambers. I model each tube as consisting of a 400 μm thick aluminum shell of density 2.73 g cm^{-3}. Inside the tube is a gas with a composition of 91% argon, 4% nitrogen and 5% methane, by volume. The gas has a density of 0.00512 g cm^{-3} and comprises a total volume of approximately 800 m^3. I use a 97% to 3% mixture, by mass, of tungsten to rhenium to model the wire anode at the centre of each tube. The spacers separating the parallel tube layers are solid aluminum and air fills the gaps in between those layers. Table 4.25 lists all of the material details of the MDT chamber model and table 4.26 stores the $\%V$ contributions of each of these materials to the overall smeared material that fills the MDT volumes.

Barrel/Endcap #	Inner radius (cm)	Outer radius (cm)	Half-length (cm)	z-position (cm)
B1	431.7	473.3	655.1	0.0
B2	686.1	737.2	913.0	0.0
B3	1027.5	1078.6	1225.0	0.0
EC1	212.1	500.5	18.35	759.2
EC2	540.0	805.5	15.75	997.0
EC3	173.5	1119.0	18.2	1384.2
EC4	652.0	1159.0	18.2	2083.2
EC5	298.5	733.5	15.75	2249.8

Table 4.24: Layout of the MDTs.

#	Material	Composition	A	Z	ρ (g cm^{-3})	X_o (cm)
1	Tubes	Al	26.98	13.0	2.73	8.8
2	Gas	Ar+N_2+CH_4	38.63	17.44	0.00512	3910.0
3	Wires	W+Re	183.91	74.03	19.3	0.351
4	Spacers	Al	26.98	13.0	2.70	8.9
5	Interior	Air	14.61	7.3	0.001	30400.0

Table 4.25: Material composition of the MDTs.

Barrel/Endcap #	Material #	$\%V$
B/EC	1	2.58
B/EC	2	46.51
B/EC	3	0.01
B/EC	4	5.09
B/EC	5	45.81

Table 4.26: Volume contributions of the MDTs.

Figure 4.9: The CSCs lie only in the endcap region.

4.3.2 The cathode strip chambers

I model the CSCs as a simple cylinder in the endcap region at z equal to ± 732.05 cm, a picture of which one can see in figure 4.9. In ATLAS, the CSCs are tilted at 11.59° to allow for better coverage in the forward region; nevertheless, for simplicity, I do not tilt the CSCs in this model. As one can find in table 4.27, the CSCs have a half-length of 45.15 cm, an inner radius of 85.9 cm and an outer radius of 208.1 cm.

The ATLAS design calls for rohacell, a lightweight foam, to build the frame that holds the CSCs. I replace the rohacell with polystyrene in the CSC model. I also change the material definition of the FR4 laminate step to acrylic. Both of these choices are a direct result of the information available on rohacell and FR4 laminate. Inside the frame is a honeycomb layer of Nomex, an aromatic nylon compound, that I model as nylon. There is also a 90 mm gap of air between each of the four rohacell/Nomex layers of the CSCs.

The active detection medium of the CSCs is a gas consisting of 30% argon, 50% carbon dioxide and 20% tetrafluoromethane comprising a total volume of approximately 1.1 m^3. It fills the Nomex honeycomb. The anode and cathode that one uses for signal readout I model as tungsten and copper, respectively.

Barrel/Endcap	Inner radius (cm)	Outer radius (cm)	Half-length (cm)	z-position (cm)
EC	85.9	208.1	45.15	732.05

Table 4.27: Layout of the CSCs.

#	Material	Composition	A	Z	ρ (g cm^{-3})	X_o (cm)
1	Gas	Ar+CO_2+CF_4	21.80	10.29	0.0022	13459.0
2	Cathode	Cu	63.54	29.0	8.96	1.43
3	Anode	W	183.84	74.0	19.3	0.35
4	Frame	Polystyrene	11.154	5.615	1.032	42.0
5	Step	Acrylic	12.40	6.24	1.19	34.07
6	Nomex	Nylon	12.77	6.41	1.18	35.52
7	Gaps	Air	14.61	7.3	0.001	30400.0

Table 4.28: Material composition of the CSCs.

Barrel/Endcap #	Material #	$\%V$
EC	1	10.80
EC	2	0.28
EC	3	0.52
EC	4	33.24
EC	5	6.28
EC	6	18.98
EC	7	29.90

Table 4.29: Volume contributions of the CSCs.

Table 4.28 contains a more precise definition of each of these materials. One can also find the $\%V$ contribution of each of these materials to the final smeared material definition of the CSCs in table 4.29.

4.3.3 The resistive plate chambers

The RPC models lie in the barrel region of the muon system. As figure 4.10 shows, there are three layers in total, where the inner and middle layers sandwich the central MDT barrel layer inside the air-core of the barrel toroid magnet. Consequently, they have a half-length equivalent to the central barrel MDT chamber of 913.0 cm. The thickness of the inner RPC cylinder is 13.2 cm and the thickness of the middle cylinder is 13.1 cm, where each layer lies flush to the MDT chamber. The outer RPC cylinder, lying flush on the inside of the outer MDT chamber layer, again with the same half-length of that MDT chamber of 1225.0 cm, has a thickness of 11.7 cm. Table 4.30 gives the exact layout and dimensions of the RPC layers.

I use bakelite to model the resistive layers of the RPC chambers. It has

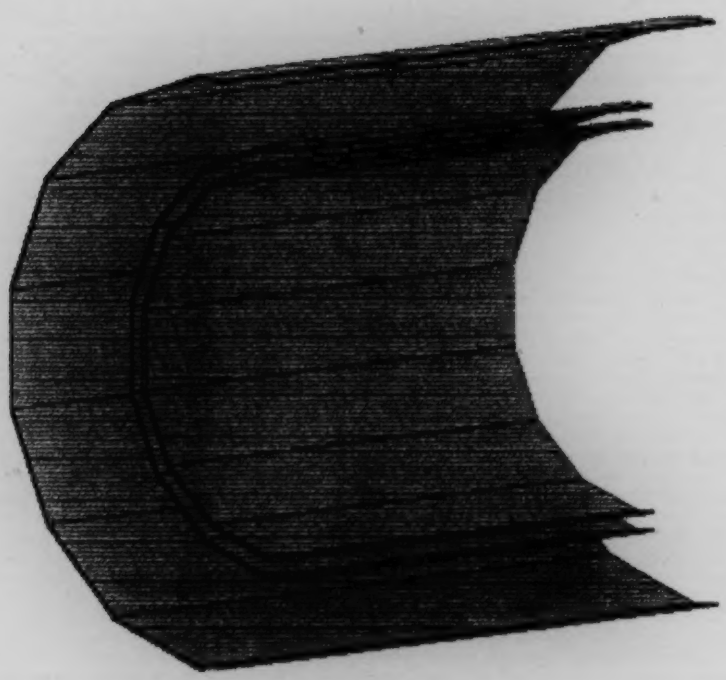

Figure 4.10: The RPCs, which one uses for triggering, lie only in the barrel region.

Barrel/Endcap #	Inner radius (cm)	Outer radius (cm)	Half-length (cm)	z-position (cm)
B1	672.9	686.1	913.0	0.0
B2	737.2	750.3	913.0	0.0
B3	1015.8	1027.5	1225.0	0.0

Table 4.30: Layout of the RPCs.

#	Material	Composition	A	Z	ρ (g cm^{-3})	X_o (cm)
1	Bakelite	H+C+O	12.05	6.05	1.25	33.63
2	Gas	$C_2H_2F_4$+iso-C_4H_{10}	16.88	8.08	0.00420	8422.1
3	Panels	Polystyrene	11.154	5.615	0.040	1083.6
4	Strips	Al	26.98	13.0	2.70	8.9
5	Strips	Polyethelene	10.429	5.286	0.93	47.4
6	Spacers	Polycarbonate	11.89	5.97	1.20	34.59

Table 4.31: Material composition of the RPCs.

Barrel/Endcap #	Material #	$\%V$
B	1	9.88
B	2	4.50
B	3	80.25
B	4	2.71
B	5	0.99
B	6	1.67

Table 4.32: Volume contributions of the RPCs.

a chemical composition of 5.7441% hydrogen, 77.4591% carbon and 16.7968% oxygen, by mass, with a density of 1.25 g cm^{-3} [72]. I model the active gas as tetrafluoroethane-isobutane in a 97% to 3% ratio, by volume, comprising a total volume of nearly 18 m^3. The RPC η and ϕ readout strips are aluminum with a polyethylene backing, although the actual detector design calls for the backing to be polyethylene-teraphtalate. I model the spacer and frame material as polycarbonate and the panels between the internal RPC layers as polystyrene. One can find a more complete description of these materials in table 4.31. The $\%V$ contributions of each material are in table 4.32.

4.3.4 The thin gap chambers

The model of the TGCs consists of five wheels in the endcap region of ATLAS lying directly fore and aft of the central MDT chamber endcap. The TGC triplet layer lies closest to the interaction point at z equal to $\pm$1307.5 cm and has a half-width of 16.5 cm. The other four wheels are staggered on the other side of the MDT chamber wheel at a value of z between $\pm$1407.0 cm and $\pm$1504.0 cm. Each of these wheels has a half-width of 11.5 cm, modelling

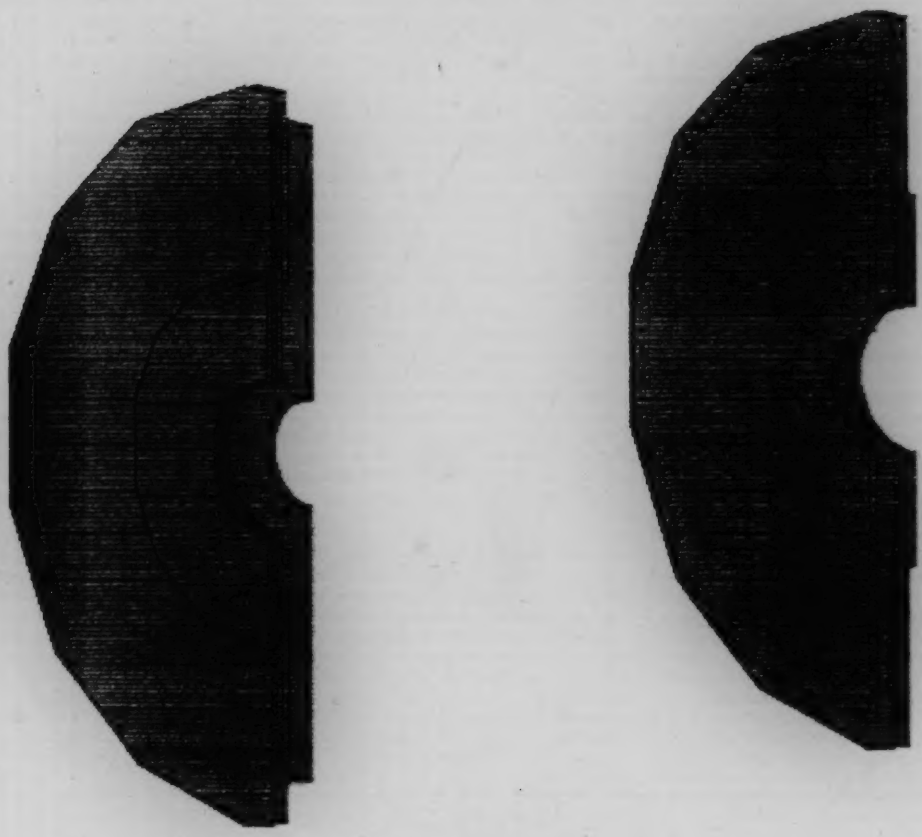

Figure 4.11: The TGCs lie only in the endcap region.

the TGC doublet layers. The TGCs extend inward to an innermost radius of 170.7 cm and outward to an outermost radius of 1203.5 cm. A list of the exact layout and dimensions of each layer is in table 4.33 with figure 4.11 showing the corresponding picture.

To model the gas in the TGC wheels, I use carbon dioxide–*n*-pentane in a 55% to 45% ratio, by volume. The gas comprises approximately 16 m^3 in total volume. The material I use to model the 50 μm thick wire anode used for readout is tungsten. Dividing the gas volumes are layers of G10, a compressed epoxy-resin soaked fibrous glass substance [73]. It has a material composition of 0.71% hydrogen, 53.0% oxygen, 27.0% silicon and 19.1% calcium and a density of 1.85 g cm^{-3}. The two gas volumes in the doublets and three gas

Barrel/Endcap #	Inner radius (cm)	Outer radius (cm)	Half-length (cm)	z-position (cm)
EC1	170.7	1081.2	16.5	1307.5
EC2	569.1	1203.5	11.5	1418.5
EC3	244.0	587.7	11.5	1445.5
EC4	594.1	1203.5	11.5	1465.5
EC5	244.0	607.8	11.5	1492.5

Table 4.33: Layout of the TGCs.

#	Material	Composition	A	Z	ρ (g cm^{-3})	X_o (cm)
1	Honeycomb	Polystyrene	11.154	5.615	1.032	42.0
2	Gas	CO_2+n-C_5H_{12}	11.96	6.03	0.345	121.6
3	Wires	W	183.84	74.0	19.3	0.35
4	G10	H+O+Si+Ca	23.73	11.85	1.85	13.49

Table 4.34: Material composition of the TGCs.

volumes in the triplet TGC have a separator of dense paper, for which I use polystyrene of density 1.032 g cm^{-3} in place of the paper as a model. Table 4.34 outlines the exact composition of each of these materials. Even though the doublet and triplet layers contain a slightly different weighting of each of these materials, I define a single average TGC material, the $\%V$ contributions for which table 4.35 shows.

4.4 The magnet system

The ATLAS magnet system model, which figure 4.12 shows, consists of a thin solenoid in the inner barrel region and a large air-core toroid in the outer barrel region along with endcap air-core toroids that supplement the toroidal field in the ATLAS forward region. As table 4.36 lists, the conductor consists

Barrel/Endcap #	Material #	$\%V$
EC	1	71.33
EC	2	12.65
EC	3	0.27
EC	4	15.75

Table 4.35: Volume contributions of the TGCs.

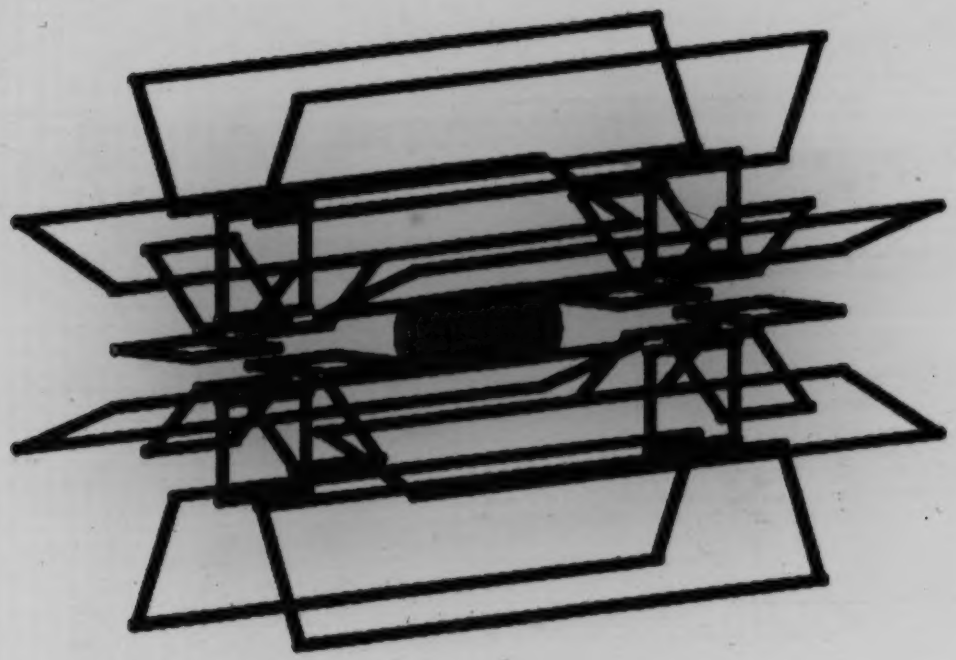

Figure 4.12: The magnet system consists of a barrel solenoid, a barrel toroid and an endcap toroid. The barrel solenoid envelops the whole inner detector and the outer layers of the muon system lie within the barrel toroid core. There is nothing except air inside the endcap toroid core.

of a mixture of aluminum, copper, niobium and titanium, which is resident in different proportions for each of the three magnet types. The coolant, which lowers the temperature of the magnets to a level where they become superconducting, is liquid helium and the cold-mass support is aluminum. To increase the mass of the magnets to those which [53] gives, I add iron into the magnet mixture.

As one can read in the subsections below, I only model the cold-mass volumes of the magnets; thus, the density of each of the magnets is increased so that the mass of the magnets conforms to that given by [53]. I use iron simply to increase the magnet mass. The layout of the magnets and their $\%M$ contributions follow in the corresponding subsections.

#	Material	Composition	A	Z	ρ (g cm^{-3})	X_o (cm)
1	Coolant	LHe	4.0	2.0	0.125	755.18
2	Support	Al	26.98	13.0	2.70	8.9
3	Conductor	Al	26.98	13.0	2.70	8.9
4	Conductor	Cu	63.54	29.0	8.96	1.43
5	Conductor	Nb	92.91	41.0	8.57	1.16
6	Conductor	Ti	47.87	22.0	4.54	3.56
7	Additional mass	Fe	55.85	26.0	7.87	1.76

Table 4.36: Material composition of the magnet system.

Barrel/Endcap #	Material #	$\%M$
B	1	7.37
B	2	25.97
B	3	45.26
B	4	6.14
B	5	10.17
B	6	5.09

Table 4.37: Mass contributions of the barrel solenoid. The density of the barrel solenoid is taken to be 1.58 g cm^{-3}, which is its total mass divided by the total volume of the barrel solenoid that I define in the simulation.

4.4.1 The barrel solenoid

The barrel solenoid model lies sandwiched between the inner detector and ECAL volumes, having an inner radius of 123.0 cm, an outer radius of 131.5 cm and a half-length of 265.0 cm. Table 4.37 gives the $\%M$ contributions of each of the solenoid components that table 4.36 lists. For these, I assume that the density of the barrel solenoid is 1.58 g cm^{-3}, which I base on the total mass of this magnet, including the conductor, cold mass and supports, that [53] gives as 5.7 tonnes.

The magnetic field inside of the barrel solenoid is a uniform 2 T, extending to the outer edge of the barrel volume. Although the actual field is not completely uniform, I choose to model it as uniform purely out of simplicity. This field allows for bending of the charged particles that pass through the inner detector region in the model, where a majority of the inner detector lies inside of the solenoid volume.

4.4.2 The barrel and endcap toroids

The barrel toroid magnet lies in the outer barrel region of the ATLAS model. The inner radius of the toroid is 500.9 cm and the outer radius is 1015.9 cm and it has a half-length of 1247.4 cm. It is an air-core magnet, which enables it to contain the middle MDT barrel chamber and its surrounding RPC layers, where the radius of each winding itself is 38.4 cm. The inner and outer horizontal tubes are connected at each end by vertical tubes of the same radii, set at z equal to ±1228.2 cm, thus lying flush with the ends of the horizontal tubes. The barrel toroid consists of eight coils evenly spaced in the x-y plane that are offset from vertical by 22.5°.

The endcap toroids are similar to the barrel toroid, but they lie farther along the z-axis at ±1013.0 cm. The inner radius of the toroid is 121.0 cm and the outer radius is 500.9 cm. It has a half-length of 217.5 cm. There are eight coils in each of the two endcaps, each of which has a radius of 40.0 cm. Again, the horizontal tubes are connected at either end by a vertical tube of the same radius, set at z equal to ±815.5 cm for the inner tubes and ±1210.5 cm for the outer tubes. The endcaps are also air-core toroids, but they contain no other volumes. The eight coils are spaced evenly in the x-y plane and are offset from the barrel toroid by 22.5° (so they have no offset from vertical).

Table 4.38 lists the $\%M$ contributions of each of the magnet materials in table 4.36. I take the density of the barrel toroid to be 15.27 g cm^{-3}, corresponding to a total mass of 830 tonnes, and the density of the endcap toroids to be 16.17 g cm^{-3}, corresponding to a mass of 239 tonnes each.

I use an ideal toroidal field to model the field inside the barrel and endcap toroid models, where I have scaled the fields to more closely resemble the magnetic field map of ATLAS. The magnetic field of the toroids is given by

$$\vec{B} = \alpha \frac{\mu_o N I}{4\pi s} \hat{\phi}, \tag{4.11}$$

where μ_o is the permeability of free space, N is the number of coils and I is the current. The $\hat{\phi}$ denotes the direction of the magnetic field, where the coordinate system is right-handed, and the α is a scale factor that I use to bring this ideal field closer to the actual field values. Table 4.39 lists the

Barrel/Endcap	Material #	%M
B	1	1.57
B	2	55.42
B	3	11.07
B	4	1.09
B	5	1.36
B	6	0.70
B	7	28.79
EC	1	0.95
EC	2	55.44
EC	3	5.97
EC	4	0.96
EC	5	1.08
EC	6	0.56
EC	7	35.04

Table 4.38: Mass contributions of the barrel and endcap toroids. The density of the barrel toroid is taken to be 7.64 g cm^{-3} and the density of the endcap toroid is taken to be 8.09 g cm^{-3}, which are their total masses divided by their total respective volumes that I define in the simulation.

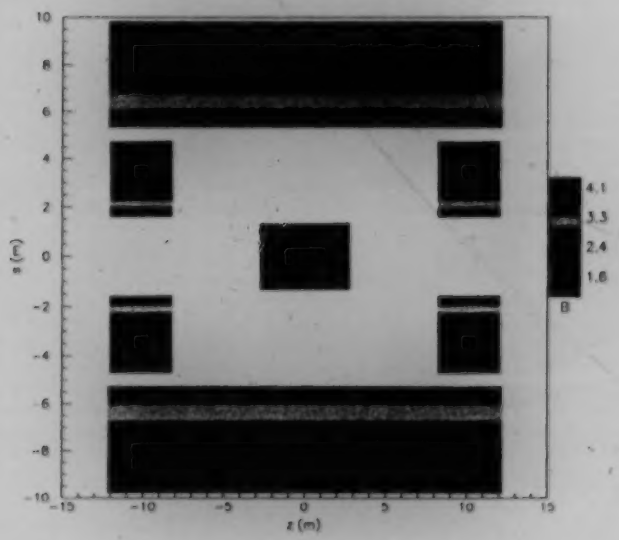

Figure 4.13: This is a slice in the s-z plane of the magnetic field map of the barrel solenoid and barrel and endcap toroid models. Note that the magnetic field is symmetric through rotations in ϕ, as per equation 4.11, so this image contains all necessary information.

Barrel/Endcap	N	I (kA)	α
B	960	20.5	10.5
EC	928	20.0	3.5

Table 4.39: The barrel and endcap toroid magnetic field parameters. I use the scale factor α to force the ideal toroidal field to match the actual magnetic field map more closely.

Figure 4.14: The beam pipe I model as beryllium. The forward shielding is solid iron and I build it as a cylinder of staggered outer radius. It has an inner radius of 3.7 cm, lying jut outside of the beam pipe.

constants for the barrel and endcap toroids. Figure 4.13 shows a slice of the magnitude of the model magnetic field in the s-z plane at an x-position of 0. As per equation 4.11, the magnetic field is symmetric through a rotation in ϕ.

4.5 The beam pipe and forward shielding

The ATLAS design calls for the ATLAS beam pipe to consist of beryllium; thus, I model it as such. The design also calls for the forward shielding to have a primary composition of cast iron. As such, I model the forward shielding as solid iron. Table 4.40 contains the dimensions of the shield. Figure 4.14 shows the layout of these components.

Outer radius (cm)	Lower z limit (cm)	Upper z limit (cm)
170.0	1291.0	1404.0
243.5	1404.0	2004.0
298.0	2004.0	2234.1

Table 4.40: Layout and dimensions of the forward shielding. The shield has a uniform inner radius of 3.7 cm.

4.6 The ATLAS overburden and underburden and cavern system

The model of the ATLAS overburden [74, 75], as one can see in figures 4.15 and 4.16, consists of eight layers of rock of differing uniform densities, extending up to 78.91 m above the interaction point. The underburden has two layers of rock of uniform density, extending downward 1000.0 m below the interaction point. Each of these rock layers extends out to $\pm$1000.0 m in x and z. Table 4.41 shows the y-position and thickness of each of the rock layers, as well as the density of the rock that forms them. A mixture of 52.9% oxygen, 33.7% silicon, 4.4% calcium, 3.4% aluminum, 1.6% sodium, 1.4% iron, 1.3% potassium and 1.0% hydrogen, by mass, gives an approximate composition of cement, which, with a varying density, then models the rock overburden and underburden.

The model of UX15, the ATLAS cavern, is a box with a half-width of 1500.0 cm in x, a half-width of 1435.0 cm in y and a half-width of 2650.0 cm in z. The cavern centre sits at an x-position of -170.0 cm, a y-position of 215.0 cm and a z-position of 0.0 cm. The cavern has a 700 cm thick curved roof section with an inner radius of 1300.0 cm that has its centre at a y-position of 350.0 cm. The end walls, which are perpendicular to the beam pipe, are also curved with an inner radius of 2650.0 cm and a thickness of 500.0 cm. They are 2790.0 cm tall and have their centre at a y-position of 255.0 cm. The material filling the cavern is air.

Perpendicular to UX15 lie the models for caverns US15 and USA15. The US15 model is a cylinder of radius 1000.0 cm and half-length 800.0 cm lying at an x-position of 2330.0 cm, a z-position of 0.0 cm and with its centre at a

Y_{centre} (cm)	Thickness (cm)	ρ (g cm^{-3})
7741.0	300.0	2.4
7431.0	320.0	2.3
7081.0	380.0	2.5
6741.0	300.0	2.35
6266.0	650.0	2.4
4776.0	2330.0	2.4
3126.0	970.0	2.5
700.0	3882.0	2.45
-8120.5	6879.5	2.5
-15000.0	85000.0	2.5

Table 4.41: There are a total of eight rock layers comprising the overburden and two rock layers forming the underburden of ATLAS. Each of these extends to ±1000.0 m in x and z. This table shows the y-position of the centre of each rock layer, as well as its thickness and the density of the rock in it.

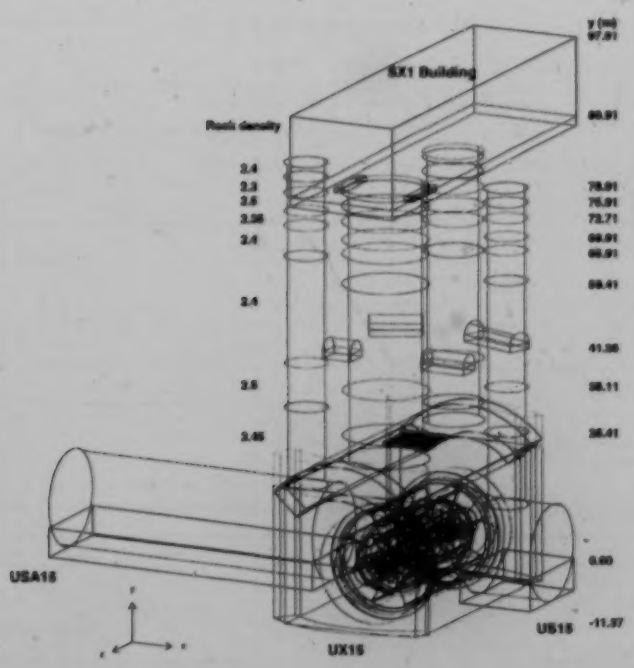

Figure 4.15: The ATLAS cavern system consists of the main cavern UX15 and two counting rooms USA15 and US15, as well as the four access shafts PX14, PX16, PM15 and PX15, along with their support galleries. The figure also shows the surface building SX1.

y-position of 220.0 cm. This cylinder forms the curved roof, where the cavern has a rectangular floor with a half-length of 800.0 cm in x, a half-length of 335.0 cm in y and a half-length of 1000.0 cm in z with its centre at a y-position of 35.0 cm. The USA15 cavern is also a cylinder with a rectangular floor. The cylindrical roof has a radius of 1000.0 cm and a half-length of 3025.0 cm. It lies at an x-position of -4895.0 cm, a y-position of 100.0 cm and a z-position of 0.0 cm. The floor has a half-length of 3025.0 cm in x, a half-length of 300.0 cm in y and a half-length of 3025.0 cm in z. It lies directly below the cylindrical roof with its centre at a y-position of 0.0 cm. Both caverns have floors that are concrete of density 2.45 g cm^{-3}, where the remaining room contains air.

The model of the ATLAS cavern system also accounts for the four cavern access shafts, PX15, PM15, PX14 and PX16. PX15 and PM15 are cylinders of radius 455.0 cm. The PX15 shaft reaches from the ground level at 7891.0 cm down to the roof of the USA15 cavern with its x-position centre at -2500.0 cm. Extending from the ground level down to the roof of the US15 cavern, the PM15 shaft has its x-position centre at 2100.0 cm. The z-position centre of both shafts is at 0.0 cm. The PX14 and PX16 shafts connect the roof of the ATLAS main cavern, UX15, to the ground level. Shaft PX14 has a radius of 900.0 cm and has its z-position centre at 1350.0 cm. Shaft PX16 is smaller, with a radius of 630.0 cm. It has its z-position centre at -1770.0 cm. Both shafts have their x-position centres lying at 0.0 cm.

In addition to the access shafts, there are four support galleries lying just off PX14 and PX16 in rock layer six. Built similarly to the US15 and USA15 caverns, the galleries, PX14A, PX14B, PX16A and PX16B consist of tube segment rooves with rectangular slab floors. Each cavern has a roof of radius 265.0 cm and a floor that reaches to the bottom edge of the cylinder with a half-length of 72.5 cm in y and a half-length of 265.0 cm in the circular plane of the cylinder forming the roof. Perpendicular to that plane, the half-length of PX14A is 316.0 cm, the half-length of PX14B is 488.5 cm, the half-length of PX16A is 554.0 cm and the half-length of PX16B is 691.0 cm. Each of the galleries lies at a y-position of 4271.0 cm. PX14A and PX14B have their z-position centres at 1085.0 cm and lie at $\pm$1129.0 cm in x, along either side

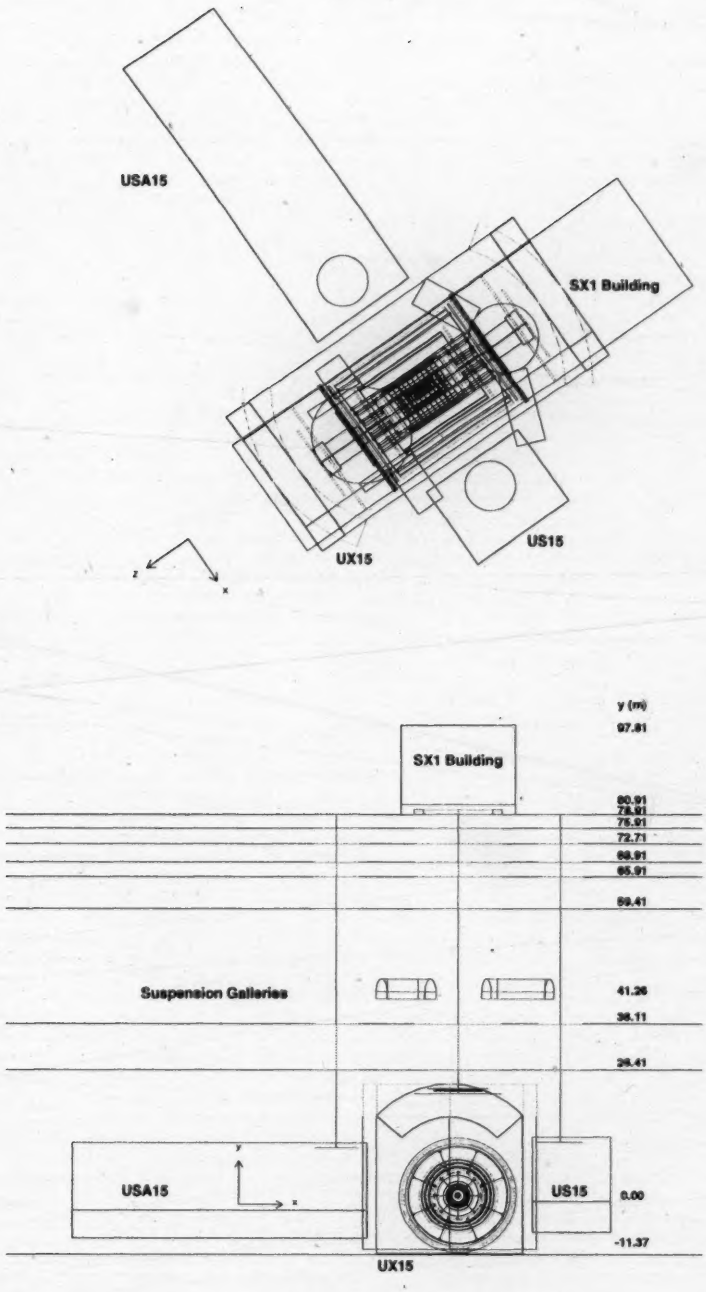

Figure 4.16: The top image shows a top-down view of the cavern system and the bottom image shows a side view of the cavern system, along the beamline.

of the PX14 shaft. PX16A has its x-position centre at -1064.9 cm and its z-position centre at -1260.2 cm and is at an angle of 295.583° with respect to the z-axis. With its x-position centre at 1232.5 cm and its z-position centre at -1301.9 cm, PX16B lies on the other side of the PX16 shaft. With respect to the z-axis, it is at an angle of 69.204°.

Although neither part of the rock overburden and underburden nor the cavern system, this model also includes the SX1 surface building, since it is important for cosmic ray background studies, acting as an active cosmic ray shield. This building model has a half-length of 1170.0 cm in x, a half-length of 945.0 cm in y and a half-length of 4230.0 cm in z and its y-position centre lies at 8836.0 cm above the interaction point. The walls and roof of this building are 3.0 mm thick iron sheets and the floor is 2.0 m thick concrete of density 2.4 g cm^{-3}. The rest of the volume – the dimensions above minus the thickness of the walls and floor – contains air. The floor above the PX14 and PX15 access shafts is only 1.0 m thick, since there are 1.0 m thick concrete shielding beams directly above the shafts and below the floor of SX1.

Chapter 5

Analysis I

This chapter describes the setup of the stau production, trapping and decay, as well as the detection of the stau decay products. As such, I call this the 'initial analysis', where the analysis methods that I present in chapter 6 depend on knowing how the detector model (see chapter 4) responds to the signal of the stau decay products.

One analysis 'run', as I will call it, begins with the production of stable staus via Monte Carlo proton-proton collisions. For this, I assume a mSUGRA model, with the parameters m_o equal to 0 GeV c^{-2}, A_o equal to 0 GeV c^{-2}, $\tan\beta$ equal to 10, sgnμ greater than 0 and $M_{1/2}$ between 300 GeV c^{-2} and 900 GeV c^{-2}, in increments of 100 GeV c^{-2}. This one-dimensional parameter set lies in a region of the mSUGRA parameter space that requires the gravitino to be the LSP, otherwise it would be an excluded stau LSP region [5]. The lower bound on $M_{1/2}$ is chosen so that the stau is the NLSP, which the arguments in section 1.3 motivate, and the upper bound is chosen so that the SUSY cross-section is high enough to be able to create enough staus each year to perform this analysis.

Next, I pass these staus through the GEANT ATLAS model (see chapter 4), which tracks them until their momentum falls below 0.001 GeV c^{-1}, at which point I assume they have stopped. I then assign each stau a decay time, which I sample from an exponential lifetime distribution, where I input the stau lifetimes into the simulation by hand. The lifetimes I consider are 7, 30, 90, 150 and 365 days. Thus, I have a two-dimensional parameter set that runs

over the stau lifetime and the mSUGRA parameter $M_{1/2}$. I also give each stau a random creation time within a one year period, where this creation time can only be during those times when the beam is on (see section 2.1.1).

Finally, GEANT decays the trapped staus, the decay products of which a model of the trigger system for both ATLAS and ACME could detect. I use the number of stau decays the detectors see to determine the geometric detector acceptance, which I define as the number of stau decays the detector will see over the total number of staus that the Monte Carlo produced. I also determine the average upward-going muon background rates that ATLAS and ACME will see, resulting from neutrino interactions within the earth. One requires the geometric detector acceptance and the background rate to perform the analysis that I present in the chapter 6. This analysis will only consider decay products that are upward-going and decays that occur during those times when the beam is off. This is because, by limiting the analysis to this scenario, one essentially eliminates most sources of background. With the beam off, there will be no proton-proton interactions occurring and by only considering upward-going decay products, one eliminates the background resulting from downward-going cosmic rays.

The sections below describe this analysis in more depth, as well as present the results from it. Finally, one should note that I perform all final analyses within Physics Analysis Workstation (PAW) [76].

5.1 Monte Carlo data production

To simulate the proton-proton collisions of the LHC, I use HERWIG 6.507 [77,78] and, to obtain the SUSY mass spectrum, ISAJET 7.71 [79,80], which one interfaces with HERWIG via the use of ISAWIG [81]. In HERWIG, one is able to remove the requirement for stau decay, which is important for this analysis, where I control the lifetime of the stau as an input paramter to the simulation and allow GEANT to handle the stau decay at a later time. The stau lifetimes that I will consider are 7, 30, 90, 150 and 365 days.

I use mSUGRA to model the SUSY breaking in ISAJET, the parameters

m_o (GeV c^{-2})	$M_{1/2}$ (GeV c^{-2})	A_o (GeV c^{-2})	$\tan\beta$	sgnμ	σ_{SUSY} (pb)
0	300	0	10	> 0	20.22
0	400	0	10	> 0	4.868
0	500	0	10	> 0	1.505
0	600	0	10	> 0	0.542
0	700	0	10	> 0	0.219
0	800	0	10	> 0	0.096
0	900	0	10	> 0	0.045

Table 5.1: I hold the values of m_o, A_o, $\tan\beta$ and μ constant while varying $M_{1/2}$ in the mSUGRA parameter set. These parameters ensure that the stau is the NLSP and that the gravitino is the LSP [5]. The table lists the SUSY cross-section at each of these points, as well.

for which table 5.1 lists. HERWIG calculates the SUSY cross-section at the end of its running. It bases this calculation on the number and type of SUSY particles it produces, which it creates as a result of the SUSY parameters one feeds it. As one can seen in the table, the SUSY cross-section rapidly falls (over three orders of magnitude) as $M_{1/2}$ increases, which could mean that one will encounter difficulties searching for trapped staus at those points in the parameter set, simply as a result of the low number of produced staus.

Figure 5.1 shows the stau energy and $\cos\theta$ distributions for 1×10^6 staus with a lifetime of 30 days at $M_{1/2}$ equal to 300 GeV c^{-2}. For these same parameters, figure 5.2 shows the energy of the staus plotted against $\cos\theta$. As one can see, the highest energy staus travel off in the forward direction, so the distribution of staus trapped near the ATLAS cavern in the overburden and underburden should be roughly isotropic, where one would expect that the detectors would have the highest probability of receiving a signal from those staus that are trapped nearest the interaction point.

5.2 Stau trapping

The output from Herwig, containing the stau creation vertices and momenta, feeds into the GEANT ATLAS model, where the tracking of the staus through ATLAS and into the rock overburden and underburden can commence. GEANT tracks each stau outward from the interaction point until its

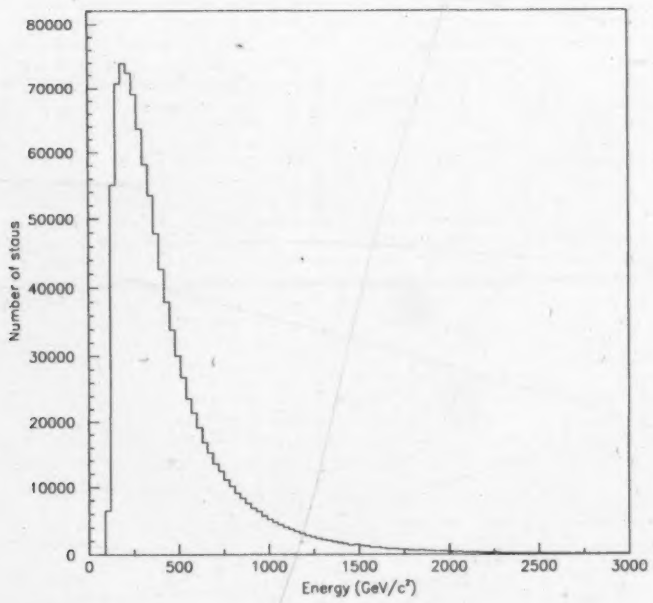

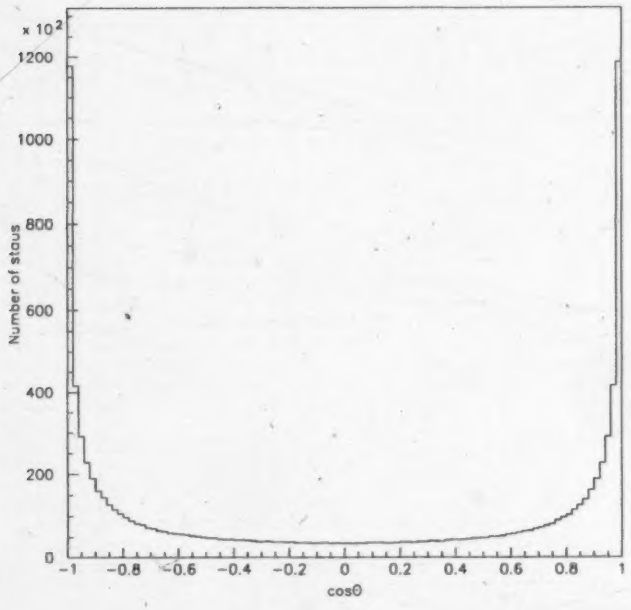

Figure 5.1: The plots show the energy and $\cos\theta$ distributions for 1×10^6 staus with a lifetime of 30 days at $M_{1/2}$ equal to 300 GeV c^{-2}. Notice that most of the staus travel in the forward direction, where $|\cos\theta|$ is near to 1.

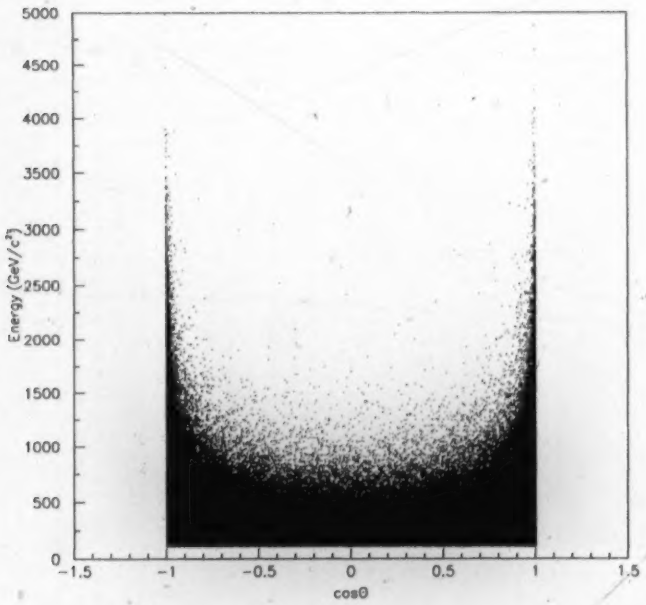

Figure 5.2: The stau energy versus $\cos\theta$ shows that those staus with the highest energies, which are the most likely to travel too far from the detector to have their decay products be seen, travel off in the forward direction. Thus, the distribution of trapped staus from which the detectors will be able to receive a signal is roughly isotropic about the ATLAS cavern.

momentum falls below 0.001 GeV c^{-1}, at which point GEANT assumes the stau to have stopped and ceases tracking it. The program then outputs the stopping positions to file for later use.

Because, as figure 1.4 shows, the stau is heavy, and since it has an electromagnetic, but not a colour charge, one would expect it to act like an extremely massive muon when interacting with matter. Thus, the stau should lose most of its energy via ionization effects, with only a small amount being given off as radiation, which one can then assume to be negligible.

Jonathan Feng, in [5], uses the Bethe-Bloch equation to give the average energy loss per g cm^{-2} resulting from ionization of a charged slepton travelling

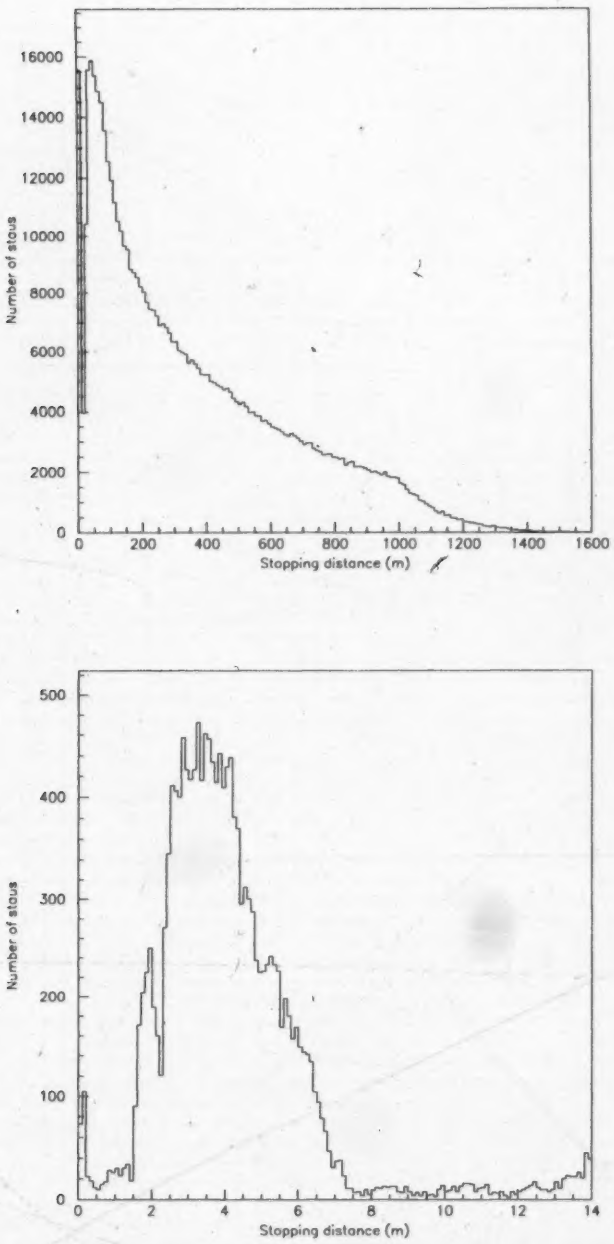

Figure 5.3: The radial stopping positions of staus in ATLAS and the ATLAS overburden and underburden. The bottom plot zooms in to the interaction point, so one can see that a majority of those staus that become trapped in ATLAS stop in the calorimetry. The 'bump' in the tail of the top distribution signals the perpendicular distance from the interaction point to the edge of the GEANT universe. The lifetime of the stau is 30 days and the value of $M_{1/2}$ is 300 GeV c^{-2}.

through matter as

$$\frac{dE}{dx} = Kz^2\frac{Z}{A}\frac{1}{\beta^2}\left(\ln\left(\frac{2m_ec^2\beta^2\gamma^2}{I\sqrt{1+\frac{2m_e\gamma}{M}+\frac{m_e^2}{M^2}}}\right) - \beta^2 - \frac{\delta}{2}\right), \tag{5.1}$$

where $K = 0.307075$ MeV g^{-1} cm^2, z is the slepton charge, Z, A and I are the atomic charge, average nucleon number and mean ionization energy of the material, respectively, m_e is the electron mass and M is the slepton mass. The values of β and γ are familiar from the Lorentz transformations and are $\beta = v/c$ and $\gamma^{-2} = 1 - \beta^2$, where v is the particle velocity. The parameter δ takes into account the polarization of the surrounding medium by the charged slepton, where one writes it as

$$\delta = \Theta(E - E_o)\left(\ln\left(\frac{E^2}{(Mc^2)^2} - 1\right) + \ln\left(\frac{\hbar\omega_p}{I}\right) - \frac{1}{2}\right). \tag{5.2}$$

Here, ω_p is the plasma frequency and E_o is the energy at which the polarization effect becomes significant. The value of E_o (4.4 TeV for lead and 1.3 TeV for water) is generally much higher than the energy of the slepton one is considering, so this effect becomes nearly negligible.

As a result of this, the range of the slepton in matter becomes the integral over the inverse of equation 5.1, which one writes as

$$R(E') = \frac{A}{KZ}\int_{Mc^2+\delta Mc^2}^{E'} dE \frac{\frac{(Mc^2)^2}{E^2} - 1}{\ln\left(\frac{2m_ec^2(E^2-(Mc^2)^2)}{I\sqrt{(Mc^2)^2+2Em_ec^2+(m_ec^2)^2}}\right) + \left(\frac{(Mc^2)^2}{E^2} - 1\right) - \delta}, \tag{5.3}$$

where $Mc^2 + \delta Mc^2$ is the energy at which the value of equation 5.1 reaches a maximum, which should occur for some low value of the slepton velocity, βc. Figure 5.4 shows the range of a 219 GeV c^{-2} stau in lead and in water as a function of energy. It displays both the results of running the stau through the ATLAS simulation and the results of using equation 5.3, where the values of δM, I, E_o and $\hbar\omega_p$ for lead and water, respectively, are 110 MeV c^{-2} and 220 MeV c^{-2}, 820 eV and 75 eV, 4.4 TeV and 1.3 TeV and 61 eV and 21 eV. As one can see, the simulation results from GEANT agree very well with Feng's theory for the range of a stau in lead. For the less dense material, water,

though, Feng's theory provides more stopping power than GEANT delivers; thus, in the simulation, this suggests that less dense materials will not be as effective at trapping staus as Feng's theory would predict. On the other hand, the GEANT universe may trap fewer staus than one would expect, leading to a conservative estimate for the number of staus that ATLAS or the ATLAS overburden or underburden could trap.

At this point in the run, I force the stau to be stable so that it will not decay before coming to rest, where I will later give the stau a decay time that I sample from an exponential distibution according to a lifetime of either 7, 30, 90, 150 or 365 days. Also, during the run, I assign a random creation time within a one year period to every stau, where there is an equal probability that the stau creation occurs at any time when the beam is on. The stau creation time will not fall during a period when the beam is off, since no stau production occurs at those times (see section 2.1.1).

5.3 Stau decay detection

For the final run step, the GEANT simulation reads in the positions and lifetimes of the trapped staus from the outward-going GEANT simulation. GEANT then decays each stau from rest into a SM tau [1] and a gravitino, which occurs 100% of the time. Because one specifies the lifetime of the stau as a parameter input into the simulation, one must recalculate the gravitino mass, since, as equation 1.8 outlines, the gravitino mass is a function of the stau lifetime (or vice versa). This gravitino mass, which table 5.2 tabulates, dictates the kinematics of the stau decay, which, in turn, controls the kinematics of the resulting tau. GEANT also handles the tau decay, where the tau will decay mainly into pions and muons, according to [4]. Fortunately, the signals resulting from both muons and pions hitting ACME and ATLAS will be almost identical; thus, one can utilize signals resulting from the interactions of both particle types with the detectors.

As the stau grand-daughters pass through ACME and ATLAS, GEANT

[1] Of course, this tau will have the same charge as the stau.

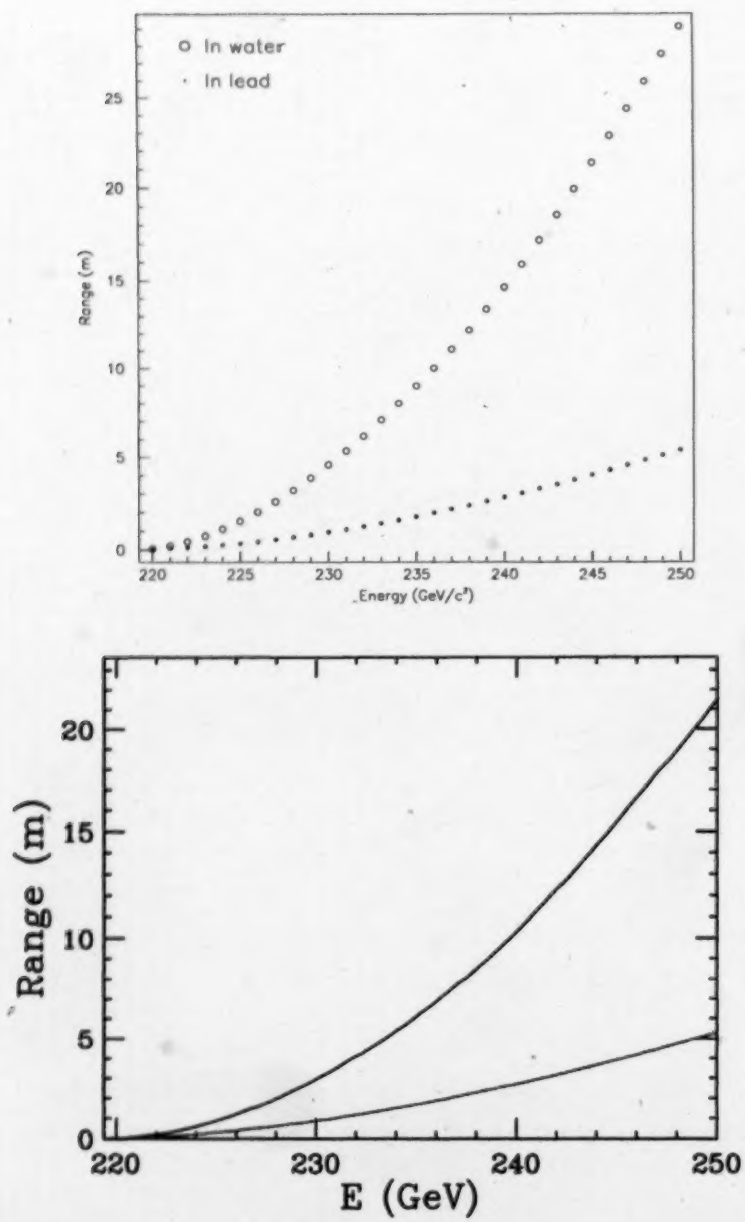

Figure 5.4: The top plot shows the stau range as a function of energy that is output from the simulation for both lead and water. The bottom plot shows Feng's theoretical stau range for both lead and water [5]. The agreement for lead is excellent and the difference for water suggests that GEANT will not be as effective at stau trapping with low-density materials as the theory Feng proposes. The stau mass is 219 GeV c^{-2} in both plots.

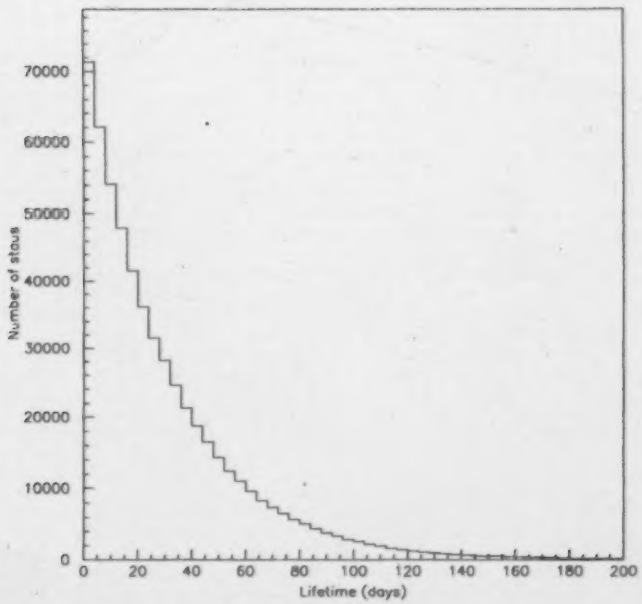

Figure 5.5: The individual stau lifetimes follow an exponential distribution. The plot shows the distribution for a model lifetime of 30 days.

stores their position and momentum information, whereupon one can use this information to form a model trigger decision. The trigger, which I describe in the next section, will decide whether or not the detector will accept the particle as a contributor to the trapped stau signal. The number of particles that the trigger selects as a function of time during those periods when the beam is off is the measurement one requires to perform the stau lifetime analysis that chapter 6 outlines.

τ (days)	7	30	90	150	365	Stau mass
$M_{1/2}$ (GeV c^{-2})	Gravitino mass (GeV c^{-2})					(GeV c^{-2})
300	4.26	8.75	14.81	18.71	27.33	112.22
400	8.62	17.48	28.83	35.70	49.56	148.95
500	14.86	29.60	47.22	57.12	75.63	185.65
600	23.12	45.00	69.14	81.79	104.07	222.35
700	33.45	63.32	93.70	108.69	133.98	258.96
800	45.86	84.18	120.25	137.20	164.92	295.58
900	60.27	107.11	148.21	166.81	196.53	332.13

Table 5.2: The gravitino mass depends both on the mass of the stau, taken from the SUSY mass spectrum, and on the lifetime one chooses for the stau, via equation 1.8.

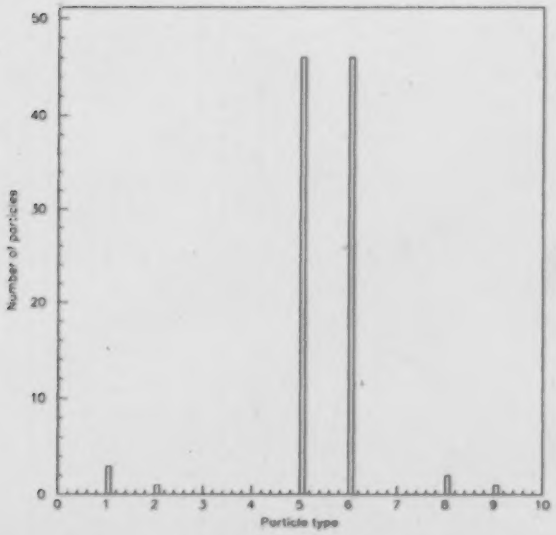

Figure 5.6: Particles, mostly muons (where the particle identification numbers are those from GEANT: 1 for photons, 2 and 3 for e^+ and e^-, 5 and 6 for μ^+ and μ^- and 7, 8 and 9 for π^o, π^+ and π^-, respectively), arrive at ACME. The stau lifetime is 30 days and $M_{1/2}$ is 300 GeV c^{-2}.

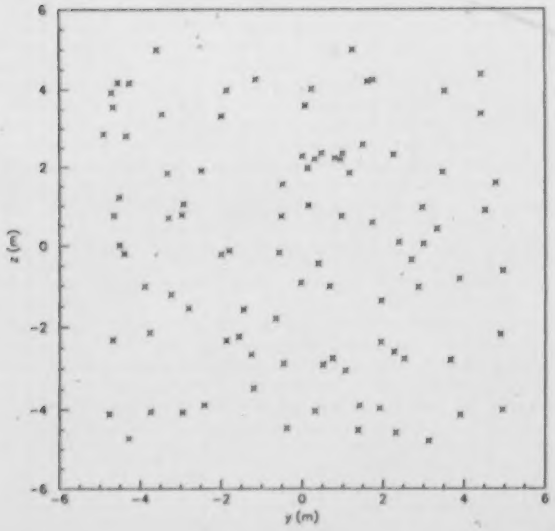

Figure 5.7: The muons and pions from figure 5.6 that would cause a trigger to occur are incident on ACME relatively uniformly. The stau lifetime is 30 days and $M_{1/2}$ is 300 GeV c^{-2}.

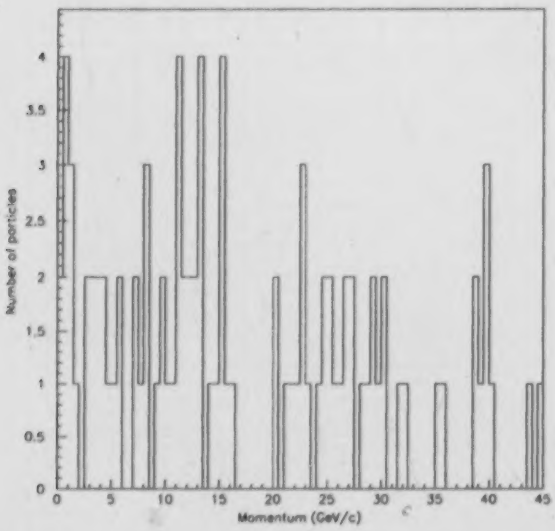

Figure 5.8: These are the momenta of the muons and pions from figure 5.6 that would cause a trigger to occur. The stau lifetime is 30 days and $M_{1/2}$ is 300 GeV c^{-2}.

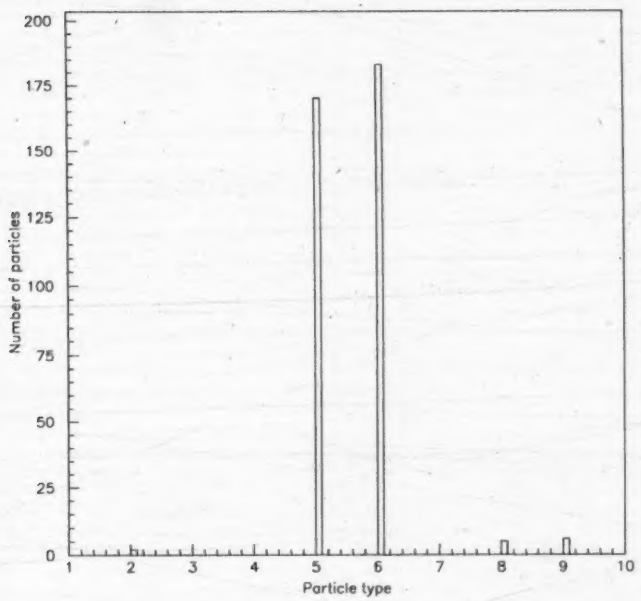

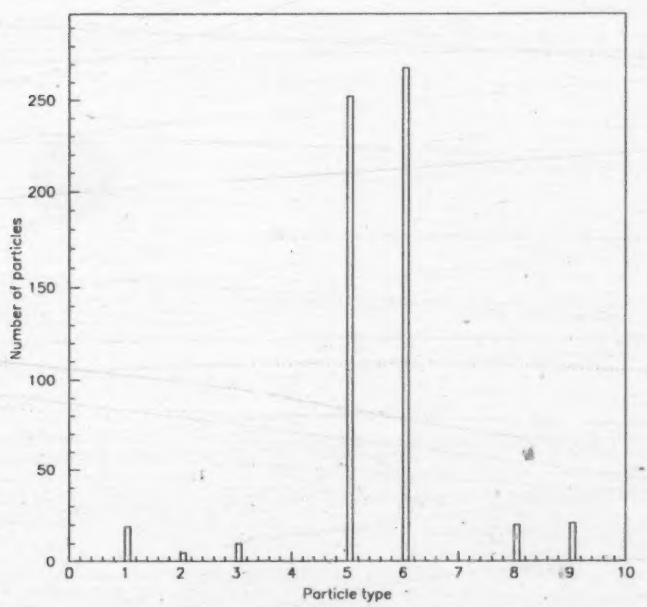

Figure 5.9: The top figure corresponds to RPCs and the bottom corresponds to TGCs. Again, mostly muons are incident on the ATLAS muon system (where the particle identification numbers are the same as those in figure 5.6). The stau lifetime is 30 days and $M_{1/2}$ is 300 GeV c^{-2}.

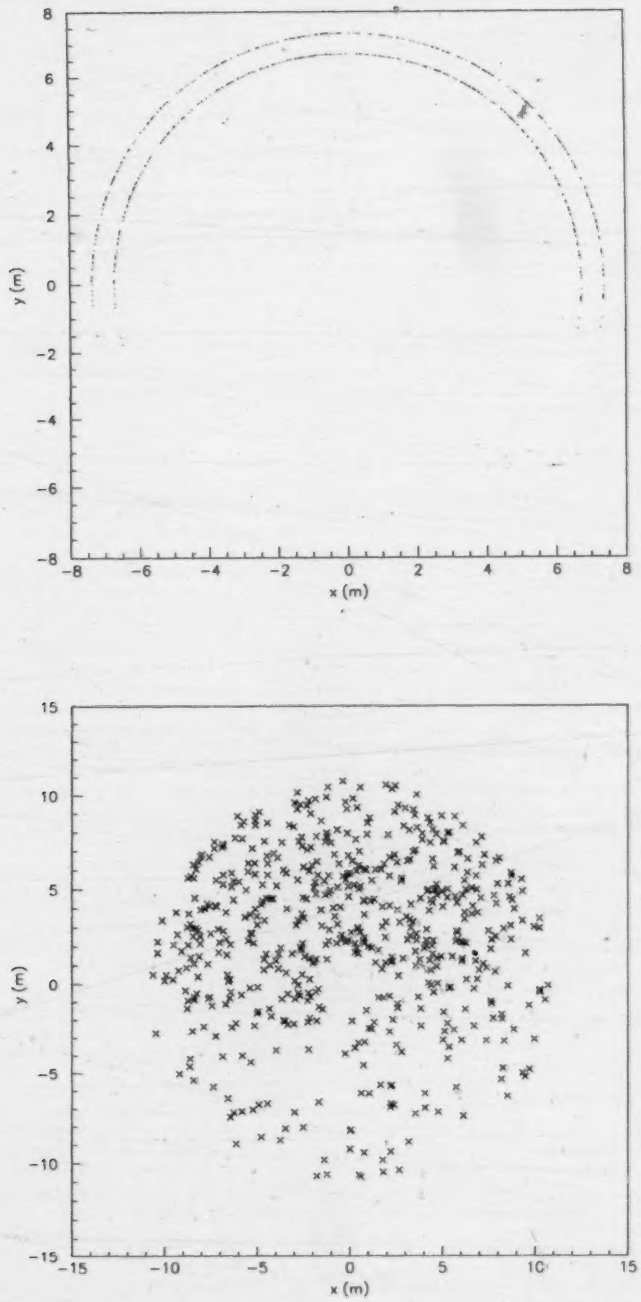

Figure 5.10: The arrival positions of the muons and pions that would cause a trigger in the muon system. Again, the top figure corresponds to RPCs and the bottom corresponds to TGCs. The stau lifetime is 30 days and $M_{1/2}$ is 300 GeV c^{-2}.

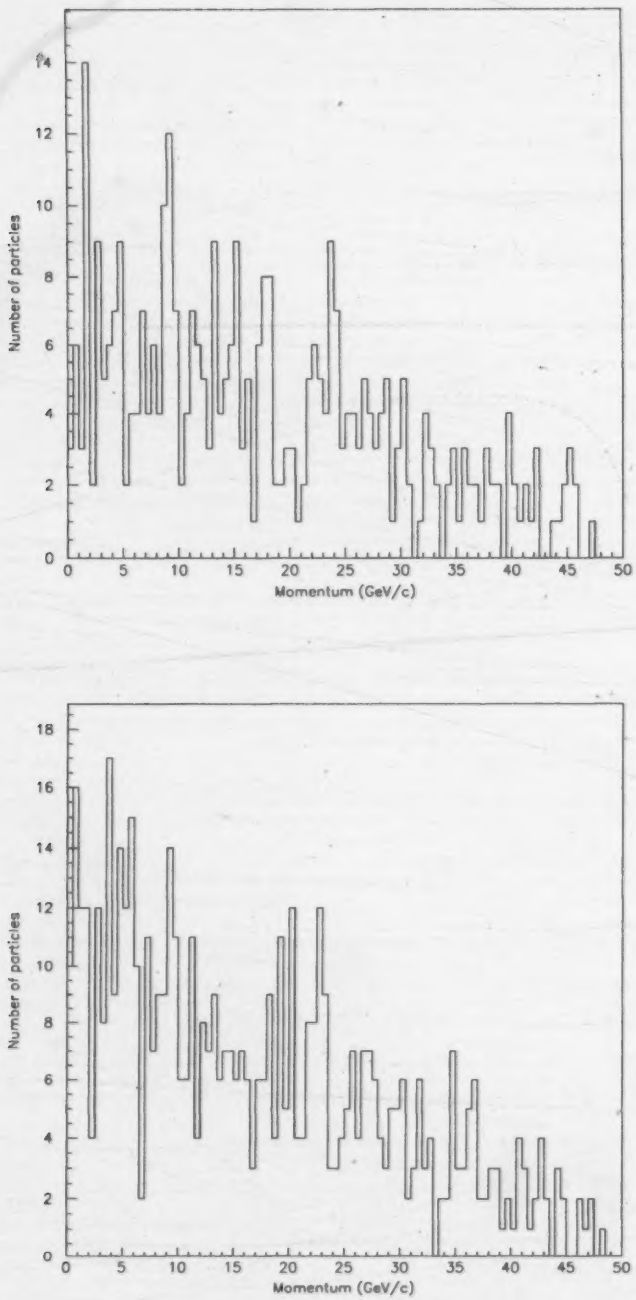

Figure 5.11: The momenta of those muons and pions that would cause a trigger in the muon system, where the top figure corresponds to RPCs and the bottom corresponds to TGCs. The stau lifetime is 30 days and $M_{1/2}$ is 300 GeV c^{-2}.

As a final note, figures 5.6, 5.7 and 5.8 and 5.9, 5.10 and 5.11 show the positions at which the stau grand-daughters are incident on ACME and ATLAS, respectively, as well as the types of particles incident there and their momenta. The position and momentum figures only show those particles that will cause a trigger to occur and that are upward-going. Also, for the ATLAS plots, the arrival positions at the RPCs are approximately uniform in z, where the figure shows the x versus y arrival positions, only, and the arrival positions plot for the triplet TGC overlaps the data from both wheels. Figure 5.12 shows the momenta of all the muons and pions that hit the ATLAS muon system and that may or may not cause a trigger to occur. As one can see, there are particles with very small momentum that the ATLAS trigger may select. These correspond to those particles trapped very near the muon system, such that the distance they must travel in order for the trigger to accept them is small, requiring only a low momentum.

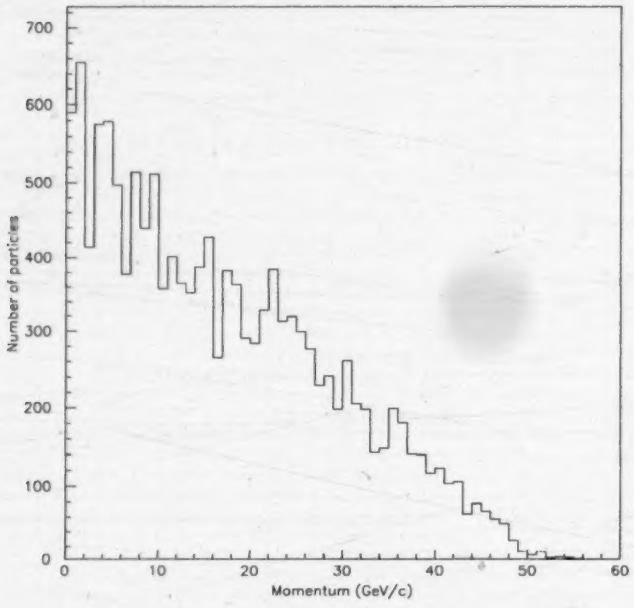

Figure 5.12: The momenta of all muons and pions hitting the ATLAS muon system (both RPCs and TGCs), where the stau lifetime is 30 days and $M_{1/2}$ is 300 GeV c^{-2}.

5.3.1 Trigger decision

Even though the purpose of the cosmic ray trigger is to efficiently trigger on cosmic ray muons using the ATLAS muon system, one should also recognise its ability to detect the charged particles that originate from the decay of trapped staus. To the cosmic ray trigger, the muons and pions that are present in the stau decay chain will, essentially, look like cosmic ray muons, since, with the beam off, the only particles that should be present in the cavern are cosmic rays. As such, one could use the cosmic ray trigger to show evidence of trapped staus.

Fortunately, the cosmic ray trigger has good enough timing accuracy to distinguish between upward- and downward-going particles, so one can essentially eliminate the downward-going cosmic ray muon background rate by exploiting this capability and only searching for upward-going particles [2]. It is because the downward-going cosmic ray muon flux through ATLAS is so high – on the order of kHz – that I choose not to consider downward-going particles. The downward-going cosmic ray muon background would completely dwarf this signal. Now, the only background is the result of upward-going muons that originate from neutrino interactions within the earth, which arrive at ATLAS and ACME at a substantially smaller rate than downward-going cosmic ray muons.

I consider two different triggering situations. In the first, ATLAS and ACME trigger separately on events and each collect a distinct set of event data, where one can combine the results from the two data sets in the final analysis. In the second, I assume that ACME will have access to the ATLAS trigger information since it is, in principle, possible to add the ACME trigger into the set of ATLAS LVL1 triggers via provisions in NIM, as long as the ACME trigger can run according to the standard LHC bunch spacing clock [82]. In

[2] One can, in principle, use ACME as a veto for cosmic ray showers, whereby one assumes that any bundle of particles passing through both ACME and ATLAS constitutes a cosmic ray shower and is not a signal particle. This could allow one to effectively reduce the downward-going background rate in the ATLAS barrel region to a manageable level, perhaps making an analysis like that in chapter 6 possible. Nevertheless, this thesis does not concern itself with a study of this sort and, as a result, I consider only upward-going particles.

this way, ACME can directly supplement the total amount of event data that ATLAS collects, where one will not trigger on a single event twice. This, in turn, could hopefully lead to a better statistical analysis of the data. Also, since the triggering efficiency of ACME should be better than that of the ATLAS muon system, ACME should be able to catch some of those events that the ATLAS trigger misses. In chapter 6, I compare these two triggering scenarios to determine which may be of more value, where the first method will only reduce the error in the lifetime analysis if the errors resulting from each distinct data set are comparable [3].

The model of the ACME trigger requires hits in both scintillating planes that occur within 25 ns of one another. If this occurs, I assume that the event passes the trigger, where the trigger has an inherent efficiency of 100%.

For the ATLAS barrel muon trigger model, I require a hit in both of the inner two RPC layers where a straight line connecting the two hit points passes within a 2 m sphere of the interaction point, which is an approximation of the actual RPC electronics. If a particle passes through both the upper and lower half of the muon barrel and passes the trigger selection twice, then I count the particle as passing the trigger decision only once, regardless of the time of flight of the particle between triggering in the two halves. Technically, this time of flight could be less than 25 ns if the particle travels through the muon barrel sector at a large value of |x|, but I assume that it would be possible to determine that the two triggers were a result of the same particle, using offline trajectory matching. I give the barrel trigger an inherent efficiency of 83%, in line with simulation [83], where I subject each trigger event in the simulation to this efficiency cut.

In the endcap, I require a single hit in the TGC triplet layer to cause a trigger. This is because the cosmic ray trigger in this region works by introducing dummy hits into the layers surrounding the inner triplet layer, so almost any particle that hits the endcap will cause a trigger to occur. If

[3] In fact, the errors in the individual measurements of the lifetime must be within a factor of $\sqrt{3}$ of one another in order to reduce the error in the measurement, assuming one adds the errors in quadrature.

a single particle passes the trigger decision twice, then I only count a single trigger as occurring, for the same reasons that I described above. Also, if a single particle passes both the barrel and endcap trigger selection, then I also only count a single trigger as occurring, where the first trigger to happen is the one I select. Again, I assume it is possible to determine that it is the same particle causing these triggers and count only one trigger to avoid inflating the event rate. The endcap trigger model has an inherent efficiency of 95%, where, again, I assert this efficiency cut on each trigger event.

5.3.2 Detector acceptance

To parameterize how sensitive ATLAS and ACME are to the signal of the decaying staus, I define a geometric detector acceptance α as the number of stau decays the detectors record over the total number of staus that the proton-proton collisions produce. To do so, I generate six runs of 5×10^5 proton-proton collisions each, where, because of R-parity conservation, every collision results in the production of two staus. I do this once for each $M_{1/2}$ and lifetime pair of model points that I am considering, for a total of 35×6 runs. One should note that the number of stau decay products the detectors will actually see when the beam is off will then be equal to the number of stau decays that occur during that time multiplied by this geometric acceptance.

Figure 5.13 shows the ATLAS and ACME acceptance as a function of both $M_{1/2}$ and lifetime. The figure shows the acceptance of both upward- and downward-going particles for comparitive purposes, where one can note that the acceptance of upward-going particles is greater than the acceptance of downward-going particles of both detectors, lending additional credit to performing an upward-going analysis, only. In fact, the upward-going acceptance of ACME is four times greafer than its downward-going acceptance.

The errors in the acceptance measurements are the standard deviations that one calculates as

$$\sigma_\alpha = \sqrt{\frac{1}{N-1}\sum_{i=1}^{N}(\alpha_i - \bar{\alpha})^2}, \tag{5.4}$$

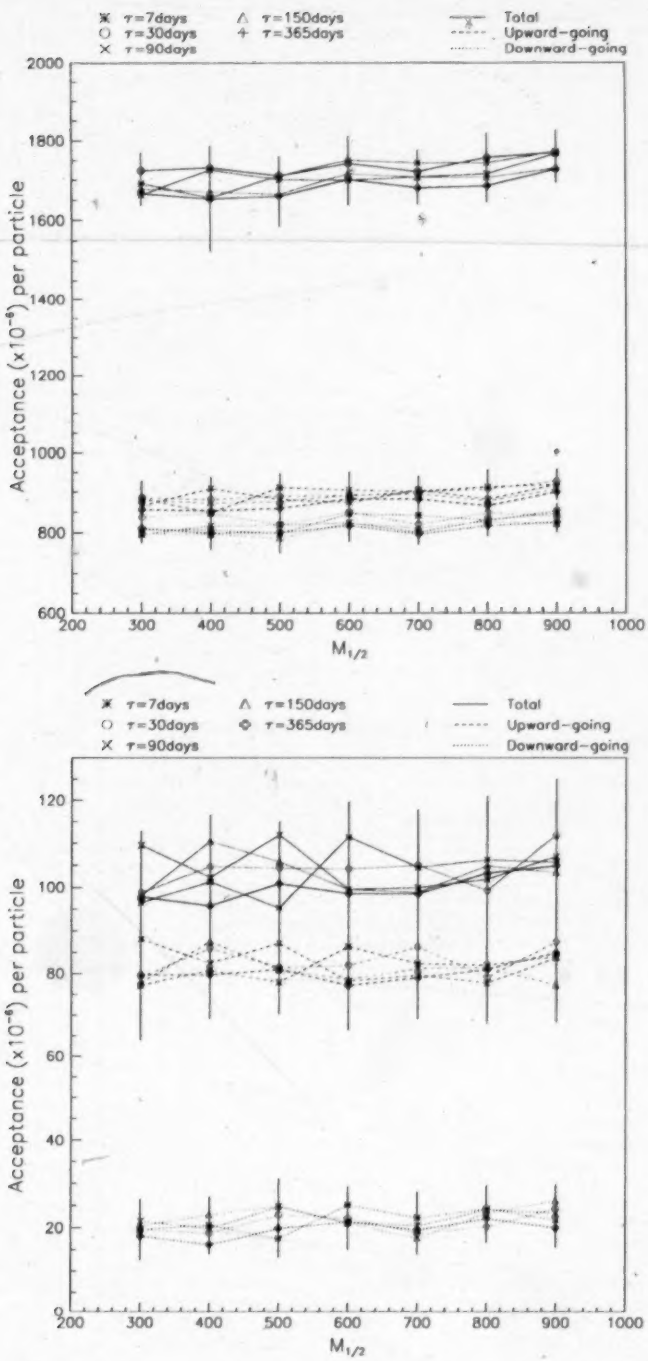

Figure 5.13: The ATLAS (top) and ACME (bottom) detector acceptance as a function of $M_{1/2}$ and lifetime. The plots show both the acceptance of upward- and downward-going particles, as well as the total acceptance. Notice that, for both detectors, the acceptance of upward-going particles is greater than the acceptance of downward-going particles.

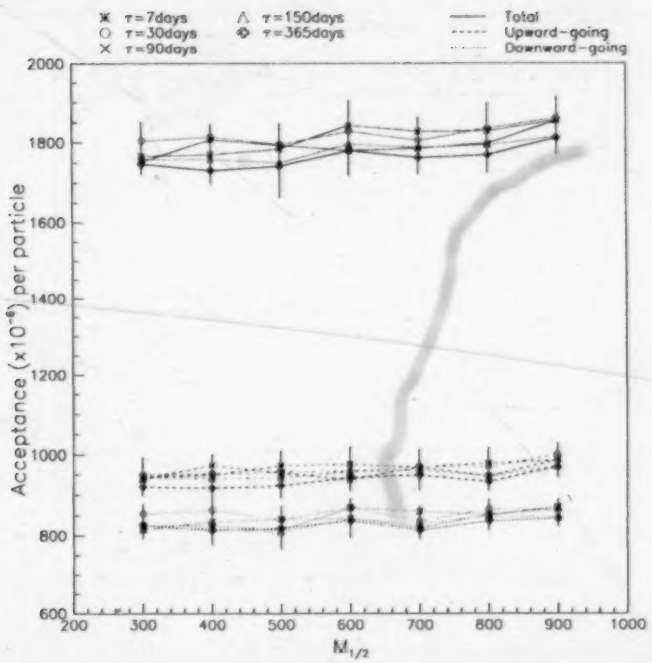

Figure 5.14: The total acceptance upon combining the results of both ATLAS and ACME. Here, the acceptance of upward-going particles is still greater than the acceptance of downward-going particles.

where N is equal to 6, the total number of runs, α_i is the acceptance of the i^{th} run and $\bar{\alpha}$ is the average acceptance. One should also note that the total acceptance of each detector is the sum of the upward- and downward-going acceptances of each. I calculate the error in the total acceptance using equation 5.4, not by adding the errors of the upward- and downward-going acceptances in quadrature. One can use these acceptances when considering ATLAS and ACME to be separate detectors, collecting distinct data sets (see section 5.3.1).

To analyse the triggering situation when ACME acts only as a supplementary detector to ATLAS (see section 5.3.1), one requires the combined acceptance of both detectors. Figure 5.14 shows this combined acceptance of ATLAS and ACME for both upward- and downward-going particles, where one can see that the acceptance of upward-going particles is greater than the acceptance of downward-going particles. Equation 5.4 again gives the errors in the acceptances.

To be explicit, tables 5.3, 5.4 and 5.5 list the upward-going acceptances for ATLAS, ACME and the combination of the two detectors, respectively. Because the analysis will only consider upward-going particles and figures 5.13 and 5.14 include the downward-going acceptances only for comparison, tables 5.3, 5.4 and 5.5 do not include the downward-going acceptances.

τ	7 days		30 days		90 days		150 days		365 days	
$M_{1/2}$	α	σ_α	α	σ_α	α	σ_α	α	σ_α	α	σ_α
(GeV c^{-2})	$\times 10^{-6}$									
300	884.0	18.0	885.5	43.4	866.5	26.8	879.7	27.1	856.7	17.3
400	847.7	91.2	882.5	28.8	908.5	25.7	873.3	22.7	853.3	24.3
500	911.3	36.5	890.5	34.2	881.8	19.1	876.7	42.2	859.7	31.6
600	905.0	47.0	890.7	35.2	874.7	25.4	892.5	39.4	883.2	18.4
700	901.3	41.0	900.3	37.1	906.0	10.4	895.3	24.8	882.7	37.0
800	913.0	43.6	907.7	26.2	882.3	17.2	879.0	26.7	866.7	15.8
900	918.8	16.3	927.8	29.6	919.2	40.0	907.3	19.7	900.7	17.6

Table 5.3: ATLAS upward-going acceptance.

τ	7 days		30 days		90 days		150 days		365 days	
$M_{1/2}$	α	σ_α	α	σ_α	α	σ_α	α	σ_α	α	σ_α
(GeV c^{-2})	$\times 10^{-6}$									
300	77.2	13.4	79.3	10.9	88.2	6.9	77.8	8.9	79.7	6.7
400	80.8	11.8	86.0	7.0	82.5	10.8	87.5	6.8	79.7	10.3
500	78.0	7.8	81.5	3.7	87.2	5.9	81.0	7.9	81.0	9.6
600	86.3	6.9	82.0	9.4	78.3	7.8	78.7	4.6	77.2	10.9
700	82.3	11.5	86.3	8.9	79.7	10.2	81.3	10.8	79.0	9.9
800	82.0	5.9	79.2	4.8	77.8	4.5	81.5	13.5	81.0	10.0
900	84.0	10.6	87.5	15.0	83.7	4.5	77.3	9.2	84.8	7.3

Table 5.4: ACME upward-going acceptance.

τ	7 days		30 days		90 days		150 days		365 days	
$M_{1/2}$	α	σ_α	α	σ_α	α	σ_α	α	σ_α	α	σ_α
(GeV c^{-2})	$\times 10^{-6}$									
300	944.3	17.7	950.0	43.7	938.2	25.1	943.0	29.1	920.7	21.8
400	947.7	26.4	951.5	35.3	973.8	27.8	941.3	20.5	917.3	24.4
500	971.8	37.2	955.7	35.2	952.7	22.6	942.2	48.7	923.7	32.0
600	975.2	45.1	958.5	38.0	937.5	28.4	956.2	40.9	943.5	18.4
700	968.0	45.8	969.8	37.1	967.8	13.0	960.7	29.9	949.2	38.5
800	978.3	39.0	969.3	26.0	945.0	24.2	945.5	22.0	933.3	24.1
900	986.0	22.5	1000.8	24.7	987.8	40.4	970.5	20.8	968.7	25.8

Table 5.5: Total upward-going acceptance.

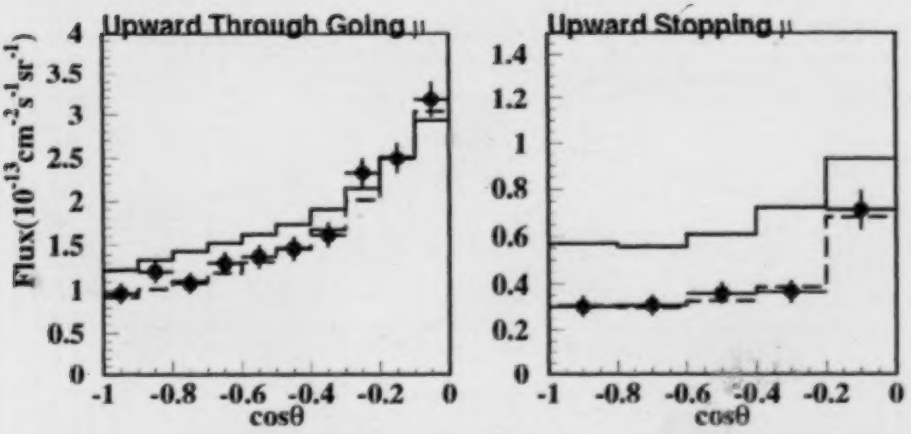

Figure 5.15: The upward-going muon flux at Super-Kamiokande for both through-going and stopping muons with energies greater than 1.6 GeV. Pointing straight up corresponds to $\cos\theta$ equal to -1. The solid lines correspond to theory with no neutrino oscillations and the dashed lines correspond to theory assuming neutrino oscillations. As one can see, the data fits the neutrino oscillations case [24].

5.4 Background sources

If one searches for the signal of the trapped stau decays only when the beam is off, where the cosmic ray trigger can run during this time, then there will be no background to the process resulting from the proton-proton collisions or from the beam, itself, in terms of beam-halo and beam-gas rates [67]. As such, one must only contend with cosmic rays and upward-going muons resulting from neutrino interactions inside the earth. Since both the ATLAS cosmic ray trigger and ACME will have the ability to distinguish between upward- and downward-moving particles, if one only looks at those particles that are upward-going, which is the case that I consider in this thesis, then one can essentially eliminate the cosmic rays as a source of background.

Circa the beginning of the twenty-first century, the Super-Kamiokande collaboration measured the upward-going neutrino-induced muon rate, as [22–24] outline. Figure 5.15 shows the upward-going muon flux as a function of zenith angle resulting from 1289 days of Super-Kamiokande running. As one can see, the flux increases for muons that arrive at higher zenith angles,

corresponding to neutrinos that traverse a shorter distance through the earth, where, for $\cos\theta$ equal to -1, the neutrinos travel through nearly 13000 km of earth before arriving at the detector, whereas for $\cos\theta$ equal to 0, the neutrinos only pass through approximately 500 m of rock. The minimum muon energy is 1.6 GeV.

To calculate the average upward-going muon flux impinging upon ATLAS and ACME, I assume that the neutrino interactions that create the muons occur at the cavern walls. Because the solid angle and effective area of the detectors depend on how far away from the detectors the muon is, assuming this distance is the distance to the cavern wall, rather than the distance to that place in the rock where the muon actually originated, will only increase the solid angle and effective area that the muon will see. This serves to inflate the background rate through the detectors, which implies that I am conservatively over-estimating the background rates.

For the muon barrel, I use the effective area and solid angle of a circle of radius 2 m at the interaction point to calculate the background rate. This mimicks the trigger decision, where the trigger only selects particles that pass within a 2 m sphere of the interaction point. This leads to an average background rate of 0.005 day^{-1}. Similarly for the muon endcap, I use the solid angle and effective area of a circle of radius 12.035 m at the position of the outermost TGC layer to perform this same calculation, resulting in an average background rate of 0.16 day^{-1}. Thus, I take the average upward-going background rate through the muon system to be 60 year^{-1}. Also, I assume that the trigger will select all background events with 100% efficiency (again to ensure that I am not underestimating the background rate).

Since it is a square plane, the geometry of ACME requires more careful consideration when determining the background rate. For this detector, appendix B contains a derivation of both the solid angle and effective area, as functions of zenith angle. Using those results, as well as the fact that ACME does not lie centered in the ATLAS cavern so that muons originating from either wall will see a different solid angle from complementary zeniths, the average upward-going muon flux that ACME should see will be on the order of 1

year^{-1}, which is much smaller than the background rate that ATLAS will see. Of course, if ACME becomes operational, then one could, hopefully, directly measure this background rate.

Chapter 6

Analysis II

This chapter outlines the main analysis of this thesis, that being the determination of the trapped stau lifetime and the SUSY cross-section. The first section derives the stau production and decay rates, which rely on the stau lifetime and the SUSY cross-section, that one would expect to see as a function of time at the LHC [84]. One may refer to section 2.1.1 and table 6.1 for an overview of the LHC operating schedule that I assume.

The second section presents the results of performing a fit of the data that the trigger model (see section 5.3.1) selects to determine the stau lifetime and the SUSY cross-section. I perform the analysis for both ATLAS and ACME separately, as well as by treating them like one effective detector. For the ATLAS-only case, I perform the lifetime fits 100 times per lifetime and $M_{1/2}$ parameter pair in order to determine the statistical spread in the lifetimes and cross-sections one can expect this fitting method to produce. I do the same thing for each of the three detector scenarios at a lifetime of 30 days, while covering the entire $M_{1/2}$ range, to determine which scenario will produce the best fit results. One should note that I only consider those times when the LHC beam is off and only look at upward-going stau decay products in order to do these fits. This effectively reduces the background to the stau decay signal to that of upward-going muons resulting from neutrino interactions within the earth.

Days in year	Beam condition	Period i	Luminosity year 1-3	Luminosity year 4-6
1 - 25	on	1	low	high
26 - 28	off	1	–	–
29 - 53	on	2	low	high
54 - 56	off	2	–	–
57 - 81	on	3	low	high
82 - 84	off	3	–	–
85 - 109	on	4	low	high
110 - 112	off	4	–	–
113 - 137	on	5	low	high
138 - 140	off	5	–	–
141 - 165	on	6	low	high
166 - 168	off	6	–	–
169 - 193	on	7	low	high
194 - 196	off	7	–	–
197 - 221	on	8	low	high
222 - 224	off	8	–	–
225 - 365	off	–	–	–

Table 6.1: This is the LHC operating schedule scenario that I assume. Low luminosity and high luminosity correspond to an integrated luminosity over the year of running of 10 fb^{-1} year^{-1} and 100 fb^{-1} year^{-1}, respectively.

6.1 Stau production and decay rates

During those periods when the beam is operational, the proton-proton collisions occurring within ATLAS will lead to the production of staus according to the SUSY cross-section, a model-dependent list of which table 5.1 shows. If one takes the integrated luminosity for year j of running at the LHC to be L_j, then the stau production rate at ATLAS, assuming R-parity conservation, will be

$$R_j = 2\frac{L_j \sigma_{\text{SUSY}}}{T_{on}}, \tag{6.1}$$

where the 2 results from having two sleptons in the final state for every SUSY interaction that occurs and T_{on} is the total time over the year that the beam is on, which, according to the LHC operating schedule I assume, is 200 days. Table 6.1 outlines the six year operating scenario that I will use, including the LHC integrated luminosities that I assume for each year.

Now, if one assumes that, at some time t during the year, there are $N(t)$

undecayed staus trapped in or around ATLAS, then the number of staus that survive until a time $t + dt$ will be

$$N(t + dt) = N(t)\left(1 - \frac{dt}{\tau}\right) \tag{6.2}$$

if the beam is off at time t and

$$N(t + dt) = N(t)\left(1 - \frac{dt}{\tau}\right) + Rdt \tag{6.3}$$

if the beam is on at time t, where τ is the stau lifetime. After re-zeroing the time at every beam turn-on and -off, let the number of undecayed staus remaining at beam turn-on be N^o and the number of undecayed staus remaining at beam turn-off be N^f. Thus, solving equations 6.2 and 6.3, respectively, the number of undecayed staus remaining, as a function of time, becomes

$$\begin{aligned} N_{off} &= N^f e^{-t/\tau} \\ N_{on} &= N^o e^{-t/\tau} + R\tau(1 - e^{-t/\tau}). \end{aligned} \tag{6.4}$$

Using equation 6.4 and labelling the eight LHC operating periods with the index i, one arrives at

$$\begin{aligned} N^o_{1,1} &= 0 \\ N^o_{1,j} &= N^f_{8,j-1} e^{-t_{sd}/\tau},\ j \geq 2 \\ N^o_{i,j} &= N^f_{i-1,j} e^{-t_{off}/\tau},\ i \in [2, 8] \\ N^f_{i,j} &= N^o_{i,j} e^{-t_{on}/\tau} + R_j\tau(1 - e^{-t_{on}/\tau}), \end{aligned} \tag{6.5}$$

where t_{sd}, t_{off} and t_{on} are the amounts of time during a shutdown, offline and operational period of the LHC [1]. Thus, there is a set of equations that one can solve via iteration for the number of undecayed staus present in or around ATLAS as a function of time. Figure 6.1 shows the cumulative number of stau decays that one would expect to occur each year, as a function of the number of days after the shutdown period begins and figure 6.2 shows the total number of decays one would expect to see over the six years of running. Both plots are for a stau lifetime of 30 days.

[1]The shutdown period is the long 20 week plus 3 day (144 days total) period during which time the LHC beam is shut off, the offline periods are the short three-day down times during beam operation and each operational period consists of 2[illegible] days of running.

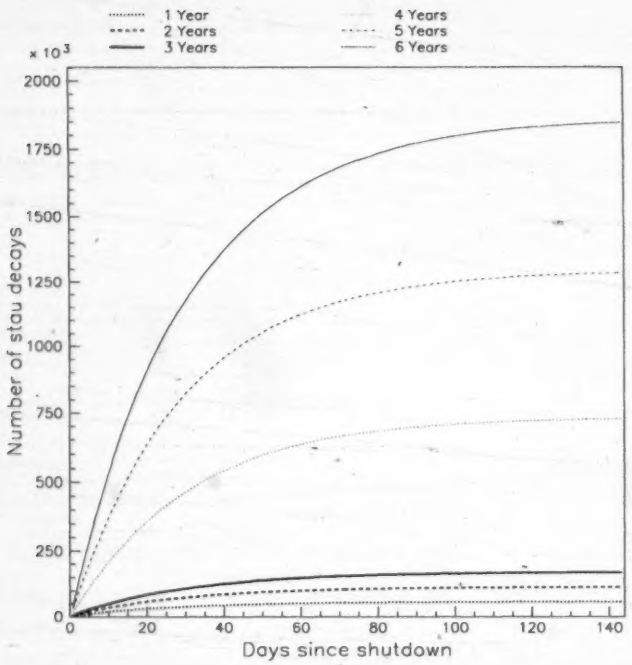

Figure 6.1: The sum of the number of stau decays that occur as a function of time during the LHC shutdown period after either 1, 2, 3, 4, 5, or 6 years of running. The stau lifetime is 30 days and $M_{1/2}$ is 300 GeV c^{-2}.

Instead of solving equations 6.5 recursively, one can use them to determine analytic solutions for the number of undecayed staus remaining at the beginning and end of each operational period, as appendix C shows, giving

$$\begin{aligned} N^f_{i,j} &= N^o_{1,j} e^{-i(t_{off}+t_{on})/\tau} e^{t_{off}/\tau} + \\ &\quad R_j \tau (1 - e^{-t_{on}/\tau}) \sum_{n=0}^{i-1} e^{-n(t_{off}+t_{on})/\tau} \\ N^o_{1,j} &= \sum_{m=1}^{j-1} R_m \tau (1 - e^{-t_{on}/\tau}) \sum_{n=0}^{7} e^{-n(t_{off}+t_{on})/\tau} \cdot \\ &\quad e^{-(j-1-m)(7t_{off}+8t_{on})/\tau} e^{-(j-m)t_{sd}/\tau}. \end{aligned} \tag{6.6}$$

Meanwhile, the number of staus that decay during shutdown period i of year j is

$$\begin{aligned} N^{decays}_{i,j} &= N^f_{i,j}(1 - e^{-t_{off}/\tau}),\ i \in [1,7] \\ N^{decays}_{8,j} &= N^f_{8,j}(1 - e^{-t_{sd}/\tau}). \end{aligned} \tag{6.7}$$

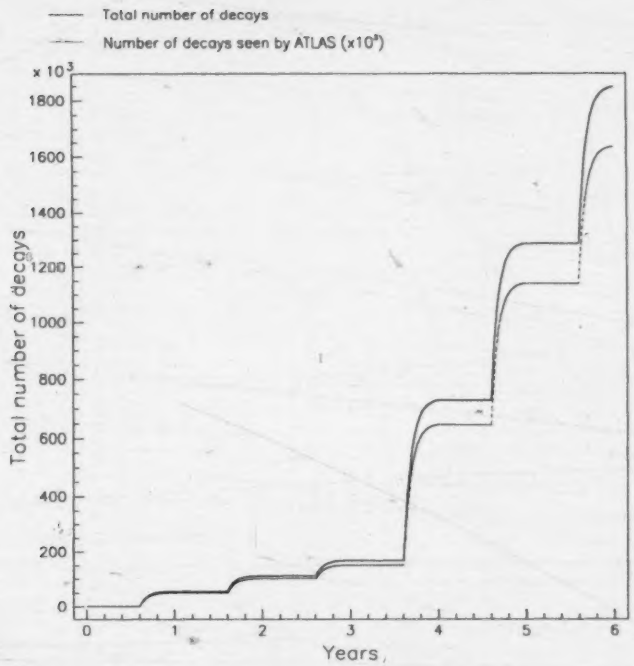

Figure 6.2: The total number of stau decays that occur as a function of the six years of running. The bottom line is the number of stau decays that one would expect the ATLAS detector to see ($\times 10^3$) in that period, which is the total number of decays that occur multiplied by the geometric acceptance. The stau lifetime is 30 days and $M_{1/2}$ is 300 GeV c^{-2}.

Thus, the number of decays the detectors are sensitive to will be the total number of decays that occur during the shutdown period multiplied by the detector acceptance (see section 5.3.2).

6.2 The stau lifetime and SUSY cross-section fit

From equation 6.6, one should note that the number of undecayed staus remaining at the end of each operational period is proportional to the stau production rate. As such, the number of stau decays that ATLAS and ACME will be able to detect, which is the detector acceptance α times the number of stau decays that occur, will also be proportional to the stau production rate. Thus, the number of candidate stau decays the detectors will be sensitive to

each year will be

$$N_{hits} = \alpha N_{8,j}^{f}(1 - e^{-t/\tau}) + \beta t, \tag{6.8}$$

where β is the background rate and equation 6.6 gives $N_{8,j}^{f}$. In order to increase the size of the data set, one can take the sum over multiple operational years of the number of candidate stau decays the detectors see, which leads to

$$N_{hits} = \alpha \left(\sum_{j=1}^{n} N_{8,j}^{f}(1 - e^{-t/\tau}) \right) + n\beta t, \tag{6.9}$$

where the total number of years I will consider is six: three at low luminosity and three at high luminosity. Because the luminosity of the LHC can fluctuate over the course of the year so one cannot precisely know the final integrated luminosity for each year a priori, I assume order-of values of 10 fb^{-1} year^{-1} and 100 fb^{-1} year^{-1} for low and high luminosity, respectively.

As such, one can perform a fit of the data from those 144 day shutdown periods when the beam is off in order to determine the stau lifetime, SUSY cross-section and background rate, where the fit is

$$\begin{aligned} N &= A(1 - e^{-Bt}) + Ct \\ A &= \alpha \sum_{j=1}^{6} N_{8,j}^{f} \\ B &= \frac{1}{\tau} \\ C &= 6\beta. \end{aligned} \tag{6.10}$$

Of course, the SUSY cross-section, which one obtains through fit parameter A, then depends on the stau lifetime, so one must use the resulting value of B in order to determine the SUSY cross-section.

Figure 6.3 shows the lifetime fits for the ATLAS and ACME detectors, where the true stau lifetime is 30 days, the true SUSY cross-section is 20.2 pb^{-1} and the background rates for ATLAS and ACME are 60 year^{-1} and 1 year^{-1}, respectively, giving a combined background rate of 61 year^{-1}. Table 6.2 lists the results of the fit, as well as the result of averaging the values from the two fits (or summing, in the case of the background fit), where one adds the errors in quadrature. As one can see from the fit results, one can

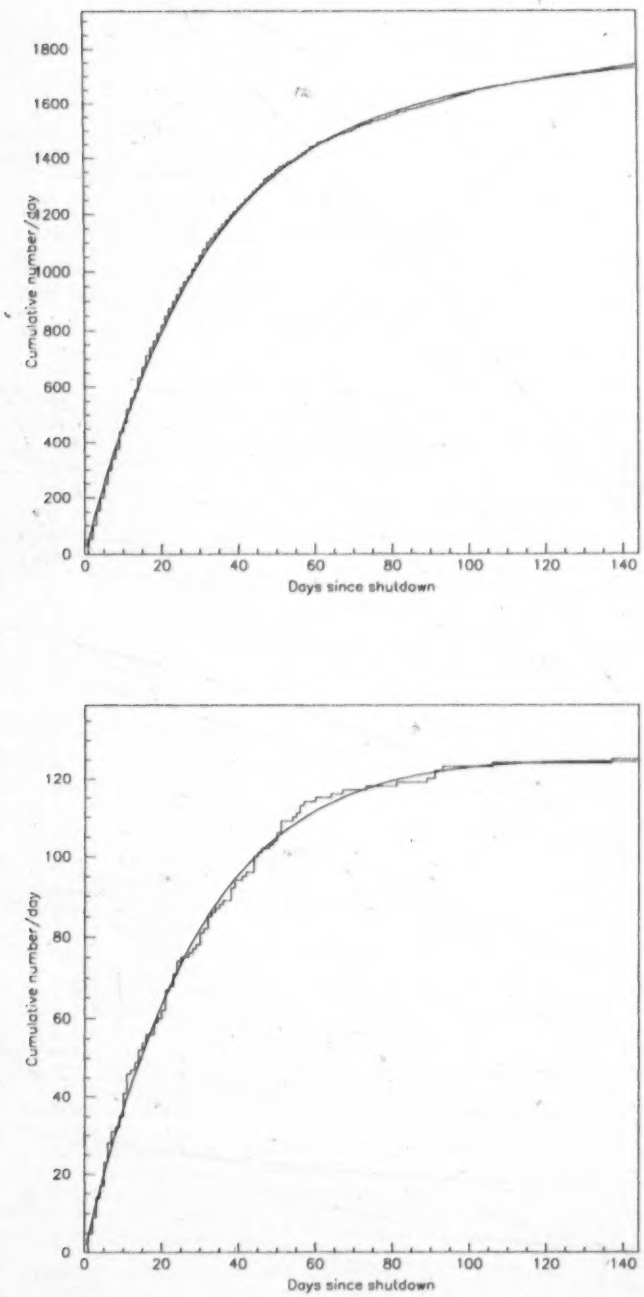

Figure 6.3: Equation 6.10 fits the number of particles that ATLAS (top) and ACME (bottom) see decay, as a function of the number of days after the beam turn off. The stau lifetime is 30 days and $M_{1/2}$ is 300 GeV c^{-2}.

	τ (days)	σ_{SUSY} (pb^{-1})	β ($year^{-1}$)
ATLAS	30.4 ± 1.0	20.1 ± 1.1	61.5 ± 21.0
ACME	30.4 ± 3.1	18.7 ± 3.0	-3.4 ± 5.6
Average	30.4 ± 1.6	19.4 ± 1.6	58.1 ± 21.7

Table 6.2: The lifetime, cross-section and background values resulting from a fit of the number of stau decays seen by ATLAS and ACME as a function of the number of days after the beam turn off. The real stau lifetime is 30 days, the real cross-section is 20.2 pb^{-1} and the real background rates are 60 $year^{-1}$ for ATLAS and 1 $year^{-1}$ for ACME.

	τ (days)	σ_{SUSY} (pb^{-1})	β ($year^{-1}$)
Combined	30.3 ± 1.0	20.1 ± 1.1	66.9 ± 22.7

Table 6.3: The lifetime, cross-section and background values resulting from a fit of the combined ATLAS and ACME data.

do a better reconstruction job with ATLAS alone, with a discrepancy in the lifetime of 1.3%, a discrepancy in the cross-section of 0.5% and a discrepancy in the background rate of 2.5%, where each of the fit values agrees within error with the real values. One can reconstruct these values with ACME, as well, but the accuracy of doing so is not as great, with a discrepancy in the lifetime of 1.3%, a discrepancy in the cross-section of 7.0% and a discrepancy in the background rate of 440.0%, which is a result of the detectors seeing mostly signal events, not background. Again, all fits agree within error of the actual values, but the errors in the fits, as table 6.2 shows, are larger for ACME than the errors in the fits using the ATLAS data.

Now, looking at the combined ATLAS and ACME data, where one uses ACME only as a supplement to the data that ATLAS is able to collect, one arrives at a fit like figure 6.4 shows, the results of which table 6.3 supplies. Here, the lifetime fit results in a lifetime that is closer to the actual lifetime, with a discrepancy of 1.0%. Adding ACME does not change the result of using only the ATLAS data to determine the cross-section, and the background rate, which should be 61 $year^{-1}$, still agrees within error, where the discrepancy is 9.7%.

As it would seem, initially, the fit using the combined data set seems to be

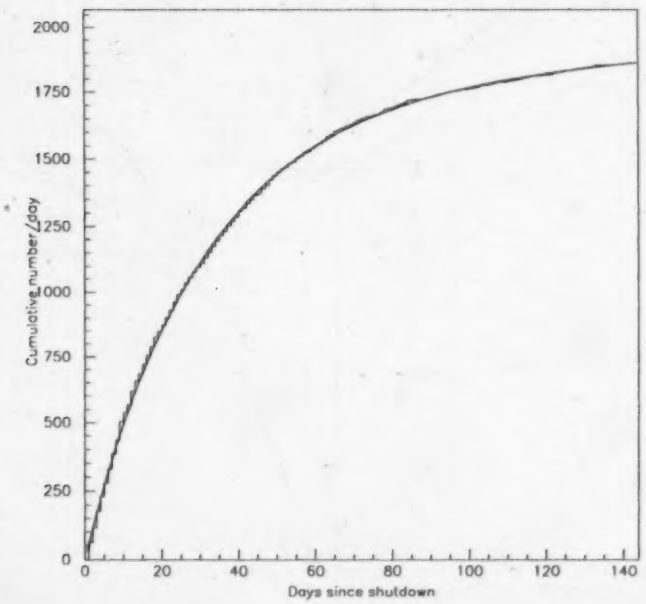

Figure 6.4: Equation 6.10 fits the combined data from both ATLAS and ACME, as a function of the number of days after the beam turn off. The stau lifetime is 30 days and $M_{1/2}$ is 300 GeV c^{-2}.

marginally better than the averaging of the two separate data sets, or the use of only the data that ATLAS collects. To test this, I performed 100 fits on 100 distinct data sets to determine the spread in fit lifetimes, cross-sections and background rates, for a lifetime of 30 days over the entire $M_{1/2}$ range. Table 6.4 lists the results of this test. Figures 6.5, 6.6, 6.7, 6.8, 6.9 and 6.10 show the spreads in the lifetimes, cross-sections and background rates for ATLAS, ACME and the combination of the two, respectively, at $M_{1/2}$ equal to 300 GeV c^{-2}. As one can see, the fits begin to break down for each of the three detector scenarios as the value of $M_{1/2}$ becomes large. This is a result of the actual SUSY cross-section (see table 5.1) becoming very small there, so the number of stau decays being seen is not significantly higher than the background rate. On the other hand, because most of what the detectors see at these values of $M_{1/2}$ is background, the background values one obtains from the fits become more accurate as the value of $M_{1/2}$ increases.

$M_{1/2}$ (GeV c^{-2})		ATLAS	ACME	Combined
300	τ	32.9±2.1	32.0±5.9	32.4±2.0
	σ_{SUSY}	19.7±0.9	19.7±1.5	19.5±0.5
	β	17.2±38.7	-2.6±7.7	9.9±42.3
400	τ	28.1±2.6	27.7±8.2	33.8±4.1
	σ_{SUSY}	4.70±0.43	4.45±0.76	4.65±0.29
	β	52.2±17.9	1.5±2.9	44.9±20.1
500	τ	28.0±5.6	23.0±7.2	29.3±4.9
	σ_{SUSY}	1.51±0.24	1.80±0.59	1.50±0.16
	β	53.3±15.7	1.5±1.8	54.4±10.6
600	τ	27.8±13.3	22.5±11.0	30.1±3.4
	σ_{SUSY}	0.62±0.20	0.81±0.49	0.61±0.18
	β	55.8±8.8	1.1±0.7	58.0±12.8
700	τ	33.3±43.3	32.5±25.0	27.4±18.3
	σ_{SUSY}	0.36±0.27	0.52±0.25	0.23±0.07
	β	59.1±9.5	1.1±0.7	58.8±5.5
800	τ	141.8±94.8	58.2±42.4	65.5±55.3
	σ_{SUSY}	0.006±0.002	0.46±0.33	0.006±0.002
	β	61.3±4.0	1.1±0.7	60.6±5.8
900	τ	$1.84\times10^{3}\pm3.11\times10^{3}$	63.2±40.5	$1.01\times10^{3}\pm2.82\times10^{3}$
	σ_{SUSY}	0.003±0.003	0.44±0.47	0.002±0.002
	β	58.8±7.3	1.1±0.7	58.4±7.3

Table 6.4: The lifetime, SUSY cross-section and background rate fit resolutions of the three detector combinations for a lifetime of 30 days.

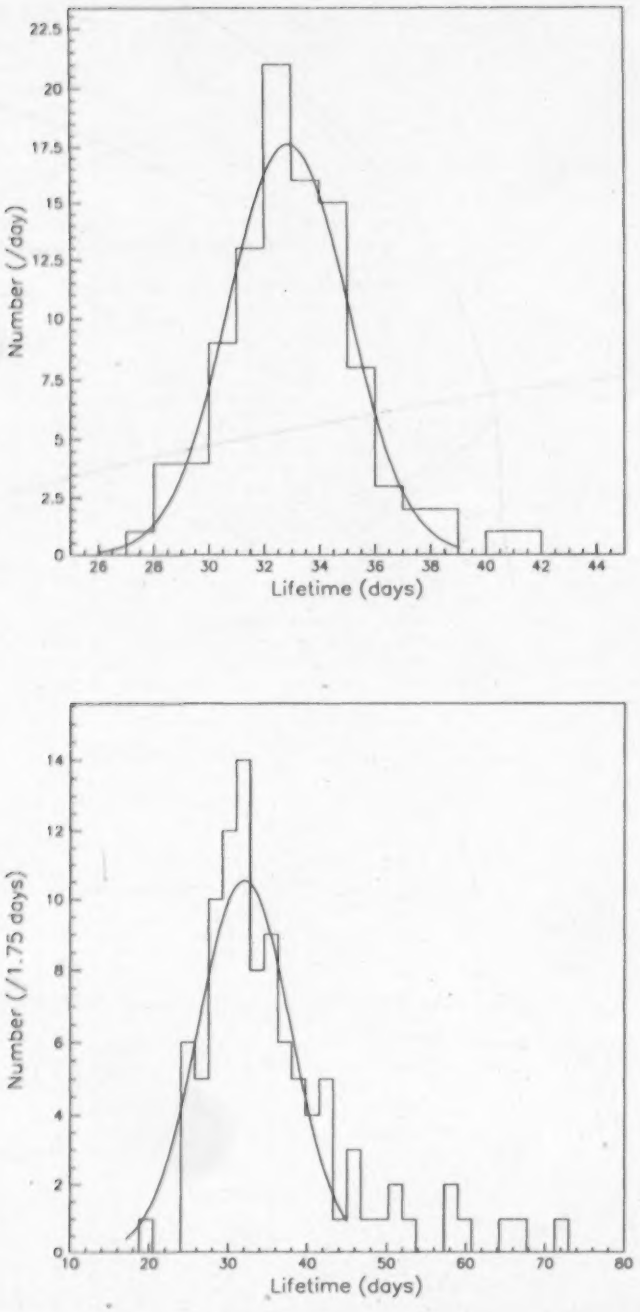

Figure 6.5: These histograms contain the lifetimes resulting from 100 fits using ATLAS (top) and ACME (bottom), where the spread in the lifetimes gives a measure of the lifetime fit resolution. The real lifetime is 30 days and the value of $M_{1/2}$ is 300 GeV c^{-2}.

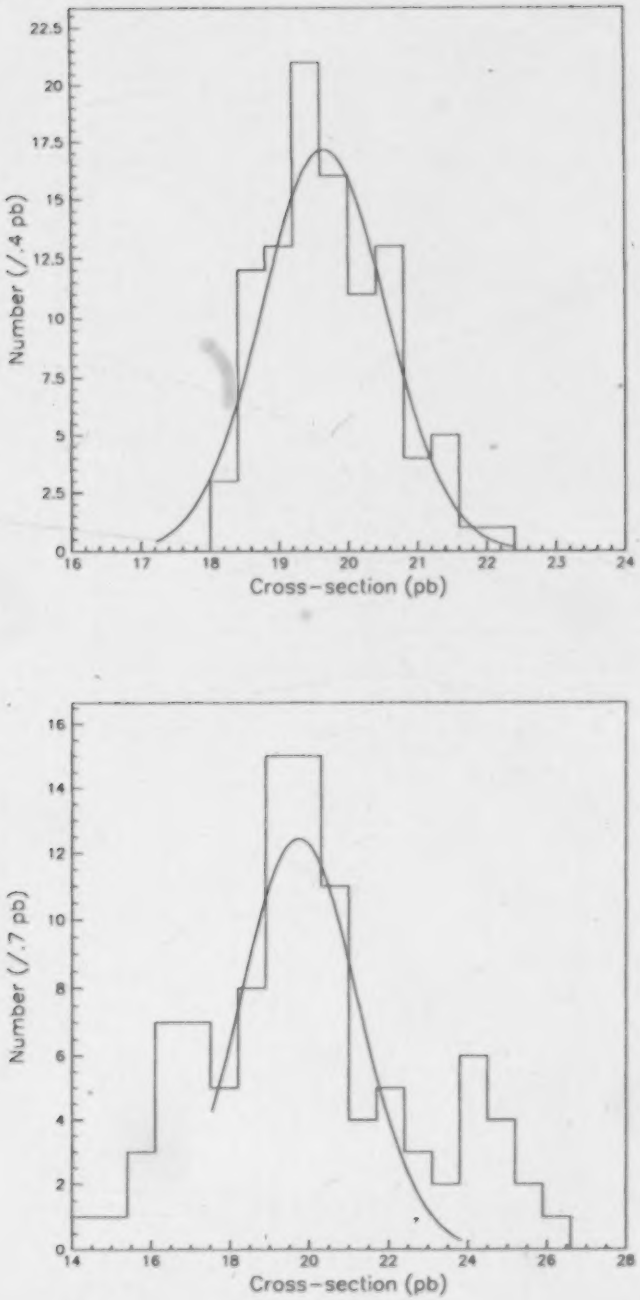

Figure 6.6: Theses histograms contain the cross-sections resulting from 100 fits using ATLAS (top) and ACME (bottom), where the spread in the cross-sections gives a measure of the cross-section fit resolution. The real lifetime is 30 days and the value of $M_{1/2}$ is 300 GeV c^{-2}.

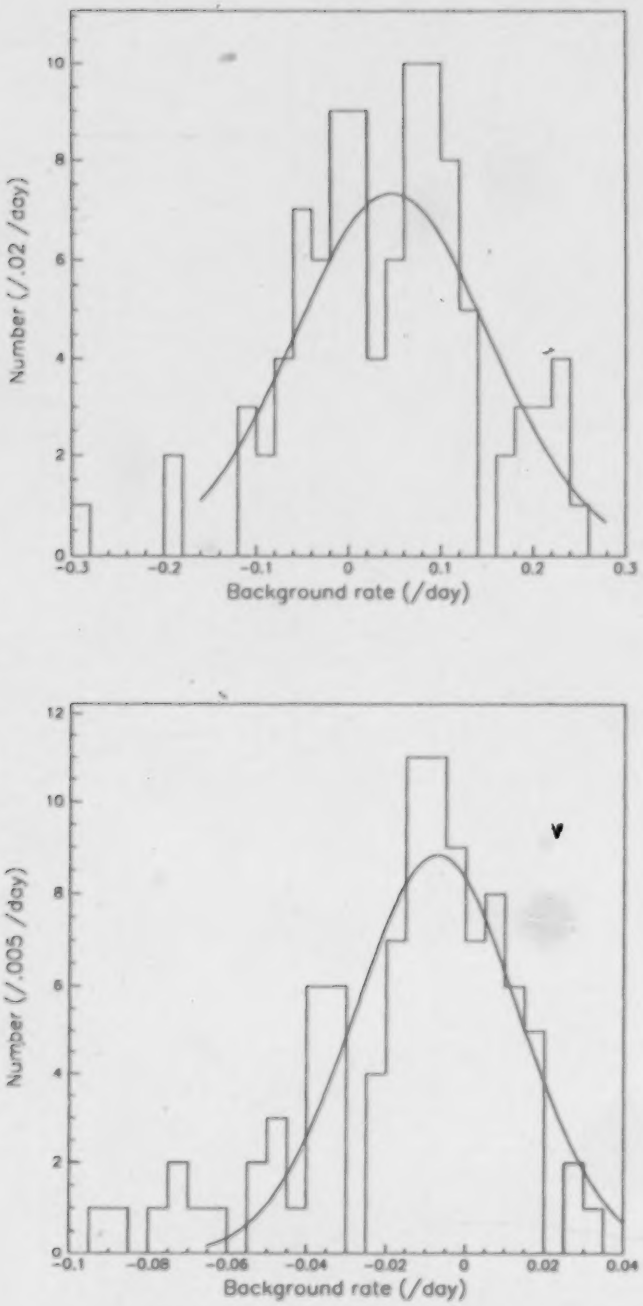

Figure 6.7: These histograms contain the background rates resulting from 100 fits using ATLAS (top) and ACME (bottom), where the spread in the background rates gives a measure of the cross-section fit resolution. The real lifetime is 30 days and the value of $M_{1/2}$ is 300 GeV c^{-2}.

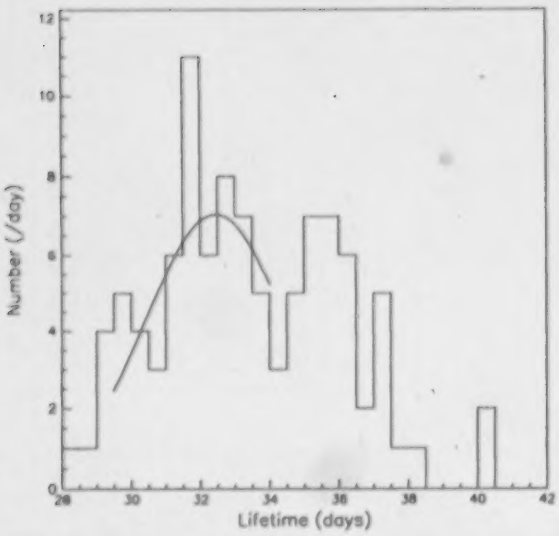

Figure 6.8: This histogram contains the lifetimes resulting from 100 fits using the combined ATLAS and ACME data for a lifetime of 30 days at $M_{1/2}$ equal to 300 GeV c^{-2}.

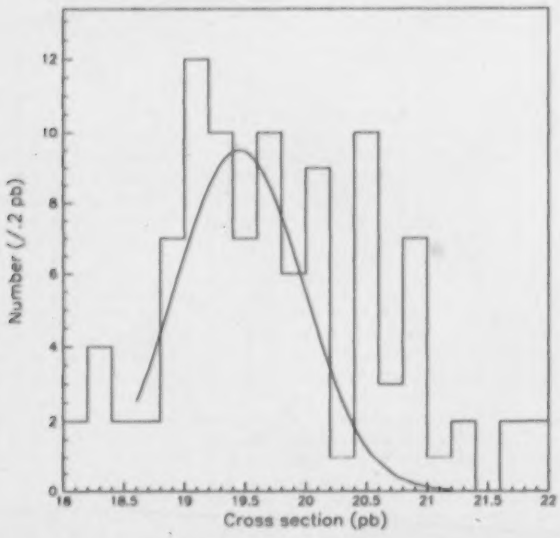

Figure 6.9: This histogram contains the cross-sections resulting from 100 fits using the combined ATLAS and ACME data for a lifetime of 30 days at $M_{1/2}$ equal to 300 GeV c^{-2}.

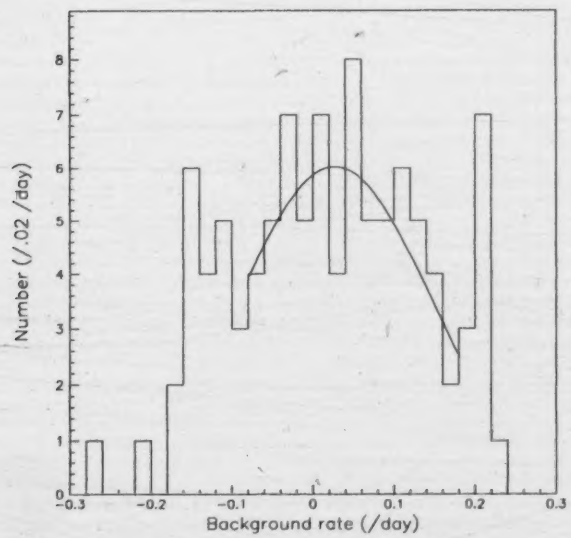

Figure 6.10: This histogram contains the background rates resulting from 100 fits using the combined ATLAS and ACME data for a lifetime of 30 days at $M_{1/2}$ equal to 300 GeV c^{-2}.

Finally, since it is apparent the ACME does not add a significant amount of additional resolution to the lifetime, cross-section and background rate fits, I look at the spread in theses values for ATLAS, alone, which table 6.5 shows, with table 6.6 showing the corresponding standard deviations in the spreads. Again, I performed the fits 100 times for each lifetime and $M_{1/2}$ parameter pair. From these tables, one can see that, as the value of $M_{1/2}$ increases, the accuracy in the values of the reconstructed lifetimes and cross-sections decreases and the accuracy of the reconstructed background rates improves. Again, this is because the small cross-sections at large values of $M_{1/2}$ cause the detectors to see mostly background events. Thus, in order to have the signal portion of the fit vanish (the $A(1 - e^{-Bt})$ in equation 6.10), one either requires the lifetime to become huge, or the cross-section to go to zero. As the tables show, the means of the lifetime distributions do become huge as the cross-sections become small. Consequently, one cannot expect to accurately reconstruct the stau lifetime at those model points, simply because the stau production cross-section is too low and neither ATLAS nor ACME can see the signal above the background rate.

Even though ATLAS does a better job at reconstructing the stau lifetime and SUSY cross-section, one can, nevertheless, justify the use of ACME with the arguments that follow. Generally, one schedules the beam shut down periods primarily for detector servicing, which could mean that neither the ATLAS detector nor the ATLAS trigger system will be available for use at those times. In this case, one could use ACME to perform this lifetime fit analysis, which would only result in a lower resolution fit. Also, one can notice from table 6.4 that, for very low cross-sections, ACME can do a better job than ATLAS at reconstructing the stau lifetime and SUSY cross-section. This is because the background to acceptance ratio for ACME is much lower than that ratio for ATLAS, implying that ACME could see a more significant number of events over background when there are very few events to be seen. Lastly, since ACME is a simple detector, it will likely be easier for one to understand its behavior than for one to understand the behavior of the ATLAS detector when running in a non-standard configuration.

$M_{1/2}$ (GeV c^{-2})	τ_{real}	7 days	30 days	90 days	150 days	365 days
300	τ	7.93	32.9	109.5	156.6	412.8
	σ_{SUSY}	21.2	19.7	22.3	20.3	16.7
	β	55.5	17.2	-221.9	13.1	-74.1
400	τ	7.58	28.1	107.7	264.6	412.9
	σ_{SUSY}	5.14	4.70	5.54	8.00	3.72
	β	59.5	52.2	-17.5	-208.8	75.6
500	τ	8.18	28.0	193.8	303.0	417.5
	σ_{SUSY}	1.55	1.51	1.35	2.83	1.25
	β	58.4	53.3	117.5	-51.1	82.9
600	τ	8.19	27.8	289.6	338.4	397.2
	σ_{SUSY}	0.423	0.624	0.527	0.330	0.205
	β	59.5	55.8	77.4	78.1	90.9
700	τ	7.63	33.3	192.4	1.26×10^{5}	2.72×10^{5}
	σ_{SUSY}	0.305	0.360	0.107	0.170	0.081
	β	61.0	59.1	71.2	73.4	69.7
800	τ	8.30	141.8	1.92×10^{4}	1.10×10^{5}	1.00×10^{5}
	σ_{SUSY}	0.043	0.006	0.016	0.033	0.038
	β	59.1	61.3	63.5	65.7	64.2
900	τ	6.68	1.84×10^{3}	4.51×10^{4}	1.09×10^{5}	1.65×10^{5}
	σ_{SUSY}	0.045	0.003	0.007	0.012	0.043
	β	57.7	58.8	64.2	63.5	60.2

Table 6.5: The lifetime, SUSY cross-section and background rate fit resolutions from ATLAS data. Notice that as $M_{1/2}$ becomes large, where the actual SUSY cross-section is low, it becomes more difficult to reconstruct the lifetimes and cross-sections, but easier to reconstruct the background rate. This is because, when the cross-section is so low, most of the data one collects will be background.

$M_{1/2}$ (GeV c^{-2})	τ_{real}	7 days	30 days	90 days	150 days	365 days
300	τ	0.52	2.1	17.9	11.6	42.9
	σ_{SUSY}	1.7	0.9	3.2	3.7	1.1
	β	5.1	38.7	362.1	75.2	198.6
400	τ	0.69	2.6	24.0	80.8	17.7
	σ_{SUSY}	1.02	0.43	1.10	0.70	0.97
	β	5.5	17.9	31.4	49.6	109.9
500	τ	2.85	5.6	101.4	91.6	110.4
	σ_{SUSY}	0.50	0.24	0.31	0.54	0.17
	β	4.7	15.7	36.9	28.8	57.7
600	τ	4.01	13.3	105.0	192.0	186.6
	σ_{SUSY}	0.217	0.197	0.224	0.120	0.030
	β	4.0	8.8	9.5	28.8	8.0
700	τ	10.18	43.3	192.2	0.76×10^{5}	2.34×10^{5}
	σ_{SUSY}	0.137	0.273	0.051	0.020	0.022
	β	2.6	9.5	6.9	9.1	6.9
800	τ	10.54	94.8	1.15×10^{4}	0.91×10^{5}	0.91×10^{5}
	σ_{SUSY}	0.069	0.002	0.005	0.010	0.021
	β	4.7	4.0	7.7	5.1	5.5
900	τ	9.59	3.11×10^{3}	4.58×10^{4}	0.82×10^{5}	2.10×10^{5}
	σ_{SUSY}	0.138	0.003	0.003	0.009	0.046
	β	4.7	7.3	7.3	3.3	4.7

Table 6.6: The error in the lifetime, SUSY cross-section and background rate fit resolutions from ATLAS data.

Chapter 7

Conclusion

Using simple models of the ATLAS and ACME detectors, I studied the sensitivity of these detectors to the decay of long-lived staus that become trapped either in ATLAS or in the ATLAS overburden or underburden. I found that both detectors are more sensitive to upward-going decay products than to downward-going decay products and, considering that the upward-going muon background rate, a result of neutrino interactions within the earth, is far smaller than the rate of downward-going cosmic ray muons, I chose to only look at the signal of upward-going decay products. I found that the sensitivity of ATLAS to decays of this sort is approximately ten times greater than the sensitivity of ACME to the decays, which is primarily due to the geometry of the detectors, where ATLAS covers a larger solid angle and has a larger effective area with respect to the decaying staus than does ACME.

Using the detectors, I was able to determine the stau lifetime, SUSY cross-section and upward-going background rate via fitting the number of stau decays each detector observes during the LHC beam shut-off period, where the only background is a result of the upward-going muons. I looked at two scenarios, where the first used ATLAS and ACME as separate detectors, combining the fit results from their respective data sets, and the second treated ATLAS and ACME as one effective detector, with only one set of data. I found that by treating ATLAS and ACME as one effective detector, one does not improve the lifetime fit over using ATLAS only. The fit enables one to reconstruct the stau lifetime, SUSY cross-section and background rate to within an av-

erage accuracy of up to 6.7%, 2.3% and 9.5% using only ACME, 6.3%, 1.0% and 2.1% using only ATLAS and 8.0%, 3.2% and 4.3% by combining the two detectors.

As such, I conclude that only ATLAS and the standard ATLAS cosmic ray trigger are necessary to reconstruct the stau lifetime, SUSY cross-section and upward-going muon background rate. Nevertheless, since ACME can still perform the fit, although not as accurately, it could prove to be valuable if ATLAS and the ATLAS trigger are not available when the beam is shut-off, since one schedules the beam shutdown periods primarily for detector servicing. Also, since the ratio of the background rate in ACME to its signal acceptance is lower than that ratio for ATLAS, ACME could be useful for determining the stau lifetime for very low SUSY cross-sections. Finally, as ACME is a simple detector, it should be easier for one to understand the signal and background that ACME sees than to understand the signal and background that ATLAS will see.

As a final note, I conclude that the lifetime fit is most accurate for lifetimes between 7 and 90 days and will require a SUSY cross-section greater than approximately 0.50 pb^{-1}.

Bibliography

[1] M. L. West. *Hesiod: Theogony, Works and Days.* New York: Oxford University Press, 1988.

[2] M. P. O. Morford and R. J: Lenardon. *Classical Mythology.* New York: Oxford University Press, 7 edition, 2003.

[3] ATLAS Collaboration. The ATLAS experiment at the CERN Large Hadron Collider. *ATL-COM-PHYS-2007-102*, 2007.

[4] S. Eidelman et al. Review of particle physics. *Phys. Lett.* ***B592***, page 1, 2004.

[5] J. Feng and B. Smith. Slepton trapping at the CERN Large Hadron Collider and the International Linear Collider. *Phys. Rev.* ***D71***, page 015004, 2005.

[6] J. Pinfold. Private communication. *ACME proposal*, 2006.

[7] S. Vigano and A. De Min. Detection methods for long lived particles at the LHC. *IFAE 2006*, pages 211–214, 2006.

[8] S. Tarem et al. Trigger and reconstruction for a heavy long lived charged particles with the ATLAS detector. *COM-PHYS-2007-096*, 2007.

[9] K. Hamaguchi et al. A study of late decaying charged particles at future colliders. *Phys. Rev.* ***D70***, 2004.

[10] K., Nojiri N. Hamaguchi and A. de Roeck. Prospects to study a long-lived charged next lightest supersymmetric particle at the LHC. *JHEP 046*, 2007.

[11] D. Griffiths. *Introduction to Elementary Particles.* John Wiley & Sons, Inc., Toronto, 1987.

[12] A. Barr. Studies of supersymmetry models for the ATLAS experiment at the Large Hadron Collider. *CERN-THESIS-2004-002*, Phd Thesis, University of Cambridge, November 2002.

[13] I. Aitchison and A. Hey. *Gauge Theories in Particle Physics Volume II: QCD and Electroweak Theory.* Institute of Physics Publishing, Philadelphia, 3 edition, 2004.

[14] I. Aitchison and A. Hey. *Gauge Theories in Particle Physics Volume I: From Relativistic Quantum Mechanics to QED.* Institute of Physics Publishing, Philadelphia, 3 edition, 2004.

[15] R. Moore. *Physics 590 Lecture Notes.* University of Alberta, Winter 2006.

[16] R. Cahn. The eighteen arbitrary parameters of the standard model in your everyday life. *Rev. Mod. Phys. 68*, pages 951–959, 1996.

[17] J. Gunion. A simplified summary of supersymmetry. *arXiv:hep-ph/9704349v1*, 1997.

[18] S. Martin. A supersymmetry primer. *arXiv:hep-ph/9709356v4*, 2006.

[19] J. Feng. Probing gravitational interactions of elementary particles. *Int. Jour. Mod. Phys.* ***D13***, pages 2355–2359, 2004.

[20] J. Feng. Supergravity with a gravitino lightest supersymmetric particle. *Phys. Rev.* ***D70***, page 075019, 2004.

[21] M. Fairbairn et al. Stable massive particles at colliders. *Phys. Rep. 438*, pages 1–63, 2007.

[22] A. Habig. Neutrino-induced upward-going muons in super-kamiokande. *arXiv:hep-ex/9903047 v2*, 1999.

[23] S. Hatakeyama et al. Measurement of the flux and zenith-angle distribution of upward through-going muons in Kamiokande II + III. *Phys. Rev. Lett. 81*, page 2016, 1998.

[24] T. Toshito. Super-Kamiokande atmospheric neutrino results. *arXiv:hep-ex/0105023 v1*, 2001.

[25] C. Zhang and Y. Ma. Detectability of upgoing sleptons. *arXiv:hep-ph/0410353v4*, 2004.

[26] Z., Nakagawa N. Maki and S. Sakata. Remarks on the unified model of elementary particles. *Prog. Theor. Phys. 28*, page 870, 1962.

[27] V. Gribov and B. Pontecorvo. Neutrino astronomy and lepton charge. *Phys. Lett.* ***B28***, page 493, 1969.

[28] M. Alberico and S. Bilenky. Neutrino oscillations, masses and mixing. *Phys. Part. Nucl. 35*, page 297, 2004.

[29] O. Brüning (ed.) et al. LHC design report v.1: the LHC main ring. *CERN-2004-003-V-1*, 2004.

[30] O. Brüning (ed.) et al. LHC design report v.2: the LHC infrastructure and general services. *CERN-2004-003-V-2*, 2004.

[31] M. Benedikt (ed.) et al. LHC design report v.3: the LHC injector chain. *CERN-2004-003-V-3*, 2004.

[32] The LEP Injector Study Group. LEP design report v.1: The LEP injector chain. *CERN-LEP-TH-83-29*, 1983.

[33] LEP design report v.2: The LEP main ring. *CERN-LEP-84-01*, 1984.

[34] C. Wyss (ed.). LEP design report v.3: LEP2. *CERN-AC-96-01-LEP-2*, 1996.

[35] CERN. The accelerator complex. *http://public/web.cern.ch/Public/en/Research/AccelComplex-en.html*, 2007.

[36] Communication Group. CERN FAQ - LHC the guide. *CERN-Brochure-2006-003-Eng*, 2006.

[37] CERN Publications. Discovery Monday - the power to attract: Magnets that make heads turn. *The Bulletin*, 23, 2004.

[38] D. Acosta (ed.). CMS physics technical design report, v.1: Detector performance and software. *CERN-LHCC-2006-001*, 2006.

[39] A. De Roeck. CMS techical design report, volume ii: Physics performance. *J. Phys. G: Nucl. Part. Phys. 34*, 2007.

[40] ALICE Collaboration. ALICE: Technical proposal for A Large Ion Collider Experiment at the CERN LHC. *CERN-LHCC-95-71*, 1995.

[41] LHCb Collaboration. LHCb reoptimized detector design and performance: Technical design report. *CERN-LHCC-2003-030*, 2003.

[42] T. Lari. The ATLAS and CMS experiments. *COM-GEN-2007-002*, 2007.

[43] R. Bailey. What LHC operation will look like. *Chamonix XIII*, pages 219–221, 2004.

[44] R. Bailey. Scheduling LHC operation. *Chamonix XIV*, pages 5–7, 2005.

[45] ATLAS Collaboration. ATLAS technical proposal for a general-purpose pp experiment at the Large Hadron Collider at CERN. *CERN/LHCC/94-43*, 1994.

[46] S., Bleicher M. Hossenfelder and H. Stocker. Signatures of large extra dimensions. *arXiv:hep-ph/0405031v1*, 2004.

[47] ATLAS Inner Detector Community. ATLAS inner detector technical design report. *CERN/LHCC/97-16*, 1, 1997.

[48] ATLAS Inner Detector Community. ATLAS inner detector technical design report. *CERN/LHCC/97-17*, 2, 1997.

[49] ATLAS Collaboration. Calorimeter performance technical design report. *CERN/LHCC/96-40*, 1997.

[50] ATLAS LARG Unit. Liquid argon technical design report. *CERN/LHCC/96-41*, 1996.

[51] ATLAS/Tile Calorimeter Collaboration. Tile calorimeter technical design report. *CERN/LHCC/96-42*, 1996.

[52] ATLAS Muon Collaboration. *Muon Spectrometer Technical Design Report.* 1997.

[53] ATLAS Magnet Group. ATLAS magnet system. *http://atlas-magnet.web.cern.ch/atlas-magnet/*, 17 November 2007.

[54] ATLAS Magnet Project Collaboration. ATLAS magnet system technical design report. *CERN/LHCC/97-18*, 1997.

[55] ATLAS Magnet Project Collaboration. ATLAS central solenoid technical design report. *CERN/LHCC/97-21*, 1997.

[56] ATLAS Magnet Project Collaboration. ATLAS barrel toroid technical design report. *CERN/LHCC/97-19*, 1997.

[57] ATLAS Magnet Project Collaboration. ATLAS end-cap toroids technical design report. *CERN/LHCC/97-20*, 1997.

[58] L. Chevalier. ATLAS magnetic field. *http://atlas.web.cern.ch/Atlas/GROUPS/MUON/magfield/mag_page1.html*, 2007.

[59] ATLAS Level-1 Trigger Group. Level-1 trigger technical design report. *CERN/LHCC/98-14*, 1998.

[60] ATLAS HLT/DAQ/DCS Group. *ATLAS High-Level Trigger, Data Acquisition and Controls Technical Design Report.* 2003.

[61] ATLAS L1Calo Group. ATLAS level-1 calorimeter trigger algorithms. *ATL-DAQ-2004-011*, 1.0, 2004.

[62] K. Cranmer and A. Mincer. TAPMMissingEt. *https://twiki.cern.ch/twiki/bin/view/Atlas/TAPMMissingEt*, 20 May 2007.

[63] A. Hamilton. EtMiss. *https://twiki.cern.ch/twiki/bin/view/Atlas/EtMiss*, 21 May 2007.

[64] A. Krasznahorkay. LVL1 RPC trigger simulation documentation. *https://twiki.cern.ch/twiki/bin/view/Atlas/MuonTriggerDocLvl1Rpc*, 12 February 2007.

[65] S. Armstrong et al. A new implementation of the region-of-interest strategy for the ATLAS second level trigger. *Computing in High Energy and Nuclear Physics, La Jolla, California*, 24-28 March 2003.

[66] R. Blair et al. The ATLAS high level trigger region of interest builder. *2007*, COM-DAQ-2007-042.

[67] M. Boonekamp et al. Cosmic ray, beam-halo and beam-gas rate studies for ALTAS commissioning. *ATL-GEN-2004-001*, 2004.

[68] N. Kayana. LVL1 TGC trigger simulation documentation. *https://twiki.cern.ch/twiki/bin/view/Atlas/MuonTriggerDocLvl1Tgc*, 6 July 2007.

[69] T. Kohno. LVL2 cosmic muon algorithm documentation. *https://twiki.cern.ch/twiki/bin/view/Atlas/MuonTriggerDocLvl2Cosmic*, 8 July 2007.

[70] GEANT detector description and simulation tool. *CERN Program Library Long Writeup W5013*, 1994.

[71] M. Nessi and G. Poulard. DICE = Calorimetry - Material Caracteristics. *http://atlas.web.cern.ch/Atlas/GROUPS/ SOFTWARE/DOCUMENTS/DICE_320/geom_mat.html, 2007*, 1998.

[72] M. Berger et al. Stopping-power and range tables for electrons, protons, and helium ions. *physics.nist.gov/cgi-bin/Star/compos.pl?matno=112*, 2005.

[73] The FLUKA Team. Online FLUKA manual. *pcfluka.mi.infn.it/ manual/sect/s101/text.html*, 2006.3b.7, 2007.

[74] Richard Soluk. GEANT3 ATLAS overburden and cavern system model. 2002.

[75] Jonathan Braden. GEANT3 ATLAS underburden model. 2005.

[76] PAW: Physics Analysis Workstation user's guide. *CERN Program Library Long Writeup Q121*, 1999.

[77] G. Corcella et al. Herwig 6.5. *JHEP 0101 (2001) 010 [hep-ph/0011363]; hep-ph/0210213*, 2002.

[78] S. Moretti et al. Implementation of supersymmetric processes in the HERWIG event generator. *JHEP 0204 (2002) 028 [hep-ph/0204123]*, 2002.

[79] H. Baer et al. ISAJET: A Monte Carlo event generator for pp, $\bar{p}p$, and e^+e^- reactions. *arXiv:hep-ph/0312045v1*, 2003.

[80] H. Baer et al. Simulating SUSY with ISAJET/ISASUSY 1.0. *Proceedings of the Workshop on Physics at Current Accelerators and the Supercolliders, Argonne*, ANL-HEP-CP-93-92, C93/06/02, June 1993.

[81] B. Webber et al. ISAWIG. *http://www.hep.phy.cam.ac.uk/~richardn/ HERWIG/ISAWIG/*, 2002.

[82] N. Ellis and T. Pauly. Private communication. 24 February 2007.

[83] T. Kohno. Private communication. 20 September 2007.

[84] J. Braden. Lifetime determination of heavy charged particles in SUSY models with a gravitino LSP. *University of Alberta*, 2005.

Appendix A

ACME, an extension of ATLAS' reach

ACME (ATLAS Cosmic Muon and Exotics detector) is a proposal for a fast scintillating cosmic ray multi-muon detector for use with ATLAS [6]. The main use of this detector will be to look for cosmic ray muon bundles that pass through the ATLAS overburden and not through the main access shafts PX14 and PX16. One could also, potentially, use it as a vetoing device for cosmic ray showers, where one can consider a bundle of particles passing through both ACME and ATLAS to be cosmic rays. One should note that it is, in principle, possible to include a detector of this sort in the ATLAS LVL1 trigger. It will require provisions in NIM and must run on electronics that work according to the LHC bunch spacing clock with 25 ns pulses [82]. Since ACME will use scintillating tile technology, it should be possible to meet both of these criteria.

I include a model for ACME in the GEANT 3 simulation. It consists of two planes of scintillator, where each is a square of side-length 10 m and thickness

Figure A.1: The ACME detector model consists of two parallel planes 30 cm apart. The top plane is segmented into ten strips in the η direction and the bottom plane is segmented into ten strips in the ϕ direction.

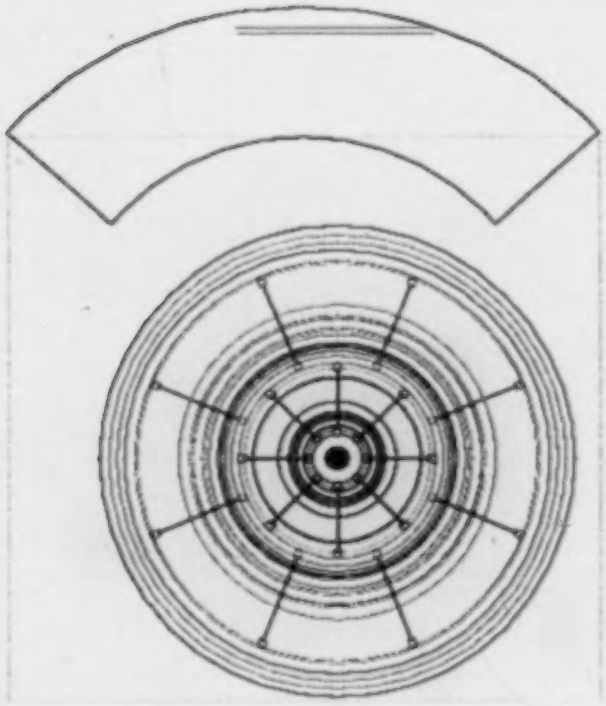

Figure A.2: The ACME model lies in the roof section of the ATLAS cavern UX15 directly above the interaction point.

2.54 cm. I segment each plane into ten 1 m wide strips pointing along η in the upper plane and along ϕ in the lower plane. A distance of 30 cm separates the bottom face of the upper plane from the top face of the lower plane. Figure A.1 shows the two planes in relation to one another.

ACME lies 18.664 m above the floor of the ATLAS main cavern, UX15, with its centre directly above the interaction point. Figure A.2 shows the position of ACME relative to the cavern. Also, one can see where ACME lies in relation to the entire ATLAS cavern system in figures 4.15 and 4.16.

Appendix B

The ACME solid angle

An object's solid angle, given by

$$\Omega = -\int\int d(\cos\Theta)d\phi, \tag{B.1}$$

is the angle that the object subtends at a point, where Θ is the zenith angle and ϕ is the azimuth. It is proportional to the surface area of the object's projection onto a sphere's surface, where, if one chooses the proportionality constant to be one, then the total solid angle becomes 4π sr [1]. In this way, the solid angle relates to the surface area of a sphere in the same way that a regular angle (in units of radians) relates to the circumference of a circle. The solid angle of an object is useful in that it gives a measure of the physical cross-section of an object with respect to an observer's line of sight.

To determine the solid angle of ACME with respect to the zenith angle [2], let us begin by finding the solid angle of a square. Begin with an observer standing at a distance R from the centre of a square of sidelength $2x_o$, where his line of sight is orthogonal to the square's surface. Figure B.1 shows the angles Θ and ϕ, where the length of line r changes depending on ϕ, which then affects the angle Θ. One can represent the angles Θ and ϕ as

$$\cos\Theta \in \left[1, \frac{R}{\sqrt{R^2+r^2}}\right] \text{ and } \phi = \arccos\left(\frac{x_o}{r}\right),\ r \in [x_o, \sqrt{2}x_o], \tag{B.2}$$

where we will divide the integral over $d\phi$ into eight symmetric sections of equal area, with $\phi \in [0, \frac{\pi}{4}]$ for each.

[1] This is the SI unit *steradian*.

[2] Yes, I am referring to two different zenith angles. The first, Θ, is internal to the solid

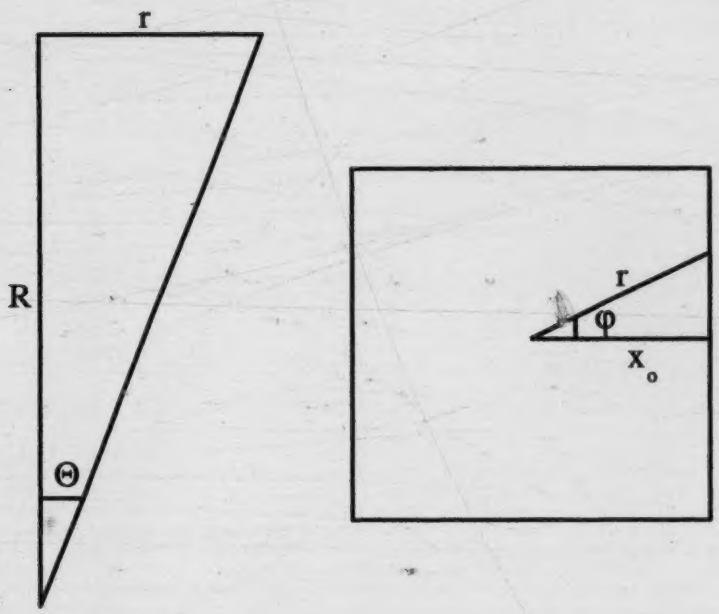

Figure B.1: The setup for the solid angle determination of a square.

This implies that

$$d\phi = \frac{x_o dr}{r\sqrt{r^2 - x_o^2}}, \tag{B.3}$$

which gives

$$\begin{aligned}
\Omega &= -\int\int d(\cos\Theta)d\phi \\
&= -8\int_{x_o}^{\sqrt{2}x_o} \frac{x_o dr}{r\sqrt{r^2 - x_o^2}} \int_1^{\frac{R}{\sqrt{R^2+r^2}}} d(\cos\Theta) \\
&= 8\int_{x_o}^{\sqrt{2}x_o} \frac{x_o}{r\sqrt{r^2 - x_o^2}} \left(1 - \frac{R}{\sqrt{R^2+r^2}}\right) dr
\end{aligned} \tag{B.4}$$

Now, we make the clever substitution

$$\begin{aligned}
z &= \sqrt{r^2 - x_o^2} \\
\Rightarrow \frac{dz}{r} &= \frac{dr}{\sqrt{r^2 - x_o^2}},
\end{aligned} \tag{B.5}$$

angle integral, where we integrate over it. The second, θ, is the zenith angle of the observer with respect to ACME, where this remains a parameter in our final solid angle determination.

which brings us to

$$\begin{aligned}\Omega &= 8\int_0^{x_o} \frac{x_o}{z^2+x_o^2}\left(1-\frac{R}{\sqrt{z^2+x_o^2+R^2}}\right)dz \\ &= 8\left(\arctan\left(\frac{z}{x_o}\right)-\arctan\left(\frac{Rz}{x_o\sqrt{z^2+x_o^2+R^2}}\right)\right)_0^{x_o}. \qquad \text{(B.6)}\end{aligned}$$

Finally, this leads to

$$\Omega = 2\pi - 8\arctan\left(\frac{R}{\sqrt{2x_o^2+R^2}}\right). \qquad \text{(B.7)}$$

To check this, note that

$$\lim_{x_o\to 0}\Omega = 2\pi - 8\arctan(1) = 0, \qquad \text{(B.8)}$$

meaning that one does not see any solid angle (since there is no square!). Also, note that

$$\lim_{x_o\to\infty}\Omega = 2\pi - 8\arctan(0) = 2\pi. \qquad \text{(B.9)}$$

So, a wall of infinite size will cover exactly half of the total solid angle of 4π. Finally,

$$\lim_{x_o\to R}\Omega = 2\pi - 8\arctan\left(\frac{R}{\sqrt{3}R}\right) = \frac{2\pi}{3}, \qquad \text{(B.10)}$$

noting that this is one sixth of the total solid angle of 4π. Thus, if one stands at the centre of a cube, then then cube will cover the total solid angle, with each of the six faces contributing one sixth of the solid angle.

Now, if we generalize the shape of the square to that of a rectangle with a half-length of x_o and a half-height of y_o, then we will end up with a situation of the type that figure B.2 displays. Again, we split the rectangle into eight regions, but now, there exist two regions over which we must integrate, multiplying the result of each by four and adding them together to obtain our final solid angle. These regions are shown as either shaded or unshaded in figure B.2.

For these regions, the integral is the same as that for a square, where one now writes the limits on r as

$$\begin{aligned} r &\in [x_o, \sqrt{x_o^2+y_o^2}] \\ r &\in [\sqrt{x_o^2+y_o^2}, y_o] \end{aligned} \qquad \text{(B.11)}$$

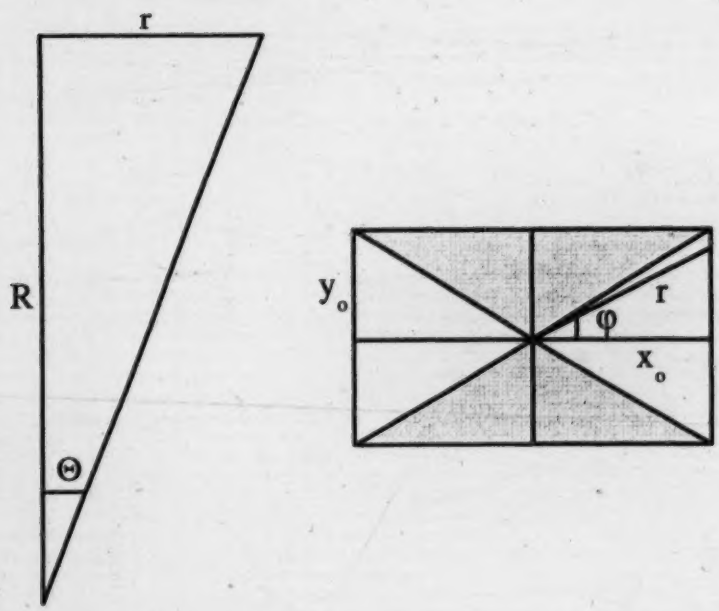

Figure B.2: The setup for the solid angle determination of a rectangle. The shaded regions each contribute the same value to the solid angle, which differs from the contribution of the unshaded regions.

for the unshaded and shaded regions, respectively. Using these limits in equation B.4 and making the same substitution as that in equation B.5 leads to the solid angle contribution of the unshaded and shaded regions, respectively, being

$$\begin{aligned} \Omega_u &= \arctan\left(\frac{y_o}{x_o}\right) - \arctan\left(\frac{Ry_o}{x_o\sqrt{x_o^2+y_o^2+R^2}}\right) \\ \Omega_s &= \arctan\left(\frac{x_o}{y_o}\right) - \arctan\left(\frac{Rx_o}{y_o\sqrt{x_o^2+y_o^2+R^2}}\right), \end{aligned} \tag{B.12}$$

where, again, the observer is at an orthogonal distance R from the centre of the rectangle. As a result, the total solid angle for a rectangle becomes

$$\Omega = 4(\Omega_u + \Omega_s). \tag{B.13}$$

Note that if we let $x_o = y_o$, which is the case for a square, then the solid

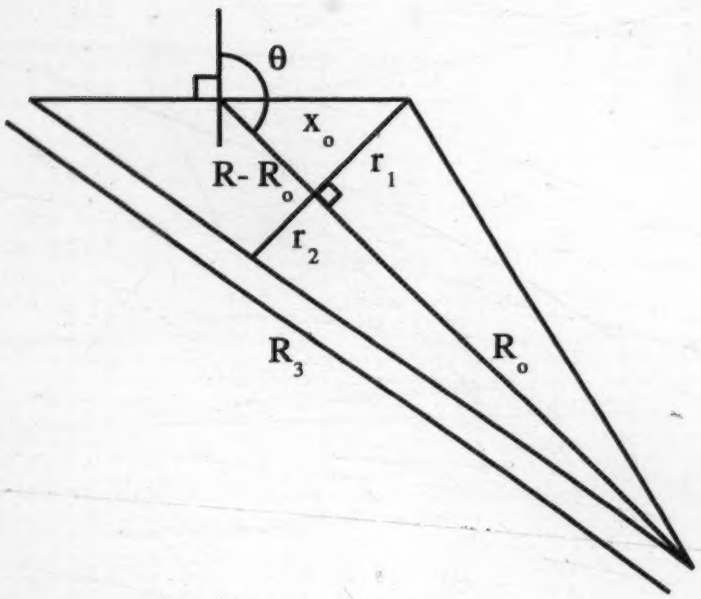

Figure B.3: The effective area the observer sees will depend on the zenith angle θ.

angle becomes

$$\lim_{y_o \to x_o} \Omega = 4\left(\frac{\pi}{2} - 2\arctan\left(\frac{R}{\sqrt{2x_o^2 + R^2}}\right)\right)$$
$$= 2\pi - 8\arctan\left(\frac{R}{\sqrt{2x_o^2 + R^2}}\right), \qquad \text{(B.14)}$$

the solid angle of a square.

Now, using these results, let us find the solid angle of a square as a function of zenith angle [3]. Figures B.3 and B.4 display the new situation, where the observer resides at a distance R from the centre of a square of side-length $2x_o$ at a zenith angle θ, where θ equal to zero corresponds to pointing straight up. It is our goal to find the solid angle of the square in terms of these three parameters only.

From the point of view of the observer, the square now looks like a trapezoid, where we let the edge of the trapezoid closest to the observer have a

[3]This is the external zenith angle, to which I referred earlier.

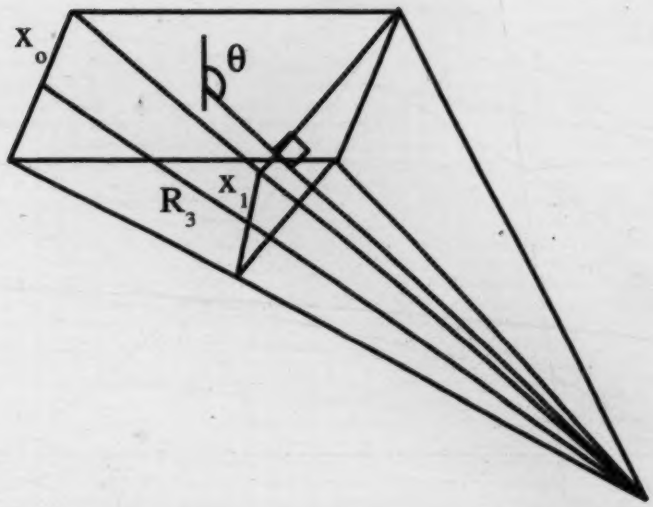

Figure B.4: This figure demonstrates how the shape of the square the observer sees will change as a function of the zenith angle θ.

half-length of x_o and the other have a half-length of x_1, where x_1 is less than x_o. Also, the intersection point of the oberver's line of sight with the trapezoid will, as figures B.3 and B.5 show, not be at the half-width of the trapezoid; rather, it will lie a distance of r_1 from the close edge and a distance of r_2 from the far edge, where r_2 is less than r_1, always, and we call the distance from this intersection point to the trapezoid edge x_2. Let us call the distance from the observer to this intersection point R_o. In terms of our three measureable parameters, we have

$$\begin{aligned} r_1 &= x_o \sin(\theta - \frac{\pi}{2}) = -x_o \cos\theta \\ R_o &= R - x_o \cos(\theta - \frac{\pi}{2}) = R - x_o \sin\theta \\ r_2 &= R_o \left(\frac{r_1}{R + x_o \sin\theta} \right) \\ &= -x_o \cos\theta \left(\frac{R - x_o \sin\theta}{R + x_o \sin\theta} \right). \end{aligned} \tag{B.15}$$

Also, calling the distance from the observer to the far edge of the trapezoid

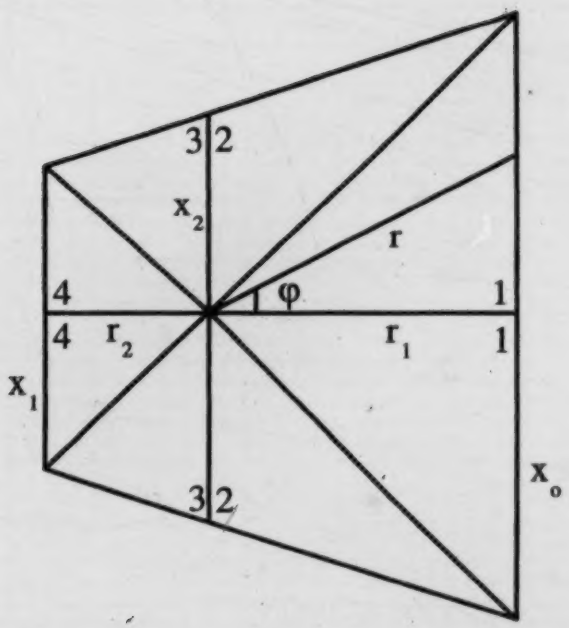

Figure B.5: The setup for the determination of the solid angle of a trapezoid. Sections with the same number will contribute the same value to the solid angle.

R_3, we have

$$\frac{\sqrt{R_o^2 + r_2^2}}{x_1} = \frac{R_3}{x_o} = \frac{\sqrt{R^2 + x_o^2 + 2Rx_o \sin\theta}}{x_o}, \tag{B.16}$$

which, using B.15, leads to

$$x_1 = x_o \left(\frac{R - x_o \sin\theta}{R + x_o \sin\theta} \right). \tag{B.17}$$

Finally, for the value of x_2, we have

$$\begin{aligned} \frac{r_1 + r_2}{x_o - x_1} &= \frac{r_2}{x_2 - x_1} \\ \Rightarrow x_2 &= x_1 + r_2 \left(\frac{x_o - x_1}{r_1 + r_2} \right) \\ \Rightarrow x_2 &= \frac{x_o}{R}(R - x_o \sin\theta). \end{aligned} \tag{B.18}$$

Now, for the trapezoid, we have four regions over which we must integrate for the solid angle, where doubling the sum of these four solid angles will give us the total solid angle of the trapezoid, because of the trapezoidal symmetry. Figure B.5 labels these regions as 1, 2, 3 and 4.

We have, essentially, already determined the solid angle of regions 1 and 4 in working out the solid angle of the rectangle in equations B.12 and B.13, above. If we take the limits on r to be

$$r \in [r_1, \sqrt{r_1^2 + x_o^2}], \tag{B.19}$$

in place of those in equation B.11, then, using equation B.12, we find that the solid angle of region 1 is

$$\Omega_1 = \arctan\left(\frac{x_o}{r_1}\right) - \arctan\left(\frac{R_o x_o}{r_1\sqrt{x_o^2 + r_1^2 + R_o^2}}\right). \tag{B.20}$$

The solid angle of region 4 will be the same as that of region 1, where we take $x_o \rightarrow x_1$ and $r_1 \rightarrow r_2$, giving

$$\Omega_4 = \arctan\left(\frac{x_1}{r_2}\right) - \arctan\left(\frac{R_o x_1}{r_2\sqrt{x_1^2 + r_2^2 + R_o^2}}\right). \tag{B.21}$$

Region 2 is different than both region 1 and region 4, because in this region $r = \sqrt{x^2 + y^2}$, where both x and y vary, unlike in regions 1 and 4, where x_o and x_1 are constant in the definition of r. As a result, one uses the fact that

$$y = \left(\frac{x_o - x_2}{r_1}\right) x + x_2 \ , \ x \in [r_1, 0] \tag{B.22}$$

to define

$$\begin{aligned} \tan\phi &= \frac{y}{x} \\ &= \frac{x_o - x_2}{r_1} + \frac{x_2}{x} \\ \Rightarrow \quad d\phi &= \frac{-x_2 dx}{x^2\left(1 + \frac{(x_o - x_2)^2}{r_1^2}\right) + 2x_2\left(\frac{x_o - x_2}{r_1}\right)x + x_2^2} \\ &= \frac{-x_2 dx}{r^2}. \end{aligned} \tag{B.23}$$

Now, using equations B.2 and B.4 to find the integral over Θ [4], the solid angle of region 2 becomes

$$\Omega_2 = -\int_{r_1}^{0} \frac{x_2 dx}{r^2}\left(1 - \frac{R_o}{\sqrt{R_o^2 + r^2}}\right). \tag{B.24}$$

[4] This is the zenith angle internal to the integral, which one should not confuse with θ.

Notice, however, that

$$\begin{aligned} rdr &= \frac{r_1^2+(x_o-x_2)^2}{r_1^2}\left(x+\frac{x_2r_1(x_o-x_2)}{r_1^2+(x_o-x_2)^2}\right)dx \\ &= \frac{r_1^2+(x_o-x_2)^2}{r_1^2}\sqrt{r^2-\frac{x_2^2r_1^2}{r_1^2+(x_o-x_2)^2}}\frac{r_1dx}{\sqrt{r_1^2+(x_o-x_2)^2}} \\ \Rightarrow \quad dx &= \frac{r_1}{\sqrt{r_1^2+(x_o-x_2)^2}}\frac{rdr}{\sqrt{r^2-\frac{x_2^2r_1^2}{r_1^2+(x_o-x_2)^2}}}, \end{aligned} \tag{B.25}$$

after completing the square for r^2 to obtain the second line. As a result, the solid angle integral becomes

$$\begin{aligned} \Omega_2 &= \int_{x_2}^{\sqrt{r_1^2+x_o^2}} \frac{bdr}{r\sqrt{r^2-b^2}}\left(1-\frac{R_o}{\sqrt{R_o^2+r^2}}\right) \\ &\quad \text{where } b=\frac{x_2r_1}{\sqrt{r_1^2+(x_o-x_2)^2}} \\ &= \int_{\sqrt{x_2^2-b^2}}^{\sqrt{r_1^2+x_o^2-b^2}} \frac{bdz}{z^2+b^2}\left(1-\frac{R_o}{\sqrt{z^2+R_o^2+b^2}}\right) \\ &= \left(\arctan\left(\frac{z}{b}\right)-\arctan\left(\frac{R_oz}{b\sqrt{z^2+R_o^2+b^2}}\right)\right)_{\sqrt{x_2^2-b^2}}^{\sqrt{r_1^2+x_o^2-b^2}}, \end{aligned} \tag{B.26}$$

using the same substitution as that in equation B.5. Finally, we have

$$\begin{aligned} \Omega_2 = \arctan\left(\frac{r_1^2+x_o^2-x_ox_2}{r_1x_2}\right)-\arctan\left(\frac{x_o-x_2}{r_1}\right)- \\ \arctan\left(\frac{R_o(r_1^2+x_o^2-x_ox_2)}{r_1x_2\sqrt{r_1^2+x_o^2+R_o^2}}\right)+\arctan\left(\frac{R_o(x_o-x_2)}{r_1\sqrt{x_2^2+R_o^2}}\right). \end{aligned} \tag{B.27}$$

Now, notice that the solid angle for region 3 will be the same as that for region 2, where we let $x_o \to x_1$ and $r_1 \to r_2$. This substitution will result in terms containing $x_1 - x_2$, which is negative. So, in essence, we will get an answer that is the negative of the result for region 2. This is because the two regions are not exactly similar, where, in region 2, the tall end of the trapezoid is farther from the intersection point and in region 3, the tall end is closer to the intersection point. This results in a reversal of the contributions from each

of the four terms in equation B.27. As such, the solid angle of region 3 is

$$\Omega_3 = \arctan\left(\frac{r_2^2 + x_1^2 - x_1 x_2}{r_2 x_2}\right) - \arctan\left(\frac{x_1 - x_2}{r_2}\right) - \arctan\left(\frac{R_o(r_2^2 + x_1^2 - x_1 x_2)}{r_2 x_2 \sqrt{r_2^2 + x_1^2 + R_o^2}}\right) + \arctan\left(\frac{R_o(x_1 - x_2)}{r_2\sqrt{x_2^2 + R_o^2}}\right). \quad \text{(B.28)}$$

Finally, we can write the total solid angle of the trapezoid as

$$\Omega = 2(\Omega_1 + \Omega_2 + \Omega_3 + \Omega_4), \quad \text{(B.29)}$$

where one can show, using equations B.15, B.16, B.17 and B.18, that

$$\lim_{\theta \to 0} \Omega = 2\pi - 8 \arctan\left(\frac{R}{\sqrt{2x_o^2 + R^2}}\right); \quad \text{(B.30)}$$

thus, our result satisfactorily reduces to the case of an observer whose line of sight is perpendicular to the square's surface.

As a final note, one should recognise that the effective area that ACME covers as a function of zenith angle becomes $(r_1 + r_2)(x_o + x_1)$, which is the area of the trapezoid.

Appendix C

Analytic number of remaining staus

This appendix shows the derivation of the analytic solution of the number of staus remaining at the end of each LHC operational period i, using the system of iterative equations in equations 6.5 as a starting point.

Beginning with equation 6.5, which, as a reminder, is

$$\begin{aligned} N^o_{1,1} &= 0 \\ N^o_{1,j} &= N^f_{8,j-1}e^{-t_{sd}/\tau},\ j \geq 2 \\ N^o_{i,j} &= N^f_{i-1,j}e^{-t_{off}/\tau},\ i \in [2,8] \\ N^f_{i,j} &= N^o_{i,j}e^{-t_{on}/\tau} + R_j\tau(1-e^{-t_{on}/\tau}), \end{aligned}$$

one obtains the solution for $N^f_{i,j}$ as

$$\begin{aligned} N^f_{i,j} &= N^f_{i-1,j}e^{-(t_{on}+t_{off})/\tau} + R_j\tau(1-e^{-t_{on}/\tau}) \\ &= N^o_{i-1,j}e^{-t_{on}/\tau}e^{-(t_{on}+t_{off})/\tau} + R_j\tau(1-e^{-t_{on}/\tau})(1+e^{-(t_{on}+t_{off})/\tau}) \\ &= N^f_{i-2,j}e^{-2(t_{on}+t_{off})/\tau} + R_j\tau(1-e^{-t_{on}/\tau})(1+e^{-(t_{on}+t_{off})/\tau}) \\ &= N^o_{i-2,j}e^{-t_{on}/\tau}e^{-2(t_{on}+t_{off})/\tau} + R_j\tau(1-e^{-t_{on}/\tau})e^{-2(t_{on}+t_{off})/\tau} + \\ &\quad R_j\tau(1-e^{-t_{on}/\tau})(1+e^{-(t_{on}+t_{off})/\tau}) \\ &\quad \vdots \\ &= N^o_{1,j}e^{-i(t_{on}+t_{off})/\tau}e^{t_{off}/\tau} + R_j\tau(1-e^{-t_{on}/\tau})\cdot \\ &\quad \sum_{n=0}^{i-1} e^{-n(t_{on}+t_{off})/\tau}. \end{aligned} \tag{C.1}$$

One derives the value of $N^o_{1,j}$ as

$$
\begin{aligned}
N^o_{1,j} &= N^f_{8,j-1} e^{-t_{sd}/\tau} \\
&= e^{-t_{sd}/\tau}(N^o_{1,j-1} e^{-7(t_{on}+t_{off})/\tau} e^{-t_{on}/\tau} + \\
&\quad R_{j-1}\tau(1-e^{-t_{on}/\tau}) \sum_{n=0}^{7} e^{-n(t_{on}+t_{off})/\tau}) \\
&= N^o_{1,j-1} e^{-7(t_{on}+t_{off})/\tau} e^{-(t_{on}+t_{sd})/\tau} + \\
&\quad R_{j-1}\tau(1-e^{-t_{on}/\tau}) e^{-t_{sd}/\tau} \sum_{n=0}^{7} e^{-n(t_{on}+t_{off})/\tau} \\
&= N^f_{8,j-2} e^{-t_{sd}/\tau} e^{-7(t_{on}+t_{off})/\tau} e^{-(t_{on}+t_{sd})/\tau} + \\
&\quad R_{j-1}\tau(1-e^{-t_{on}/\tau}) e^{-t_{sd}/\tau} \sum_{n=0}^{7} e^{-n(t_{on}+t_{off})/\tau} \\
&= e^{-7(t_{on}+t_{off})/\tau} e^{-(t_{on}+t_{sd})/\tau} e^{-t_{sd}/\tau}(N^o_{1,j-2} e^{-7(t_{on}+t_{off})/\tau} e^{-t_{on}/\tau} + \\
&\quad R_{j-2}\tau(1-e^{-t_{on}/\tau}) \sum_{n=0}^{7} e^{-n(t_{on}+t_{off})/\tau}) + \\
&\quad R_{j-1}\tau(1-e^{-t_{on}/\tau}) e^{-t_{sd}/\tau} \sum_{n=0}^{7} e^{-n(t_{on}+t_{off})/\tau} \\
&= N^o_{1,j-2} e^{-2*7(t_{on}+t_{off})/\tau} e^{-2(t_{on}+t_{sd})/\tau} + \\
&\quad (R_{j-1} e^{-t_{sd}/\tau} + R_{j-2} e^{-t_{sd}/\tau} e^{-(t_{on}+t_{sd})/\tau} e^{-7(t_{on}+t_{off})/\tau}) \cdot \\
&\quad \tau(1-e^{-t_{on}/\tau}) \sum_{n=0}^{7} e^{-n(t_{on}+t_{off})/\tau} \\
&\quad \vdots \\
&= N^o_{1,1} e^{-7(j-1)(t_{on}+t_{off})/\tau} e^{-(j-1)(t_{on}+t_{sd})/\tau} + \\
&\quad \tau(1-e^{-t_{on}/\tau}) e^{-t_{sd}/\tau} \sum_{n=0}^{7} e^{-n(t_{on}+t_{off})/\tau} \sum_{m=1}^{j-1} R_m e^{-7(j-1-m)(t_{on}+t_{off})/\tau} \cdot \\
&\quad e^{-(j-1-m)(t_{on}+t_{sd})/\tau} \\
&= \sum_{m=1}^{j-1} R_m \tau(1-e^{-t_{on}/\tau}) \sum_{n=0}^{7} e^{-n(t_{on}+t_{off})/\tau} \cdot \\
&\quad e^{-(j-1-m)(8t_{on}+7t_{off})/\tau} e^{-(j-m)t_{sd}/\tau}, \qquad \text{(C.2)}
\end{aligned}
$$

where $N^o_{1,1}$ is equal to 0. Thus, one can put the result of equation C.2 into equation C.1 to obtain an analytic solution for the number of undecayed staus remaining at the end of each period i of year j.